DEVELOPING BIOMATERIAL-BASED APPROACHES TO IMPROVE TREATMENT OF OVARIAN CANCER

A DISSERTATION

SUBMITTED TO THE FACULTY OF THE

UNIVERSITY OF MINNESOTA

BY

Tiffany Lam

IN PARTIAL FULFILLMENT OF THE REQUIREMENTS

FOR THE DEGREE OF

DOCTOR OF PHILOSOPHY

Advisor

Samira M. Azarin

April 2021

Acknowledgements

A big thank you my PhD advisor, Samira Azarin. I am grateful for her mentorship during my time as a graduate student. I thank her immensely for being supportive in all my research endeavors and supporting me professionally and personally beyond graduate school. I thank her most for being an inspiring role model and advocate for women and diversity in STEM.

Thank you to everyone in the Azarin Lab. A special thank you to Frankie and Ray for teaching me so much in my first few years in the lab, and I will always remember our collaborations together. Thank you to Jen and Pedram for always letting me learn from you and being great mentors. Another big thank you to Jenny and Hannah who have always been great role models/mentors and now are my good friends. I also want to thank Harish for being a great friend and colleague, and it has been quite the journey since we joined the lab together in 2016! Another shout out to Joe who I have enjoyed collaborating with, and I am excited to see what findings you will discover in our FIT collaboration after I have graduated. Lastly, a thank you to all the other Azarin Lab members and I thank everyone for making our group one that fosters great science, collaboration, and camaraderie.

A special thank you to all my friends I have made in the CEMS incoming class of 2016. The journey has been a long and challenging one, but you have all made it fun and full of adventure. I look forward to staying in touch, with many reunions to come. Another thank you to all my good friends from home who have supported me since our middle/high-school days.

A last thank you to my family who has supported me all throughout graduate school and well before then. Thank you so much to my mom and dad who have given me all the opportunities I have had so far. Thank you to my younger siblings, Jenny and Jacob, who have been great supporters since the beginning. I also want to thank my grandma and Uncle Joe for always believing in me. And a very big thank you to Ryan for always being there for me and for supporting me through the entire graduate school process - all the way from applying to graduate school to now at the end of my PhD.

Abstract

In ovarian cancer, the standard of care treatment, which is surgery followed by chemotherapy, has remained relatively unchanged for over the last forty years. However, the overall survival rate for ovarian cancer has stagnated to only ~ 40%. This is due to long-standing clinical challenges in the treatment of ovarian cancer including patients often having advanced stage disease at the time of diagnosis and majority of patients will exhibit recurrence and eventually acquire chemoresistant disease. Unfortunately, after patients no longer respond to chemotherapy, most will succumb to their disease due to the lack of efficacious alternative treatment modalities.

The goal of this dissertation was to develop biomaterial-based approaches which can help improve ovarian cancer treatment. In Chapter 2, a biomaterial platform immobilizing ovarian cancer cells into stiff yet porous silica gels is described. The response to immobilization in stiff silica gels by ovarian cancer cells was extensively characterized, and it was shown that this platform can select for ovarian cancer cells with an enhanced ability to enter a non-proliferative state in order to tolerate the stress of physical confinement. Further, these cells could be removed from silica gels and were more resistant to platinum- and taxane-based chemotherapy, despite being proliferative at the time of drug treatment. It was also observed that silica gels could distinguish ovarian cancer cells with enhanced chemoresistance relative to more chemosensitive cells, as seen by enhanced survival upon immobilization. When compared to other *in vitro* platforms commonly used to induce quiescence, the silica gel immobilization platform could better select for ovarian cancer cells with enhanced chemoresistance.

Chapter 3 discusses a facile method to incorporate iron oxide particles into microporous poly(caprolactone) (PCL) scaffolds previously developed in our group. These scaffolds have previously been shown to recruit metastatic breast cancer cells *in vivo*, and we sought to modify the scaffolds to be able to non-invasively kill cells after they arrived at this known targetable site. After successful incorporation of iron oxide into the scaffolds, it was demonstrated that they exhibited heating when placed under an alternating magnetic field

(AMF). Simple design parameters like the amount of iron oxide loaded into scaffolds or magnetic field strength could be tuned to alter the overall temperature rise exhibited by iron oxide-loaded scaffolds under AMF. The iron oxide itself did not cause cytotoxic effects, but iron oxide-loaded scaffolds under AMF could be used to successfully heat and kill loaded ovarian cancer cells *in vitro*. After implantation in the peritoneal cavity of female mice, iron oxide-loaded scaffolds became infiltrated with tissue after 6-7 weeks, and *ex vivo* AMF treatment of these iron oxide-loaded scaffolds could be used to kill infiltrated cells. Lastly, non-invasive hyperthermic treatment could be administered to mice with implanted iron oxide-loaded scaffolds, and iron oxide-loaded scaffolds under AMF could effectively kill infiltrated cells *in vivo*.

Chapter 4 further explores the potential of the PCL-only and iron oxide-loaded scaffolds to be used as a therapy for ovarian cancer. The use of an advanced stage ID8 ovarian cancer mouse model is first described, since our group has not used this type of cancer model before. The mouse model exhibited hallmarks of advanced stage disease, including ascites accumulation and extensive metastases within the peritoneal cavity. Because the ID8 ovarian cancer cells were not labeled, a method to quantify the extent of disease during disease progression and at study end-points was implemented. More importantly, the ability of the scaffolds to capture disseminated ovarian cancer cells *in vivo* was investigated. PCL-only scaffolds were able to capture disseminated ovarian cancer cells *in vivo*, regardless of whether they were implanted prior to cancer cell injection or during disease progression. Most notably, iron oxide-loaded scaffolds successfully captured disseminated ovarian cancer cells throughout disease progression, and significant disease formation was not necessary for cancer cell capture at iron oxide-loaded scaffolds. Lastly, future studies to expand upon the work described here are recommended in Chapter 5. Overall, the biomaterial-based approaches developed and discussed in this dissertation could be used to help improve the treatment of ovarian cancer.

Table of Contents

List of Tables

List of Figures

Chapter 1: Introduction

1.1 Ovarian cancer and standard of care treatment

Ovarian cancer is the fifth-leading cause of cancer-related death in women, and ~ 22,000 women in the U.S. will be diagnosed with ovarian cancer each year, with 64% of these patients ultimately succumbing to the disease[1]. In recent decades, improvements have been made to optimize the standard of care for ovarian cancer which includes surgery followed by platinum- and taxane-based chemotherapy. However, the overall cure rate for patients has stagnated to only around 40%[2], leaving ovarian cancer as the most lethal gynecologic malignancy[1]. A significant obstacle in the treatment of ovarian cancer has been that most patients will have advanced stage disease, where the cancer has spread beyond the primary tumor, at the time of diagnosis. Advanced stage patients will often have metastases throughout the abdominal cavity and may have ascites - a protein-rich fluid associated with malignancy and poor prognosis - prior to even starting treatment. An additional long-standing challenge has been that a significant number of patients will exhibit cancer recurrence after completing initial treatment and no longer respond to chemotherapy. Lastly, although it is well-known that many patients will stop responding to drug treatment, alternative therapies for ovarian cancer are sparse and have shown limited success.

Ovarian cancer is a highly mutated cancer[3], and it is often marked by multiple genetic and epigenetic abnormalities[4]. Many tumor suppressor genes and oncogenes have previously been implicated in ovarian cancer[5]. An oncogene is a mutated form of a gene typically involved in normal cell growth and drives cancer proliferation, while a tumor suppressor gene is one that regulates cell growth, but its mutation and loss of function can lead to

cancer. In a comprehensive analysis performed by The Cancer Genome Atlas in 2011[6], it was discovered that a number of genes were significantly mutated in ovarian cancers, and one of the most common abnormalities involved the mutation and loss of *p53* gene function. The *p53* gene is a tumor suppressor gene that is activated under various cellular stimuli or stress - most importantly DNA damage - which can lead to cell cycle arrest, senescence, and apoptosis. The most common outcome of all *p53* mutations is loss of function[7], resulting in loss of the original tumor suppression activity of the wildtype *p53* gene and its regulation of cell cycle arrest and apoptosis in DNA-damaged cells. Another genetic abnormality associated with ovarian cancer involves hereditary mutations in DNA repair genes, which comprises 10 - 15% of ovarian cancers[8,9]. The most well-known of these are mutations of the *BRCA1* and *BRCA2* genes. An essential way for cells to repair double-strand DNA breaks involves homologous recombination (HR) repair, and both *BRCA1* and *BRCA2* have multiple, unique roles in HR repair[3]. Consequently, patients with *BRCA1/2* mutations will have an increased potential for cell oncogenesis compared to the general public[3], with the lifetime risk of ovarian cancer increasing to 30 - 60% and 15 - 30% for those with *BRCA1* and *BRCA2* mutations, respectively[4]. Here, a few well-known gene signatures in ovarian cancer are described, but extensive genomic profiling of ovarian cancer cell lines and patient samples has been completed[10]. Findings from Domcke *et al.* demonstrate the heterogeneity in both patients and commonly used ovarian cancer cell lines, and the authors challenge investigators to make informed decisions about which cell lines to use in studies (i.e. based upon genetic mutations, histological sub-type, site of origin) to increase clinical-relevance and the potential for developing promising therapies.

As indicated above, the histological sub-type and origin site of a patient's tumor are important and can be indicative of prognosis and response to the standard of care treatment. The majority of ovarian cancers (80%) are of epithelial origin[11], and epithelial ovarian cancers (EOCs) are further categorized into histological sub-types and grades. There are four main histological sub-types of epithelial ovarian cancer: serous, endometrioid, mucinous, and clear cell. Although they are all EOCs, each histological sub-type is known to differ in its genetic abnormalities, gene expression, disease biomarkers, and response to chemotherapy[4]. Notably, most EOCs are of the serous sub-type[12], with 90% being specifically high-grade serous ovarian cancer (HGSOC)[13]. Because HGSOC is very aggressive and accounts for two-thirds of all ovarian cancer deaths[14], it has been the most studied ovarian cancer sub-type. The site of origin of EOCs is also important, and there has been debate about whether EOCs originate from the ovarian surface epithelium (OSE) or the fallopian tube epithelium (FTE). First proposed by Fathalla in 1971, the "incessant ovulation" theory has been widely accepted, and it hypothesizes that the frequent ovulation cycle involving rupture and repair of the OSE may lead to its malignant transformation[15]. In recent decades, the FTE as a second site of origin has been noted, and studies have shown that the FTE near the ovary displays pre-neoplastic changes in women predisposed to ovarian cancer[16,17]. Overall, all the various genetic alterations and histo-pathologies have led to a broader classification of EOCs into Type I or Type II tumor sub-types for clinical treatment. Ovarian cancers classified as Type 1 are often slow growing, while Type II tumors are more commonly of FTE origin, have *p53* mutations, and are harder to treat[18].

The heterogeneity in ovarian cancer tumors is also consequently reflected in the ovarian cancer cell lines used in preclinical studies. Using available genomic profiles from the Broad-Novartis Cancer Cell Line Encyclopedia[19], Domcke *et al.* compared 47 ovarian cancer cell lines, including the most widely used SKOV-3, A2780, OVCAR-3, CAOV-3, and IGROV-1 cell lines[10]. It was discovered that mutated genes characteristic of HGSOC were also mutated in a significant fraction of the cell lines, with *p53*, *BRCA1*, and *BRCA2* mutated in 62%, 6%, and 9% of cancer cell lines, respectively. Specifically, the commonly used OVCAR-3 and CAOV-3 cell lines have *p53* mutations and other gene abnormalities (i.e. high copy-number alterations) characteristic of HGSOC. Contrastingly, SKOV-3 and A2780 cell lines maintain wildtype *p53* but carry mutations that are common in other histological sub-types. IGROV-1 was "hypermutated" relative to HGSOC and is predicted to not be HGSOC but instead an endometrial or clear cell ovarian cancer sub-type. The patients' specimen type from which the cell lines were established and exposure to chemotherapy also differ. IGROV-1, CAOV-3, and A2780 were established from the primary tumor tissue of patients[20], but OVCAR-3 and SKOV-3 originated from cells in patients' ascites fluid[21]. The patient from which the A2780 cell line was established had not been treated with chemotherapy, and the IGROV-1 cell line is considered to be sensitive to cisplatin, the platinum-based drug of choice for ovarian cancer, which is consistent with the fact that the patient from which IGROV-1 was established had no prior chemotherapy treatment[20]. Contrastingly, the OVCAR-3 cell line was established from a patient who had progressive disease after combination chemotherapy - which included cisplatin - and is resistant to clinically-relevant doses of cisplatin[21]. Overall, the heterogeneity within patient tumors and ovarian cancer cell lines provides opportunity to

investigate and develop therapies tailored to specific ovarian cancer sub-types and groups of patients.

Understanding how ovarian cancer metastasizes is also important for developing effective treatments, and ovarian cancer is unique from other cancers because of its route of metastasis. Other cancers which form solid primary tumors require disseminated cancer cells to undergo multiple intra- and extravasation steps through blood vasculature before arriving at sites permissive for metastasis, but in ovarian cancer, metastases are often confined within the peritoneal cavity after shedding from the primary tumor[22]. It is well accepted that the first step in ovarian cancer metastasis is for cells to undergo an epithelial-to-mesenchymal (EMT) transition. In ovarian cancer, the EMT transition is mainly characterized by loss of E-cadherin expression, which results in decreased adherence and anchorage of neighboring epithelial cells[23–25]. Once cells have detached from the primary tumor, passive metastasis of disseminated cancer cells occurs through their transport in the peritoneal or ascites fluid either as single cells or as clusters of cells called spheroids. The disseminated ovarian cancer cells will often arrive at the peritoneum or omentum[26] and use CD44[27,28] and β-integrins[29,30] to bind to the mesothelium lining. The peritoneum is the membrane that lines the abdominal cavity and organs, and the omentum is a structure of folds connected to the peritoneum made largely of fat, which connects the abdominal organs. The mesothelium lining consists of a single layer of cells attached to basement membrane that lines the abdominal cavity, including the peritoneum and omentum. After successful attachment, ovarian cancer cells will upregulate matrix metalloproteinase-2 (MMP-2) to degrade extracellular matrix proteins to better adhere to the basement membrane. Lastly, it has been shown that these cells can promote blood vessel formation

to support secondary metastatic growth[22], and angiogenesis through vascular endothelial growth factor (VEGF) has been shown to be important for the growth of intraperitoneal (i.p.) metastases and ascites production *in vivo*[31].

Currently, standard of care treatment for ovarian cancer involves debulking surgery followed by combination chemotherapy using platinum- and taxane-based agents. Because most patients are diagnosed at a stage where the cancer has spread, surgery aims to remove as much cancerous tissue as possible within the peritoneal cavity prior to chemotherapy. Ovarian cancer is one of the few cancers where surgery is routinely done but unlikely to remove all of the cancerous tissue, and studies have previously shown that more extensive surgeries (i.e. maximal cytoreductive surgery versus partial removal or biopsy only) help extend patient survival[32–34]. Single-agent chemotherapy of platinum-based agents was originally used in ovarian cancer treatment, and cisplatin has been the platinum-based drug of choice for over the last forty years, with patient prognosis correlating closely with response to cisplatin treatment[35]. Cytotoxic effects of cisplatin and other platinum-based drugs are mediated by formation of interstrand and intrastrand adducts between platinum and DNA[36,37]. These Pt-DNA adducts can disrupt the cell's ability to properly replicate its DNA for cell division, and without effective DNA repair, the cell will undergo cell death by inducing apoptosis. Briefly, combination chemotherapy of cisplatin with cyclophosphamide was standard after surgery, as combination drug treatment provided synergistic effects relative to single-agent chemotherapy. However, following its introduction in the 1990s, paclitaxel - a taxane-based drug - combined with cisplatin in clinical trials demonstrated improved outcomes relative to cisplatin/cyclophosphamide and has been the standard of care since[38,39]. Taxane-based drugs promote apoptosis by

stabilizing the cell's microtubules and does not allow their disassembly for chromosome separation during cell division which causes cell cycle arrest[40]. Interestingly, most ovarian cancer patients (70 - 80%) will have chemosensitive disease at diagnosis and respond to this current standard of care; however, even though most will initially respond to treatment, majority of patients will exhibit recurrence and ultimately succumb to the disease.

1.2 Recurrence and chemoresistance

Over 60% of ovarian cancer patients will eventually experience recurrence[41]. Currently, these patients have limited treatment options and are left with a more malignant form of the disease that is incurable with existing treatments[42]. Depending on their initial response to platinum-based chemotherapy, some ovarian cancer patients are re-treated with platinum-based chemotherapy. However, the probability of an effective secondary response to this treatment is low (**Fig. 1.1**)[43], and it is predicted by the length of the patient's previous response to platinum-based chemotherapy[44]. Unfortunately, it is recognized in the clinic that all patients with recurrent disease will eventually exhibit platinum-resistance[42]. Further, about 25% of patients will have platinum-resistant disease, which is defined by recurrence within 6 months of completing treatment[42,43,45]. For these ovarian cancer patients and ones who stop responding to secondary platinum-based chemotherapy, the standard practice is to next try treatment with another single-agent chemotherapy[46,47]. However, low response rates are typical[47], and in phase II clinical trials, overall response rates have been shown to only range from 10 - 35% followed by disease progression after 8 months[48]. Eventually, most patients will develop multi-drug resistance to whichever chemotherapeutics are used, suggesting the need to shift away from cytotoxic drugs towards other treatment modalities[36].

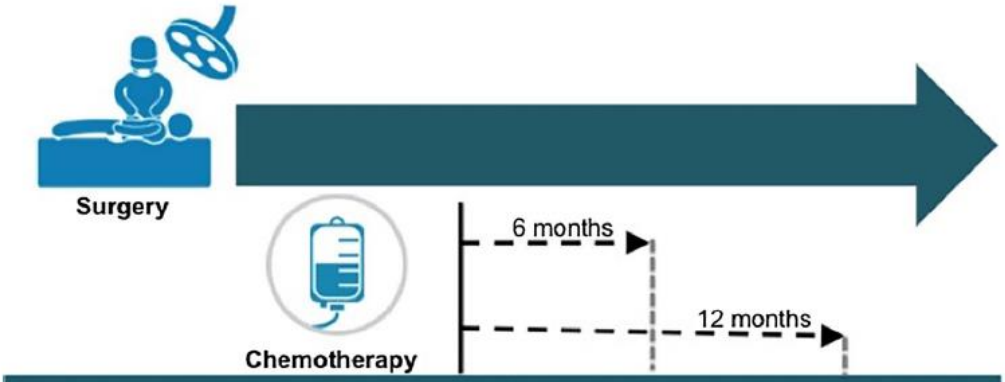

Platinum sensitivity classification	Refractory	Resistant	Partially sensitive	Sensitive
Probability of second platinum response	0%	<10%	30%	>50%

Figure 1.1: Clinical classifications of platinum sensitivity and probability of secondary response to re-treatment with platinum-based chemotherapy[43].

Numerous strategies are being investigated for their utility in predicting patient response to chemotherapy. Patient-derived xenograft models have been explored for potential correlation between patient and avatar response to chemotherapy. Past studies have shown that mice bearing xenografts from patients responding poorly to platinum chemotherapy also experienced tumor progression during *in vivo* treatment, while mice responding well to treatment corresponded to patients with better progression-free survival (PFS)[49,50]. *In vitro* chemoresponse assays – such as the ATP-tumor chemosensitivity assay (ATP-TCA) and extreme drug resistance (EDR) assay – have also been investigated for the ability to identify resistance to individual drugs. The EDR assay testing platinum compounds has previously shown promise for predicting ovarian cancer patient overall response to platinum/taxane combination therapy and response to platinum-based treatment alone[51]. Additionally, clinical trials have shown that using ATP-TCA to guide decisions throughout multiple rounds of chemotherapy leads to improved survival for ovarian cancer patients[52]. Although some studies indicate promising results, chemoresponse assays continue to only

be used in research trials and have not been recommended for use in clinical practice due to limitations of the studies that have been completed thus far[51,53]. Lastly, many studies have focused on whether gene expression of tumor cells from biopsy samples or cancer cell lines can be used to identify gene signatures or biomarkers for resistance to chemotherapy. Platforms involving microarrays, immunohistochemistry, and other methods are being investigated. However, a gene signature predicting clinical resistance has not yet been identified, and biomarkers associated with chemoresistance still require further validation before they would be used to inform clinical treatment decisions[54,55].

The main modes of chemoresistance in ovarian cancer are posited to be mechanisms involving increased DNA repair, enhanced drug efflux/detoxification, and increased tolerance of DNA damage leading to decreased apoptosis and pro-survival outcomes for cancer cells[37]. As platinum agents are the drug of choice in ovarian cancer, enhanced DNA repair mechanisms involving removal of Pt-DNA adducts are believed to be a primary source of chemoresistance in ovarian cancer. Enhanced use of the nucleotide excision repair (NER) pathway and specifically expression of ERCC-1, a key enzyme in the NER pathway, are known to correlate with clinical resistance to platinum-based chemotherapy[56]. ERCC-1 along with other NER components and innate DNA repair pathways are currently being investigated as predictive biomarkers for patient response to platinum chemotherapy. Enhanced expression of transport proteins such as multi-drug resistance protein 1 and P-gp are also associated with chemoresistance, since they are known to decrease drug accumulation of multiple types of chemotherapy in ovarian cancer[57]. Glutathione and glutathione S transferases also aid in detoxification of various chemotherapeutic agents[58], ultimately contributing to multi-drug resistance in ovarian cancer. Further, imbalance of

anti- and pro-apoptotic signaling can lead to the development and maintenance of chemoresistance in ovarian cancer, and pathways necessary for induction or inhibition of apoptosis (i.e. *p53*, *Akt*, *PI3K*) are typically dysregulated in ovarian cancer, which may ultimately contribute to survival of cancer cells during chemotherapy treatment[59].

1.3 Cellular dormancy and its potential role in ovarian cancer chemoresistance

With many ovarian cancer patients initially responding to frontline treatments and some exhibiting complete remission prior to recurrence, it is posited that a potential cause of recurrence is the reawakening of dormant cancer cells that survive treatment[60,61]. Dormant cancer cells are not progressing through the cell cycle and actively dividing (**Fig. 1.2**), and instead, they exist in a reversible, non-proliferative state due to growth arrest in the G0/G1 phase. Consequently, dormant cancer cells are characterized by loss of the Ki67 proliferation-specific biomarker, as loss of Ki67 expression indicates exit from the cell cycle into a resting (G0) phase[62]. Dormant cancer cells may be present in a patient as early as development of the primary tumor or they can be left behind as minimal residual disease after what appears to be successful initial treatment[63]. Within a primary tumor, there is great heterogeneity in the cancer cell population, and while cancer cells are often characterized as rapidly dividing, a considerable proportion of these cancer cells will remain in a non-proliferative state[61]. Another source of dormant cancer cells are disseminated tumor cells shed from the primary tumor which can become dormant after arriving at sites not permissive to proliferation such as hypoxic and nutrient-deficient environments[64]. Furthermore, a cancer stem cell hypothesis has emerged suggesting that innately chemoresistant and dormant cancer cells with stem cell characteristics may reside

within the primary tumor, persist through chemotherapy, and repopulate chemoresistant disease after months or years upon completing treatment[60].

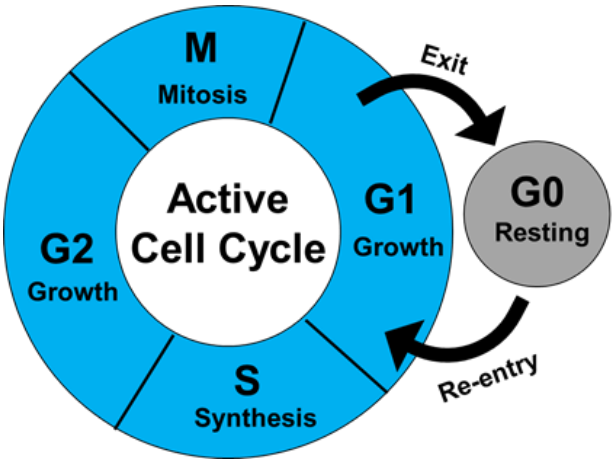

Figure 1.2: Schematic of the cell cycle. Cells in the G1, S, G2, and M phases are actively growing or dividing. Some cells may also undergo temporary growth arrest by exiting from the cell cycle into the G0 phase.

Although cancer cell dormancy has been established to play a crucial role in cancer progression and recurrence, the mechanisms by which cancer cells enter dormancy remain poorly understood. Moreover, not all cancer cells are able to enter dormancy, and it is unclear why only a unique subset of these cells is able to undergo growth arrest to survive unfavorable conditions. Understanding the genetic mechanisms allowing cancer cells to transiently enter and reawaken from the dormant state could help minimize recurrence, but extensive study of cancer cell dormancy has been hindered due to the inability to easily collect these rare cells for study.

Since most chemotherapy drugs kill rapidly dividing cells, it is believed that cancer cells which can readily enter dormancy have an enhanced ability to evade destruction during chemotherapy treatment and may ultimately engender chemoresistant disease. These

cancer cells may evade frontline chemotherapy treatment because they are innately drug-resistant or have a propensity to become drug-resistant after entering a latent state due to adverse environments[61]. Therefore, it is probable that cancer cells which have entered dormancy and previously been exposed to chemotherapeutics, but were not destroyed, can reawaken and establish secondary, chemoresistant disease once favorable conditions are restored[37,60]. Similar findings have been discovered in other cancer types such as breast cancer, where residual tumor cells can maintain an asymptomatic, dormant state for months to years. These cells also appear to bear drug-resistant mechanisms protecting them from initial chemotherapy eventually resulting in disease recurrence[63,64].

While the precise link between chemoresistance and dormancy in ovarian cancer is unknown, it is suggested that these two cellular processes are related since ovarian cancer patients who recur will ultimately have incurable, chemoresistant disease[42]. Because platinum-mediated cytotoxicity is dependent on DNA damage recognition to induce apoptosis, dormancy-capable cancer cells are less likely to be affected by treatment since they can exit the cell cycle, at which point they will not attempt to replicate their DNA for cell division. Additionally, cancer cells that are less proliferative may have more time for drug detoxification or Pt-DNA adduct removal before Pt-DNA adducts are discovered by the necessary protein complexes that induce apoptosis. With taxane-based agents, the drug mechanism of action involves pushing cells into cell cycle arrest followed by apoptosis due to altered chromosome separation; however, this mechanism may not be as lethal for cells which readily enter dormancy/cell cycle arrest in order to tolerate stressful environmental conditions. Although recurrence and chemoresistance have remained common outcomes

for ovarian cancer patients, alternative treatment modalities that can minimize these events and are efficacious are limited.

1.4 Alternative treatment options for ovarian cancer

Anti-angiogenic agents, poly ADP ribose polymerase (PARP) inhibitors, and immunotherapies have been investigated as alternative treatments, but these approaches are far from replacing the current standard of care. Anti-angiogenic agents have been used to combat ovarian cancer because angiogenesis and angiogenic-related genes have proven to play a crucial role in ovarian tumor growth and disease progression through ascites formation and metastatic spread[65,66]. The most widely studied anti-angiogenic therapy for all tumor types and for EOCs has been an anti-VEGF monoclonal antibody, bevacizumab[66], and 21% of recurrent ovarian cancer patients exhibited some response to treatment, with 40% exhibiting a PFS of at least 6 months in a phase II clinical trial[67]. However, most trials with anti-angiogenic agents have had difficulty demonstrating improvement in overall survival[46], and despite the fact that almost all ovarian cancer patients will be treated with an anti-angiogenic agent, cure rates have remained stagnant[66]. PARP inhibitors, which prevent repair of single-strand DNA breaks, are intended to be used as a maintenance therapy or in combination with chemotherapy. Further, they are of interest for ovarian cancer patients with tumors harboring *BRCA1/2* mutations or other defects in HR repair, and PARP inhibitors have most notably improved the PFS in these patient groups[68]. However, like chemotherapy, patients can develop resistance to PARP inhibitors, and this form of treatment would likely not be effective for patients who have already recurred and have chemoresistant disease[46,47].

Immunotherapy holds promise as an alternative treatment modality for ovarian cancer because of the potential for the patient's immune system to develop memory against tumor-specific antigens, which could help address recurrence. Thus far, two main strategies have been investigated in ovarian cancer clinical trials: immune checkpoint inhibitors (ICIs) and adoptive cell therapies (ACTs). ICIs aim to mitigate the immune system's own regulation by using antibodies to block immune cell inhibitory receptors that induce immunosuppression, and this allows the immune cells to continue attacking cancer cells. Various antibodies targeting checkpoint receptors of PD-1, PD-L1, and CTLA-4 have been investigated in recurrent ovarian cancer patients, but they have shown limited success, with objective response rates only ranging from 6 - 15%[69]. ACTs involve *ex vivo* expansion and reinfusion of a patient's own tumor-infiltrating lymphocytes (TILs) or re-engineered T cells with a chimeric antigen receptor to target and kill cancer cells. Although ACTs have shown great success in other types of cancer (i.e. melanoma[70,71]), ACTs have provided little improvement in EOCs[69,72]. Although ICIs and ACTs have shown minimal benefits on their own, combining them with previously used treatment modalities (i.e. chemotherapy, PARP inhibitors) or with other immunotherapies are worthwhile, and these combination treatments are currently under investigation. Immunotherapy clinical trial results have overall remained mixed with immunologic responses varying from patient to patient, making treatment strategies difficult to standardize[73,74]. Mixed responses to immunotherapy likely stem from the differences in immune cell populations within the patient's tumor microenvironment, and increased presence of TILs has been correlated with better survival in ovarian cancer, while patients with more immunosuppressive regulatory T cells typically have poorer outcome[69].

Because most ovarian cancer patients are diagnosed at an advanced stage where the cancer is in a disseminated form, new alternative treatment options are limited to strategies that do not require localized disease. Consequently, promising treatment modalities such as focal therapies that can effectively kill all types of cancer cells at a targeted site cannot be used. For ovarian cancer, focal therapies could help address the challenges of recurrence and chemoresistance, as these modalities use energy-based processes – cryoablation, hyperthermia, or irreversible electroporation – to lyse cells. Being unbiased, focal therapies can be used to destroy dormancy-capable or chemoresistant cancer cells, unlike chemotherapy. Overall, a method to localize disseminated ovarian cancer cells to a specific site for treatment would allow study of focal therapies and other promising treatments that currently cannot be used. A potential strategy to capture disseminated ovarian cancer cells may involve polymer scaffolds, since they have previously been shown to localize disease in an advanced stage ovarian cancer model after implantation into the peritoneal cavity of mice[75]. Further, our group has developed microporous polymer scaffolds that can recruit metastatic breast cancer cells[76,77], and their ability to capture disseminated cancer cells in ovarian cancer will be described here. Overall, innovative treatment modalities for ovarian cancer are needed as the existing standard of care – surgery and platinum- and taxane-based chemotherapy – will often result in recurrence and chemoresistance.

1.5 Biomaterial applications in cancer

Biomaterials have emerged as useful tools in cancer research, and over the years, they have been widely used for study in *in vitro* tumor models, diagnostics, imaging, and drug delivery[78]. These biomaterials are made of materials naturally occurring in the body or tumor microenvironment, such as collagen and fibrin, or are synthetic systems derived

from materials which are not readily found *in vivo* such as silica-based materials or other synthetic polymers. For ovarian cancer, biomaterials involved in dormancy and chemoresistance research and applications to mitigate metastatic disease are of particular interest. Biomaterial matrices and scaffolds have been extensively used to model *in vitro* tumor microenvironments and to investigate which tunable material properties (i.e. composition, stiffness, architecture, chemical and biophysical factors) may result in dormancy or chemoresistance[79–82]. Further, biomaterial scaffolds loaded with cobalt chloride as a hypoxia-mimetic were shown to be useful as a potential platform to study dormancy *in vivo*[83]. In addition to mechanistic studies of dormancy and chemoresistance, biomaterials have been explored for their potential as therapeutic tools to combat platinum-resistance in ovarian cancer, either by enhancing delivery of chemotherapeutics or by delivering biological factors to re-sensitize cancer cells to platinum-based chemotherapy[84]. Biomaterials that can localize disseminated disease are also of interest since ovarian cancer is often diagnosed at an advanced stage. As mentioned above, polymer-based scaffolds have been used to recruit disseminated cancer cells *in vivo* in ovarian and breast cancer models[75–77,85]. Numerous studies have also used biomaterials to create a bone-mimicking niche to recruit breast, melanoma, and prostate cancer cells[86–89]. The rationale for these systems is that they mimic pre-metastatic niches or tissues/organs that are typical sites of metastasis[76,77,87,90–92]. Overall, biomaterials and their properties such as size, morphology, and composition can be easily tailored, which provides ample opportunity for their use as innovative research and therapeutic tools. They have proven useful in improving mechanistic understanding of disease through improved *in vitro* and *in vivo* tumor models to study clinical challenges such as dormancy and chemoresistance. Lastly, biomaterial

systems offer advantages over traditional delivery systems by allowing for targeted therapies to potentially improve treatment efficacy and lower adverse side effects.

1.6 Scope and organization of thesis

The scope of this thesis involves developing biomaterial-based approaches to address the clinical challenges in ovarian cancer treatment: chemoresistance, recurrence, and lack of alternative treatment modalities. In Chapter 2, an immobilization platform using stiff silica gels to select for chemoresistant ovarian cancer cells with an enhanced ability to enter dormancy is described. Chapter 3 discusses incorporation of iron oxide into our previously developed poly(caprolactone) (PCL) polymer scaffolds for heating and killing of infiltrated cells when placed under an alternating magnetic field. The work in Chapter 4 focuses on the potential of PCL-only and iron oxide-loaded scaffolds described in Chapter 3 to capture disseminated ovarian cancer cells *in vivo* in an advanced stage ovarian cancer mouse model. Lastly, Chapter 5 discusses future directions for these projects based upon the findings obtained from this original work.

Chapter 2: Immobilization rapidly selects for chemoresistant ovarian cancer cells with enhanced ability to enter dormancy

2.1 Introduction

As described in Chapter 1, significant challenges in ovarian cancer treatment are the fact that a subset of patients will have chemoresistant disease and that most patients will experience recurrence after completing chemotherapy treatment. Unfortunately, there is currently no rapid way to predict how responsive ovarian cancer patients will be to chemotherapy prior to treatment, as patient-derived xenograft (PDX) avatar models take months to establish[93]. Recently, 3-D *in vitro* models using patient tumor cells have shown promise as platforms for predicting patient drug response and require less time than PDX models[94,95]; however, even these methods can take weeks. The ability to rapidly identify patients (within days) who would not respond to chemotherapy would enable clinicians to adjust monitoring strategies or suggest alternative therapies that are often only used once conventional treatment no longer works.

With many women initially responding to frontline treatments and some exhibiting complete remission, it is posited that recurrence and chemoresistance may be due to the presence of quiescent tumor cells that survive treatment[60,61]. Although cancer cells which

enter quiescence are known to evade chemotherapy and cause recurrence[61], the mechanisms by which they survive drug treatment remain unclear, and further study is required to determine which mechanisms contribute to resistance in cells which readily undergo growth arrest in stressful conditions. However, study of these cells and their drug-resistance mechanisms has been limited by the lack of suitable *in vitro* methods available to easily identify and isolate them.

As entering dormancy is a mechanism for cells to survive in a microenvironment that is not conducive to growth, most *in vitro* platforms utilize environmental stress to induce quiescence. Oxygen-deficient or low-serum/low-glucose treatment methods are often used to mimic hypoxic and nutrient-deficient conditions in the body, and previous studies have demonstrated accumulation of growth-arrested cells in various tumor cell lines grown under these conditions[96,97]. Recent work has shown that the stress of physical confinement upon immobilization in stiff yet porous alkoxide-based silica gels results in the ability to distinguish between cells that are readily able to enter dormancy and those that cannot, as breast cancer cell lines known to readily form tumors *in vivo* quickly die upon physical confinement while another cell line known to enter quiescence *in vivo* demonstrates enhanced survival in a growth-arrested state[98]. As the quiescence-inducing stress in this model is matrix-based and interactions with the extracellular matrix (ECM) are also implicated in the responsiveness of ovarian cancer cells to chemotherapy[60], we sought to investigate whether the stress of physical confinement and the silica gel environment potentiate chemoresistance, in addition to quiescence, in ovarian cancer.

In this chapter, we report the use of physical confinement in silica gels to identify ovarian cancer cells which exhibit quiescence when immobilized and resume proliferation upon

extraction from the gel. This process selects for a population with a higher propensity to enter dormancy, as the extracted cells exhibit enhanced survival in the quiescent state upon re-immobilization. Interestingly, these extracted cells also demonstrate signaling responses similar to cells that have persisted following chemotherapy treatment, and accordingly the extracted cells are shown to be less sensitive to cisplatin and paclitaxel treatment than the original cell population. Furthermore, chemoresistant cells exhibit enhanced survival upon immobilization in the gels, indicating that they are more readily able to enter the dormant state. These findings demonstrate a linkage between chemoresistant and dormancy-capable phenotypes in ovarian cancer. As immobilization in silica gels can isolate populations with these phenotypes within days, this platform could be useful in future mechanistic or drug studies and could potentially be used as a tool to identify patients that may have chemoresistant disease and are at risk of recurrence.

2.2 Materials and Methods

2.2.1 Cell culture

OVCAR-3 and SKOV-3 cells were purchased from the ATCC (HTB-161 and HTB-77). OVCAR-3 and SKOV-3 cells were cultured in RPMI 1640 media (Thermo Fisher Scientific) and McCoy's 5A media (Thermo Fisher Scientific), respectively, supplemented with 10% fetal bovine serum (FBS) (Thermo Fisher Scientific). Cells were passaged when 80 – 90% confluence was reached. OVCAR-3 was chosen as the primary cell line since it was established from a patient who maintained progressive disease after completing combination chemotherapy and is resistant to clinically-relevant doses of cisplatin and other anticancer drugs[21]. SKOV-3 is also known to be resistant to cisplatin and other drugs.

2.2.2 Immobilization of cells by silica gel encapsulation

Silica gel matrices were formed from tetrakis(2-hydroxyethyl) orthosilicate (THEOS) and silica nanoparticles (SNPs) as described previously (**Fig. 2.1A**)[98]. Primary gelling solution consisted of FBS-supplemented cell culture media with 1% v/v penicillin-streptomycin (Thermo Fisher Scientific), 4-arm PEG (2 kDa, hydroxyl terminated, Creative PEGWorks), and NS125 silica nanoparticles (Nyacol) in a 0.9:0.1:0.02 volume ratio. Cells for encapsulation were trypsinized and cell solution at 2×10^6 cells per mL was added 1:1 with gelling solution and aliquoted to 50 µL per gel. Tetrakis (2-hydroxyethyl) orthosilicate (Gelest) was added to each aliquot at a 1:10 ratio and thoroughly mixed. Silica gel solution was quickly pipetted and spread onto a non-treated 35 mm polystyrene petri dish. Dishes were left untouched for a few minutes to allow complete gelling, after which media was added on top to prevent dehydration before incubating at 37 °C. OVCAR-3 cells were easily visualized within gels and observed to be intact and distributed primarily as single cells without forming large clusters (**Fig. 2.1B**).

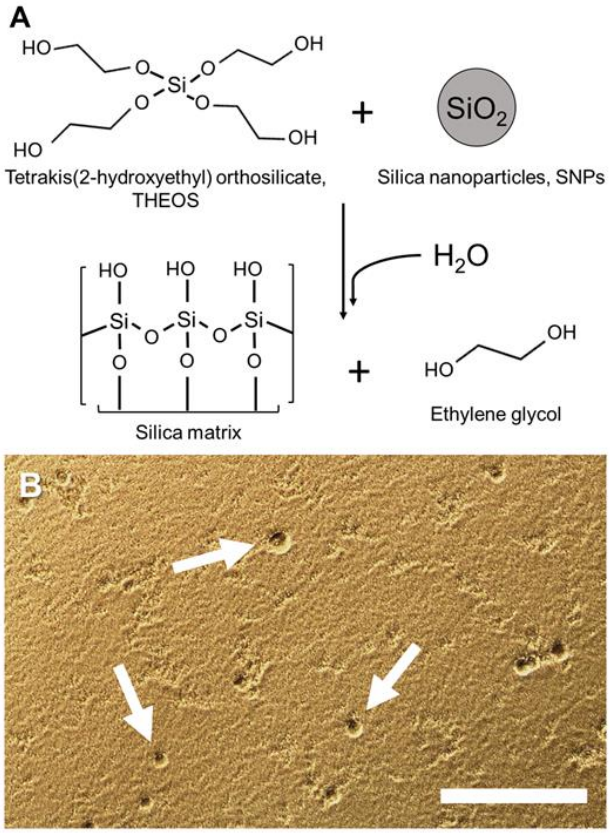

Figure 2.1: Silica gels formed from tetrakis(2-hydroxyethyl) orthosilicate (THEOS) and silica nanoparticles (SNPs) were used to immobilize OVCAR-3 cells. (**A**) Schematic of chemical formation of silica matrices by incorporating water with a silicon alkoxide, where addition of water causes hydrolysis of THEOS followed by condensation reactions producing ethylene glycol as a by-product. SNPs aid in gel network formation by acting as additional nucleation sites during gelation. (**B**) Phase-contrast image of cells (white arrows) after immobilization within a silica gel. Scale bar indicates 200 µm.

2.2.3 Quantification of immobilized viable cells

Immobilized cells were stained with Calcein AM (Thermo Fisher Scientific) diluted 1:500 in phosphate buffered saline (PBS) for 30 minutes on a shaker platform at room temperature. Live cells were imaged using an EVOS FL Auto fluorescence microscope (Thermo Fisher Scientific) at 10x magnification. Ten images were taken for each timepoint (five images each from two separate gels), and the number of live cells was manually counted from each image. Fold change in viable cell number for each day was quantified

as total number of live cells counted in each gel normalized to average total number of live cells counted in gels on Day 0.

2.2.4 Ki67 immunofluorescence analysis

Washing was completed with PBS, and all incubation steps were at room temperature on a shaker platform. 2-D or silica gel samples were washed and then fixed with a 4% paraformaldehyde (PFA) solution for 12 or 20 minutes, respectively. Samples were washed again and incubated for 1 hour with blocking solution containing PBS with 5% normal goat serum (Thermo Fisher Scientific) and 0.3% Triton X-100 (Millipore Sigma). Ki67 primary antibody in antibody dilution buffer (PBS with 0.3% Triton x-100 and 1% bovine serum albumin (BSA) (Millipore Sigma)) was added to samples for overnight incubation at 4 °C. Samples were washed followed by addition of secondary antibody in antibody dilution buffer and incubated for 1 or 2 hours for 2-D or silica gel samples, respectively. All samples were washed before addition of 300 nM DAPI nuclear staining solution (Thermo Fisher Scientific) for 5 or 30 minutes for 2-D samples or silica gels, respectively. Samples were washed once more then imaged using an EVOS FL Auto fluorescence microscope with the same intensity and exposure time for all samples. See **Table 2.1** below for antibody details.

Table 2.1: Detailed information for antibodies used in immunofluorescence (IF) and Western blotting (WB) experiments.

Target	Application	Vendor Information	Dilution
Ki67	Primary, IF	D3B5 Rabbit IgG, Cell Signaling Technology	1:500
--	Secondary, IF	AlexaFluor 594 Goat anti-Rabbit IgG, Thermo Fisher Scientific	1:1000
P-p38	Primary, WB	Phospho-p38 MAPK (Thr180/Tyr182), Cell Signaling Technology	1:1000
p38	Primary, WB	p38 MAPK, Cell Signaling Technology	1:1000
P-ERK1/2	Primary, WB	Phospho-p44/42 MAPK (Erk1/2) (Thr202/Tyr204), Cell Signaling Technology	1:1000
ERK1/2	Primary, WB	p44/42 MAPK (Erk1/2), Cell Signaling Technology	1:1000
β-actin	Primary, WB	Rabbit mAb (13E5) HRP-conjugated, Cell Signaling Technology	1:1000
--	Secondary, WB	Goat anti-Rabbit HRP-conjugated, Cell Signaling Technology	1:1000

2.2.5 Senescence-associated β-galactosidase staining

Staining was completed using the Senescence β-Galactosidase Staining Kit #9860 from Cell Signaling Technologies according to the manufacturer's instructions. Briefly, 2-D or silica gel samples were washed then fixed with 1x fixative solution for 12 or 20 minutes, respectively. Samples were washed again, and β-galactosidase staining solution was prepared, adjusted to a final pH between 5.9 and 6.1, and added. Samples were covered with parafilm to prevent evaporation, and 2-D or silica gel samples were placed in a dry 37 °C incubator overnight or for 24 hours, respectively. Brightfield images at 20x magnification were taken using an EVOS FL Auto fluorescence microscope. High passage human foreskin fibroblasts (ATCC; SCRC-1041) were used as a positive control.

2.2.6 Cell extraction

Gels were rinsed with PBS followed by incubation with 0.25% trypsin-EDTA for 7 minutes at 37 °C. Cells were then extracted from silica gels by pipetting with cell culture media to

break apart the gels. The gel fragment and media solution was transferred to a conical tube and further pipetted to break up large fragments. This solution was transferred to a T75 flask containing cell culture media with 1% v/v penicillin-streptomycin and incubated overnight. Flasks were then washed two times with PBS to remove any remaining silica gel fragments, and fresh cell culture media with 1% v/v penicillin-streptomycin was added. For studies involving regrowth and treatment of extracted cells, extracted cells were imaged at the same locations ($n \geq 9$ for each condition) for up to one week. Viable cell number was determined by manually counting cells from these images.

2.2.7 Western blotting

Protein was extracted from cells immobilized in silica gels for three days and cells maintained in standard 2-D culture using Halt Phosphatase Inhibitor Cocktail (Thermo Fisher Scientific) and Halt Protease Inhibitor Cocktail (Thermo Fisher Scientific), each diluted 1:100 in RIPA lysis buffer (Thermo Fisher Scientific). For protein separation, 10 µg of protein was loaded per well of a 4-15% Mini-Protean SDS-PAGE gel (Bio-Rad) for β-actin detection, and 30 µg of protein was loaded per well for detection of mitogen-activated protein kinase (MAPK) proteins. Proteins were then transferred to a polyvinylidene difluoride membrane (Bio-Rad), and membranes for MAPK proteins and β-actin were blocked in Tris-buffered saline containing Tween-20 (TBS-T, Millipore Sigma) with 5% BSA or 5% non-fat dry milk (Bio-Rad), respectively, for 1 hour at room temperature. Membranes were then incubated overnight at 4 °C with primary antibodies in TBS-T with 5% BSA or 5% milk for MAPKs and β-actin, respectively. MAPK membranes were then rinsed and incubated with secondary antibody diluted in TBS-T with 5% BSA

for 1 hour at room temperature. SuperSignal West Pico Chemiluminescent substrate (Thermo Fisher Scientific) was used to detect protein bands, which were then imaged with a ChemiDoc Touch Imaging System (Bio-Rad). Western blot data was quantified using Image Lab software (Bio-Rad). The ratio of activated p38 is defined as the phosphorylated p38 MAPK "pp38" band intensity divided by the p38 MAPK "p38" band intensity. Similarly, the ratio of activated ERK is defined as the phosphorylated ERK1/2 MAPKs "pERK1/2" band intensity divided by the ERK1/2 MAPKs "ERK1/2" band intensity. The final p38:ERK activity ratio was then found by dividing these two ratios (ratio of activated p38/ratio of activated ERK). See supplemental information for antibody details (**Table 2.1**).

2.2.8 RNA-sequencing sample preparation and analysis

Total RNA was collected from cells using the RNeasy Mini Kit (Qiagen) with two replicate samples collected for each condition (5 conditions, 10 samples total). 5 µg of RNA for each sample was submitted to the University of Minnesota Genomics Core for library creation and sequencing. Ten dual-indexed Illumina TruSeq stranded mRNA libraries were created for paired-end sequencing, and sequencing was completed in one lane of a HiSeq 2500 2x125-bp run using v4 chemistry, providing a total of ~22 million reads per sample. Trimming of low-quality ends and removal of adapter sequences was completed using Trimmomatic. Spliced Transcripts Alignment to a Reference (STAR) was used for mapping of reads to the human reference genome (GRCh38.91). The HTseq package in Python was used to obtain raw counts per million for each gene, then the EdgeR package in R was used to determine the fold change and significance of gene expression in pair-wise comparisons of the various experimental conditions relative to the control. Further

analyses of these genes included Gene Ontology enrichment analysis using Database for Annotation, Visualization, and Integrated Discovery (DAVID v6.8, https://david.ncifcrf.gov/) for genes meeting criteria of fold change ≥ 2 and P-value < 0.05 and Ingenuity Pathway Analysis (IPA) (Qiagen) for genes with fold change ≥ 2, P-value < 0.05, and false discovery rate < 0.05. For comparison to patient data, genes identified as differentially expressed between chemoresistant and chemosensitive patients in the discovery group by Koti *et al.* and in their *in silico* analysis of patient datasets from The Cancer Genome Atlas were used[99]. Differentially expressed genes from these analyses were compared to the differentially expressed genes in our "Extracted" group relative to control, and genes which were commonly up- or downregulated in both datasets were used in IPA to identify which canonical signaling pathways were most relevant to the common differential gene expression observed in the patient cohorts and our *in vitro* groups.

2.2.9 Hypoxia, serum starvation, and drug treatment

Cells were seeded with 10% FBS-supplemented cell culture media and after 24 hours, plates were then placed into a hypoxia chamber (STEMCELL Technologies) maintaining 1% oxygen conditions for hypoxia treatment or media was aspirated and serum-free cell culture media was added to wells for serum starvation. For drug treatment studies, cells were seeded with 10% FBS-supplemented cell culture media and incubated at 37 °C overnight, and drug-containing media was freshly prepared prior to addition to cells for each treatment. Cells were grown in drug-containing media for 24 hours after each addition, then drug-containing media was aspirated and cells were rinsed with PBS followed by addition of fresh 10% FBS-supplemented cell culture media. Cisplatin (Millipore Sigma) was solubilized in ultrapure water by gentle stirring at 25 °C for 10-15

minutes then filtered and stored in the dark at room temperature as a 10 mM stock solution. Paclitaxel (Tocris) was reconstituted to a 100 mM stock solution with dimethyl sulfoxide, aliquoted, and stored at -20 °C.

2.2.10 Hypoxia or serum starvation studies with cisplatin treatment

Cells for standard culture, hypoxic, and serum starvation conditions were seeded at 100,000, 250,000, or 500,000 cells per well, respectively, on 6 well-plates in 10% FBS-supplemented cell culture media and incubated at 37 °C. Different seeding densities were chosen to ensure that the cell density for each condition was roughly the same at the start of cisplatin treatment. After 24 hours, cells were placed into a 1% oxygen hypoxia chamber or serum-free cell culture media was added to wells. After three days, media containing 0.5 μM cisplatin was added to wells, while control wells received drug-free media. After 24 hours of drug treatment, all wells were washed with PBS and fresh drug-free cell culture media was added. After three days, cells were stained with Trypan Blue (Thermo Fisher Scientific) and counted (Countess II Automated Cell Counter, Thermo Fisher Scientific).

2.2.11 Statistical analysis

Data are represented as mean ± S.D. of two or more biological replicates from one of three representative independent experiments or as mean ± S.D. from three combined independent experiments. P-values were determined from Student's unpaired t-test using GraphPad Prism software, with P-value < 0.05 considered to be statistically significant.

2.3 Results and Discussion

2.3.1 Immobilized OVCAR-3 cells within silica gels exhibit hallmarks of single cell dormancy

After immobilization in stiff yet porous silica gels which have previously been characterized and shown to inhibit cell motility, growth, and proliferation[100], a substantial decrease in viable OVCAR-3 cells was observed over time, with surviving cells remaining in a single-cell state and having no evident increase in size (**Fig. 2.2A**). The percentage of Ki67-positive cells significantly decreased by Day 3 of immobilization and continued to decrease at later timepoints (**Fig. 2.2B & Fig. 2.3**), which was consistent with our previous observations with the MCF-7 breast cancer cell line[98]. Ki67 is expressed in actively dividing cells and has been extensively characterized as a proliferation-specific marker, with loss of Ki67 expression indicating cell cycle exit into a resting (G0) phase[62,101]. Immobilized live cells also demonstrated an increased p38:ERK activity ratio and higher expression of phosphorylated p38 MAPK (**Fig. 2.2C**). A high p38:ERK activity ratio is an indicator for cancer cell transition from metastatic growth to quiescence[64,102]. Increased activation of p38 signaling is associated with response to environmental stress[103] and tumor suppression[104,105]. Decreased ERK activity has been associated with small tumor nodules, while rapidly growing tumors and metastases exhibited high ERK activity *in vivo*[106]. Further, ERK and p38 levels have previously been shown to predict dormancy *in vivo* in epidermoid carcinoma, fibrosarcoma, and other tumor types, and inhibition of p38 activity has even reversed dormant behavior[107,108]. Importantly, growth-arrested cells in silica gels were not senescent, as senescence-associated β-galactosidase expression levels did not change during immobilization (**Fig. 2.4**). When extracted from the silica gels after three

days of immobilization, the cells resumed proliferation, exhibiting no significant differences in growth or morphology immediately after extraction compared to control cells (**Fig. 2.2D & Fig. 2.5**).

RNA sequencing analysis revealed 1,426 and 1,031 differentially expressed genes after 24 hours ("Day 1") or 3 days ("Day 3") of immobilization, respectively, relative to 2-D control cells, with 649 common differentially expressed genes between these groups (**Fig. 2.2E**). Gene Ontology (GO) enrichment analysis was next completed using differentially expressed genes (**Fig. 2.2F&G**). For significantly upregulated genes, terms related to stress and stimuli responses, along with interferon signaling, were enriched in both "Day 1" and "Day 3", but apoptosis-related terms appeared only in "Day 1". This result is unsurprising since the most significant reduction in viable cells occurs within the first two days of immobilization (**Fig. 2.2A**), and activation of apoptotic pathways would be present in many of these cells. Previous studies have also shown addition of exogenous interferon (IFN) induces cell cycle arrest in gastric[109] and renal[110] carcinoma cells. Wall *et al.* showed IFN-gamma had an anti-proliferative effect on ovarian cancer cell lines *in vitro*, and they observed IFN treatment of platinum-refractory ovarian cancer patients caused significant cancer cell reduction although 2% residual disease remained, eventually leading to recurrence[111]. GO analysis of downregulated genes resulted in terms related to cell adhesion, cell-protein interactions, and metabolism in both groups. Terms such as ECM-receptor interaction, integrin binding, and cell-substrate adhesion largely indicate a mechanotransduction signaling response of immobilized cells within silica gels, as cellular mechanotransduction is mediated by integrins and focal adhesions due to cell receptor binding and activation to various proteins of the extracellular matrix[112,113]. Reduced

metabolism[96] and downregulation of PI3K-Akt signaling[114–116] are associated with quiescence. Previous work has shown that malignant cells resisting anchorage-dependent apoptosis also have inactivated PI3K-Akt signaling and increased entrance into the G0 phase[117]. Additionally, patient ovarian cancer cells and OVCAR-3 cells entered quiescence and had decreased AKT phosphorylation in non-adherent culture conditions[115]. These findings demonstrate the ability of silica gels to select for viable cells exhibiting dormant behavior under immobilization stress, while most of the starting population undergo cell death.

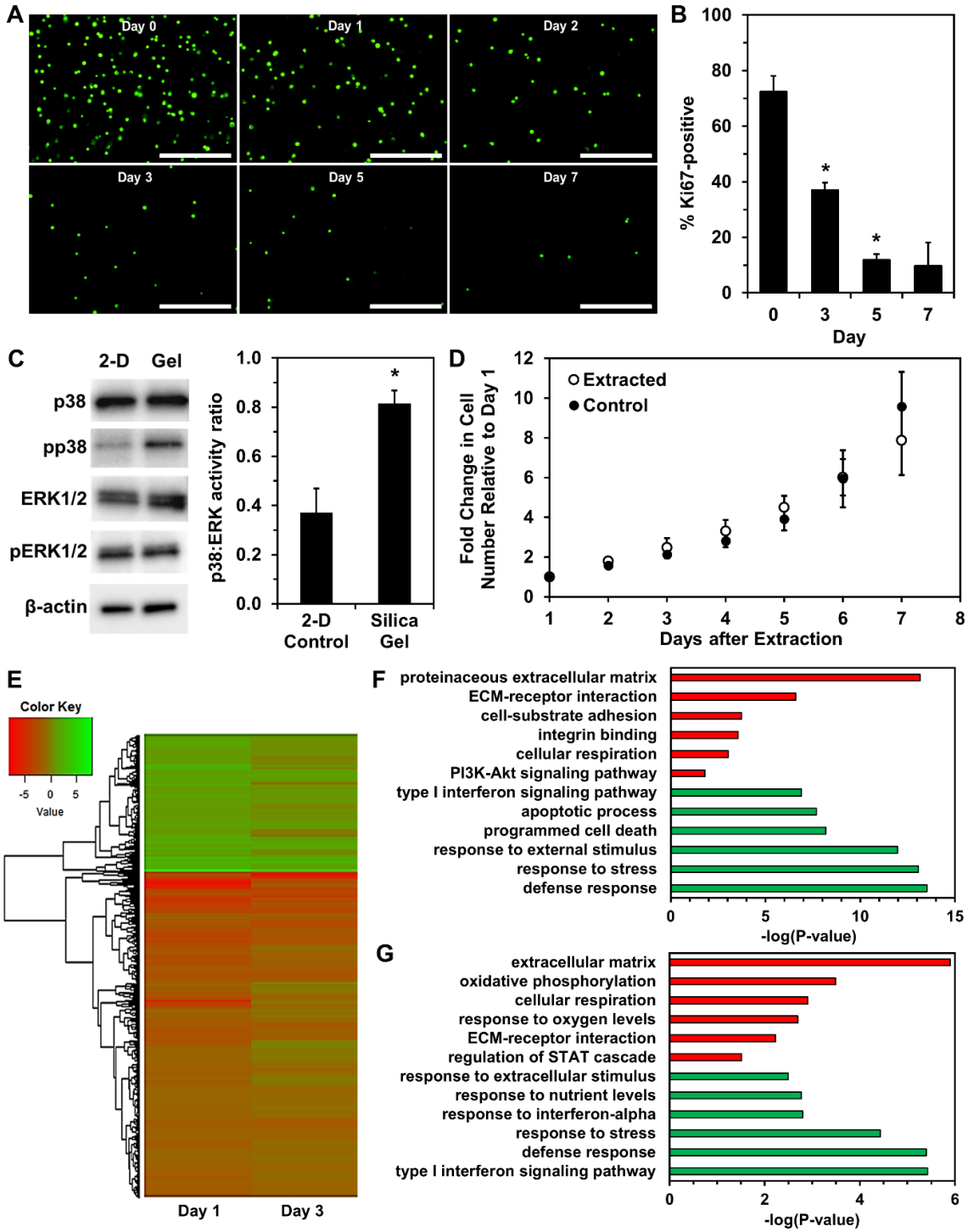

Figure 2.2: Immobilization of OVCAR-3 cells in silica gels results in survival of cells exhibiting quiescence. (**A**) Fluorescence images of viable cells stained with calcein AM (green) at Days 0, 1, 2, 3, 5, and 7 of immobilization. Scale bar indicates 400 µm. (**B**) Percentage of Ki67-positive cells (number of Ki67-expressing cells normalized to number of DAPI-labeled cells) within silica gels over a one-week period quantified from fluorescence images (*$P < 0.05$ compared to previous timepoint). (**C**) Western blotting of p38 MAPK protein ("p38"), ERK1/2 MAPK

proteins (“ERK1/2”), and their phosphorylated forms (“pp38” and “pERK1/2”) in cells immobilized for three days and control cells grown in standard 2-D culture conditions (*P < 0.05 compared to “2-D Control”). (**D**) Growth of cells extracted from silica gels after immobilization for 3 days and control cells cultured in 2-D. (**E**) Heatmap of log_2FC of gene expression in cells immobilized for one or three days relative to control cells. (**F,G**) Gene ontology enrichment analysis using genes significantly upregulated (green) or downregulated (red) in “Day 1” (**F**) or “Day 3” (**G**) of immobilization relative to 2-D controls.

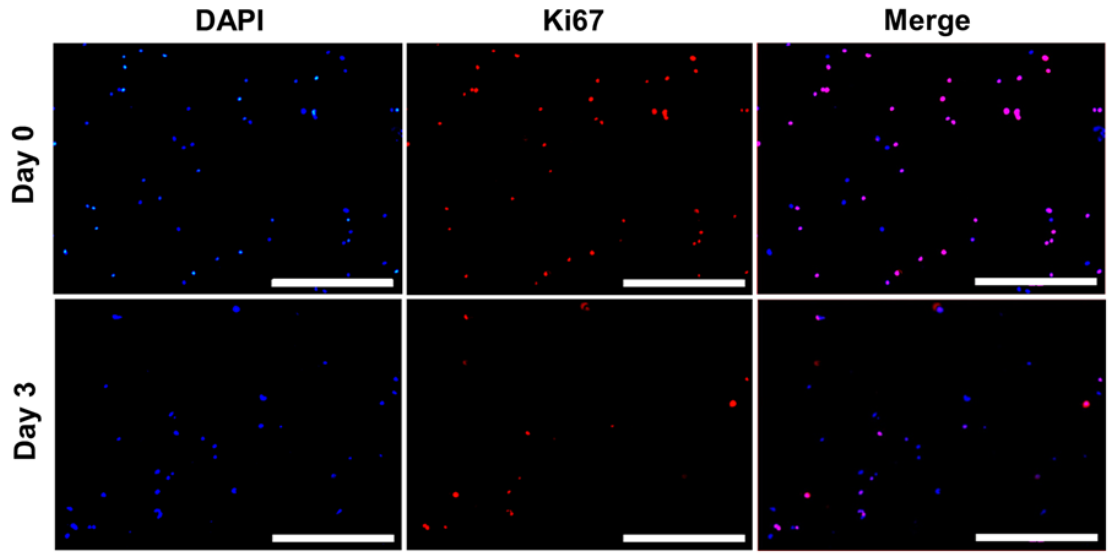

Figure 2.3: Percentage of Ki67-positive OVCAR-3 cells in silica gels decreases over time. Fluorescence images of immunostaining of nuclei (DAPI, blue) and Ki67 (red) at Day 0 and Day 3 of silica gel immobilization. Scale bar indicates 400 µm.

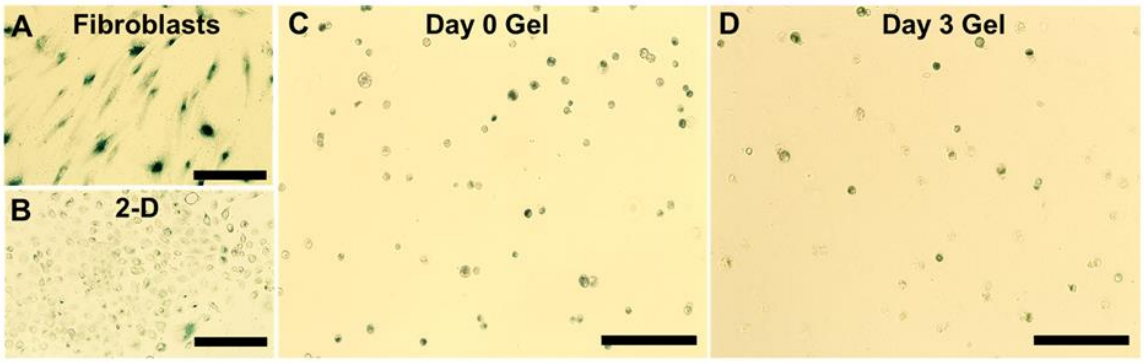

Figure 2.4: Surviving OVCAR-3 cells within silica gels do not exhibit senescence. Senescence-associated β-galactosidase staining was used to label senescent cells. (**A**) Human foreskin fibroblasts at high passage number were used as a positive control. (**B-D**) Images comparing staining of OVCAR-3 cells grown in 2-D (**B**) or immobilized within silica gels at Day 0 (**C**) and Day 3 (**D**) of immobilization. Scale bar indicates 200 µm.

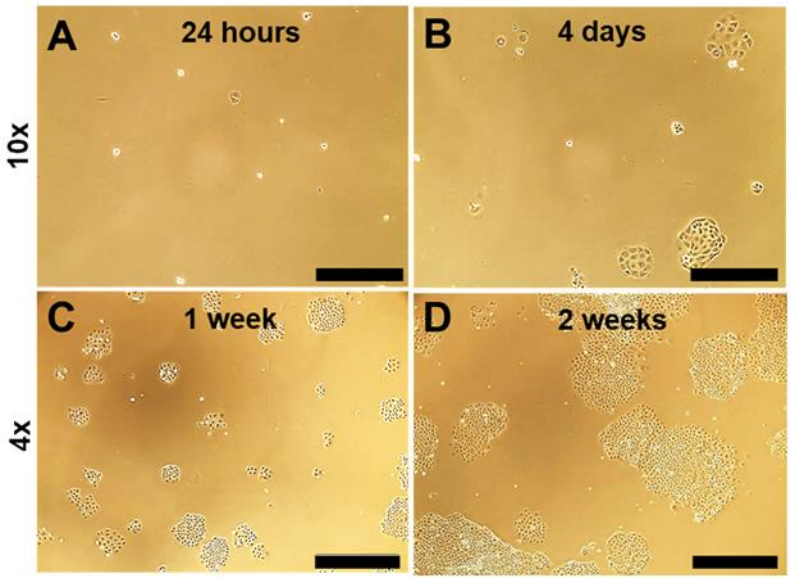

Figure 2.5: Immobilized cells can be extracted from silica gels and resume proliferation after being re-seeded in 2-D culture conditions. Primarily single cells adhered to flasks 24 hours after extraction and continued to grow in small colonies, which was clearly seen by four days post-extraction, and exhibited similar morphology as cells maintained in standard 2-D culture. (**A,B**) Phase-contrast images at 10x magnification of cells on 2-D surface 24 hours (**A**) or 4 days (**B**) after extraction. (**C,D**) Phase-contrast images at 4x magnification 1 week (**C**) or 2 weeks (**D**) after extraction. Scale bar indicates 400 μm and 1000 μm for 10x and 4x images, respectively.

This demonstration of encapsulation in a stiff biomaterial prompting cell cycle exit recapitulates previous studies where gels derived from organic materials, such as collagen[80] or fibrin[81], showed increasing stiffness results in slowed cell growth and metabolism. Here, the silica gels are advantageous as they do not allow for subsequent growth or division once cells are encapsulated, providing a harsh environment that causes most cells to quickly die. Another advantage of these silica gels is that encapsulated OVCAR-3 cells are unable to degrade the silica matrix, while gels derived from natural materials may weaken from enzymatic degradation. Minimal protein amounts in the starting silica gel matrix also provides less sites for cell adhesion and an increasingly difficult environment for these cells, which may result in survival of those more likely to undergo growth arrest and resist

apoptosis. Previously, 3-D bladder cancer spheroids cultured on low-adhesion aminoglycoside-derived hydrogels showed greater cell cycle arrest with increasing storage modulus[82]. Another study has investigated ovarian cancer cell migration, invasion, and growth in cross-linked hyaluronan gels to determine whether the material could inhibit cancer cell adhesion and implantation in the pelvic cavity *in vivo*[118]. Here, we showed the immobilization of cells in stiff silica gels – which also limits their growth and division – results in survival of cells which have entered a dormant state, potentially to tolerate the stress of growth/mitotic inhibition upon confinement.

2.3.2 Immobilization selects for a unique subpopulation with enhanced ability to enter dormancy

To test the hypothesis that immobilization selects for cells with a greater propensity to enter dormancy in order to survive the stress of physical confinement, we re-immobilized cells extracted from the silica gels. Immediately prior to re-immobilization, we confirmed via Ki67 expression that the extracted cells were as proliferative as control cells maintained in 2-D culture (**Fig. 2.6A**). Despite being proliferative just before returning to physical confinement, the extracted cells were found to have enhanced viability upon re-immobilization (**Fig. 2.6B**). These results indicate that immobilization of OVCAR-3 cells selects for a population that may have enhanced pro-survival mechanisms and a greater propensity to enter dormancy within gels.

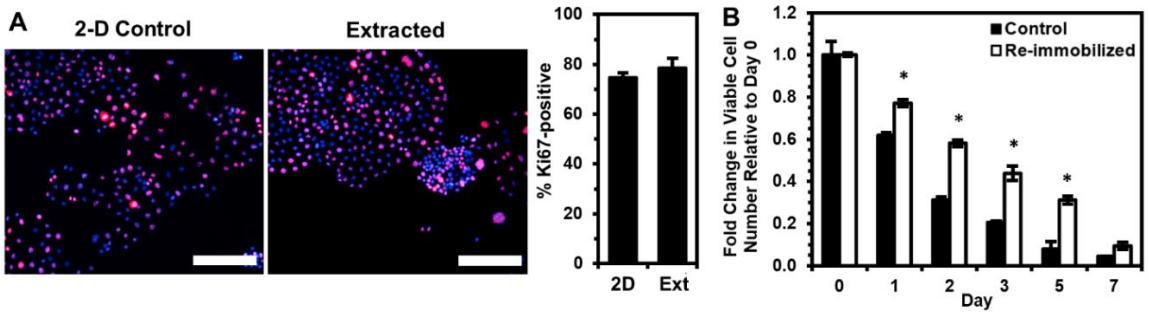

Figure 2.6: Cells surviving silica gel immobilization demonstrate enhanced survival upon re-immobilization relative to the original control population. Cells surviving immobilization for three days were extracted and cultured in 2-D for 1 week prior to immunostaining or re-immobilization. (**A**) Percentage of Ki67-positive cells (number of Ki67-expressing cells (red) normalized to number of DAPI-labeled cells (blue)) from immunofluorescence images (merged images shown) compared to 2-D control cells. Scale bar indicates 200 µm. (**B**) Fold change in viable cell number relative to Day 0 after re-immobilizing extracted cells in silica gels relative to cells immobilized for the first time (Control) (*$P < 0.05$ compared to "Control" for each timepoint).

2.3.3 Silica gel immobilization distinguishes OVCAR-3 cells with enhanced chemoresistance

Because cells immobilized in silica gels exhibited differential gene expression associated with dysregulated cell-substrate interactions, which are also thought to play a role in chemoresistance[60,119], we investigated whether cells with enhanced chemoresistance would exhibit a higher propensity to enter dormancy and survive upon immobilization. To enrich for cells more resistant to platinum chemotherapy, OVCAR-3 cells were treated with 0.5 µM cisplatin for 24 hours, and the surviving cells recovered for two weeks (**Fig. 2.7**). To verify that this procedure selected for chemoresistant cells, recovered cells were re-treated with the same dose of cisplatin, and cell viability after re-treatment ("Second Dose") was compared to viability following initial treatment ("First Dose", **Fig. 2.8A**). Initial treatment caused a significant decrease in viability over a 6-day period, while cells undergoing re-treatment did not exhibit extensive cell death and continued to grow after Day 3, confirming their decreased sensitivity to the chemotherapy. Despite being in a proliferative

state prior to immobilization (**Fig. 2.8B**), after immobilization the cisplatin-resistant cells had markedly enhanced survival relative to untreated cells immobilized in gels (**Fig. 2.8C**), suggesting cells with enhanced chemoresistance may also have greater capacity to enter dormancy when stressed by immobilization and the silica gel environment. Ultimately, these results indicate that silica gel technology could be used as a method to distinguish ovarian cancer cells with enhanced chemoresistance.

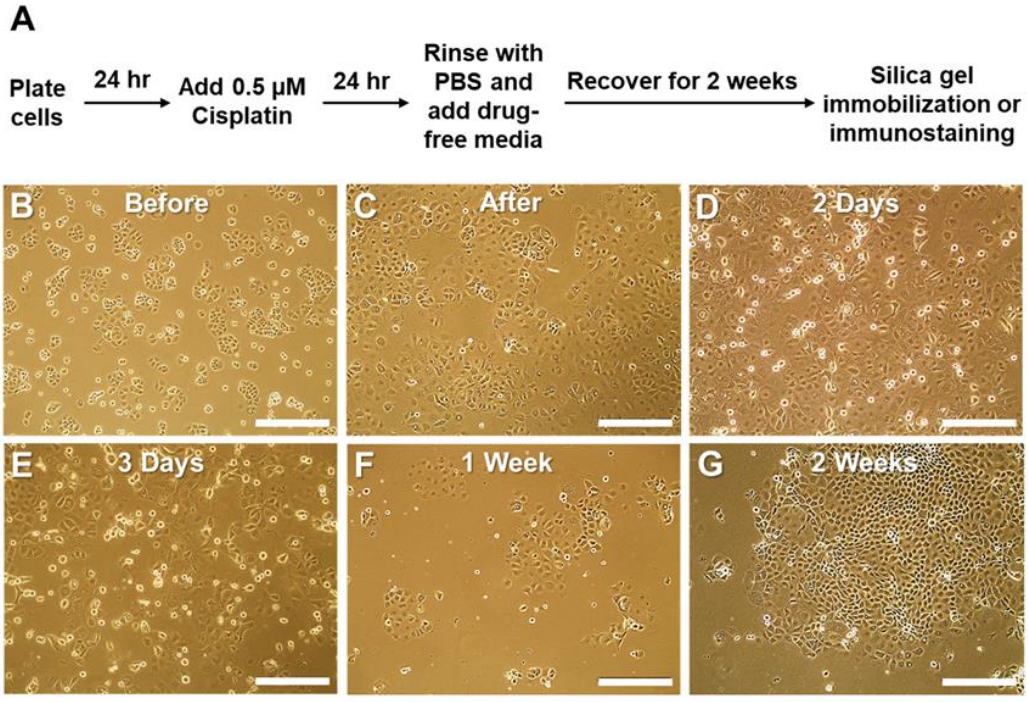

Figure 2.7: OVCAR-3 cells were treated with 0.5 µM cisplatin for 24 hours for significant cell death and recovery of a subset of cells. A 2 week-recovery period was required after drug removal because cells continued to detach and die for up to one week, and it was desired for cells to be back to proliferative state prior to encapsulation. (**A**) Timeline for selection of drug-resistant phenotype prior to silica gel immobilization or immunostaining. (**B-G**) Phase-contrast images of cells before treatment (**B**), immediately after drug was removed (**C**), and 2 days (**D**), 3 days (**E**), 1 week (**F**), and 2 weeks (**G**) after treatment. Scale bars indicate 400 µm.

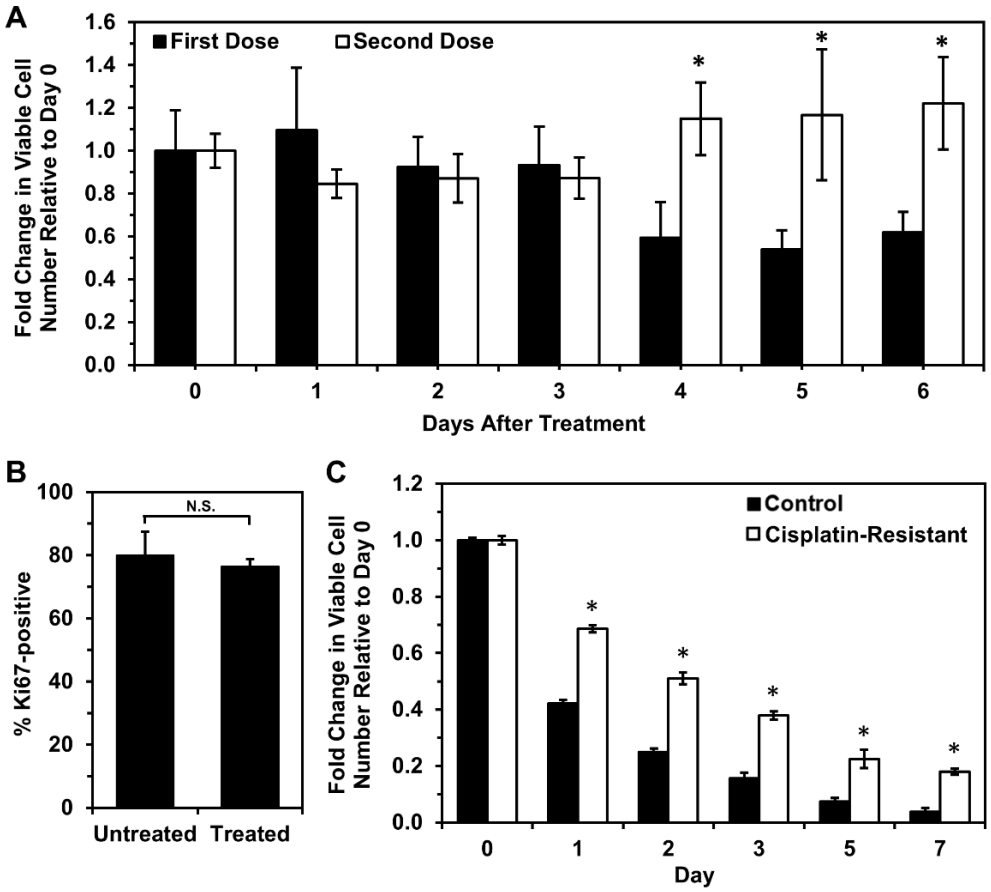

Figure 2.8: Cisplatin-resistant OVCAR-3 cells have higher tolerance for immobilization and silica gel environment. (**A**) Cells retreated with a second dose of cisplatin are less susceptible to treatment than cells undergoing primary treatment, indicating the first dose selected for cisplatin-resistant cells. Each treatment dose was 0.5 μM cisplatin for 24 hours, and cells receiving a second dose were allowed a 2-week recovery period before treatment with the second dose. Viable cell number at Day 0 is the number of live cells counted immediately after drug removal. (*$P < 0.05$ compared to "First Dose"). (**B**) Cisplatin-resistant cells ("Treated", i.e. treated with cisplatin and allowed to recover for 2 weeks) have similar Ki67 expression level as untreated cells. (**C**) Fold change in viable cell number relative to Day 0 of immobilized cisplatin-resistant cells and untreated control cells (*$P < 0.05$ compared to "Control" at each timepoint).

2.3.4 RNA sequencing analysis shows cells surviving silica gel immobilization demonstrate signaling responses associated with chemoresistance

RNA sequencing analysis of cells which survived immobilization in silica gels and were extracted ("Extracted") and cells which survived cisplatin treatment ("Treated") was performed to identify potential mechanisms that allow cells to survive within gels or evade

cisplatin treatment and which of these are shared between the two groups relative to 2-D untreated control cells (**Fig. 2.9A**). Many genes (1,424) were found to be differentially expressed in "Treated" cells relative to the 2-D untreated control, whereas only 328 genes were found to be differentially expressed in "Extracted" cells compared to the 2-D control. More than half of the genes differentially expressed in "Extracted" cells (63.7%, 209 genes) were also differentially expressed in "Treated" cells. Using Ingenuity Pathway Analysis (IPA), the Upstream Regulator function was used to discover transcriptional regulators which best explain the differential gene expression observed within the experimental data. The top 30 upstream regulators predicted to regulate the differential gene expression observed in both "Extracted" and "Treated" samples were primarily drugs or regulators associated with the inflammatory response (**Fig. 2.9B**). Interestingly, cisplatin was predicted as a regulator for "Treated" cells, as expected, but also for "Extracted" cells although they were never previously exposed to cisplatin, indicating that cells extracted from silica gels exhibit signaling responses as if they were treated by platinum chemotherapy. Fibroblast growth factor-2 (FGF-2) was additionally predicted to contribute to gene expression changes in surviving "Extracted" and "Treated" cells, and FGF-2 has previously been implicated as a mediator of chemoresistance by activating downstream survival pathways[120,121] and linked to cellular dormancy in the context of breast cancer[122,123].

GO enrichment analysis of significantly upregulated genes in "Extracted" and "Treated" cells (**Fig. 2.9C&D**) gave terms typically associated with more invasive (e.g. cell motility, migration, chemotaxis) and chemoresistant (e.g. extracellular exosomes/vesicles) phenotypes[124–126]. Exosome and vesicle secretion are important for cell-cell

communication in the tumor microenvironment and are known to regulate metastasis and chemoresistance in cancer[126]. Further, previous work has shown that extracellular vesicles secreted by cisplatin-treated ovarian cancer cells can induce invasion and protection from chemotherapy in other cells pre-treated with these vesicles[127]. In "Treated" cells, defense/stress responses and interferon signaling terms were enriched, which was also observed in "Day 1" and "Day 3" immobilization groups, indicating potential similarities in downstream signaling responses to silica gel immobilization and cisplatin treatment. Genes previously associated with tumor initiating cells or the cancer stem cell theory (e.g. CD133, CD44, CD117, EpCAM, ALDH1A1) were not observed to be consistently and significantly enriched for in experimental groups relative to control cells[37]. Significantly downregulated genes enriched for terms related to the cell membrane, adhesion, and ECM in both "Extracted" and "Treated" cells. Previous studies have shown that cancer cells resisting apoptosis in non-adherent conditions are also more chemoresistant[128–130]. Additionally in ovarian cancer, non-adherent cancer spheroids either created *in vitro* or isolated from *in vivo* ascites fluid also demonstrate enhanced chemoresistance[130–132]. Moreover, ovarian cancer spheroids are thought to be a unique subpopulation of tumor cells with self-renewal capability and enhanced chemoresistance[131].

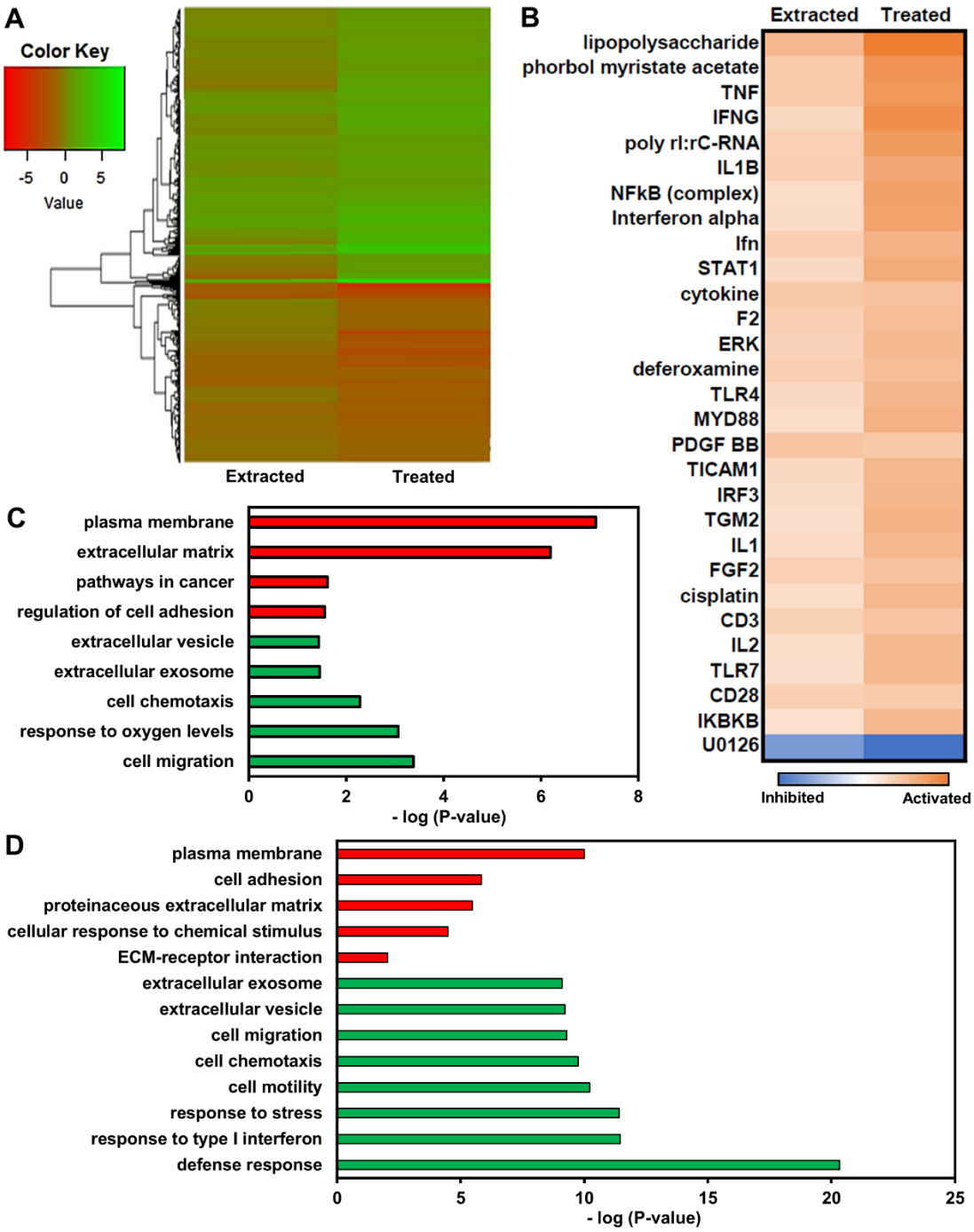

Figure 2.9: OVCAR-3 cells selected by immobilization regulate genes similarly to cells surviving cisplatin treatment. (**A**) Heatmap of $\log_2$FC of gene expression in cells immobilized for three days, extracted, and cultured in standard 2-D conditions for two weeks ("Extracted") and cells surviving treatment with 0.5 μM cisplatin for 24 hours and allowed to recover for 2 weeks in standard 2-D culture conditions ("Treated") relative to control cells. (**B**) List of top 30 common upstream regulators (determined by average Z-score with $P < 0.05$) in "Extracted" and "Treated" cells based upon differentially expressed genes relative to control cells using Ingenuity Pathway Analysis. (**C,D**) Gene ontology enrichment analysis using genes significantly upregulated (green) or downregulated (red) in "Extracted" (**C**) or "Treated" (**D**) samples relative to 2-D controls.

Lastly, we compared the differential gene expression we observed in the "Extracted" population, which has been selected by immobilization to have a higher propensity to enter dormancy, with cancer cells from ovarian cancer patients who responded poorly to chemotherapy. Genes which were found to be significantly up- or downregulated in both the "Extracted" group relative to controls and chemoresistant patients relative to chemosensitive patients by Koti *et al*. and their fold change expression values were used in IPA to identify which pathways were most associated with these genes[99]. Canonical signaling pathways previously associated with poor clinical outcome and response to chemotherapy in ovarian cancer were identified (e.g. STAT3 Pathway, NF-κB Signaling)[133–138], and most notably, pathways responsible for regulation and repair of DNA, which are proposed as key mechanisms of chemoresistance (e.g. NER Pathway, BER Pathway, etc.), were also observed (**Tables 2.2 & 2.3**). Our findings demonstrate that cells extracted from silica gels experienced stresses inducing downstream signaling as if they were treated by cisplatin and display altered regulation of genes associated with pathways known to be important in chemoresistance.

Table 2.2: Canonical signaling pathways identified using Ingenuity Pathway Analysis for differentially expressed genes that were commonly up- or down-regulated between chemoresistant versus chemosensitive patients in Koti *et al.* (2013) and between our OVCAR-3 cells which survived immobilization and were extracted from silica gels ("Extracted") versus control OVCAR-3 cells.

Canonical Signaling Pathway	-log(P-Value)
EIF2 Signaling	8.25
Regulation of eIF4 and p70S6K Signaling	4.48
mTOR Signaling	2.73
Cell Cycle Control of Chromosomal Replication	2.71
Role of BRCA1 in DNA Damage Response	2.4
NER Pathway	2.19
BER pathway	1.85

Table 2.3: Canonical signaling pathways identified using Ingenuity Pathway Analysis for differentially expressed genes that were commonly up- or down-regulated between chemoresistant versus chemosensitive patients from the Koti *et al.* (2013) *in silico* analysis of The Cancer Genome Atlas ovarian cancer patient datasets and between our OVCAR-3 cells which survived immobilization and were extracted from silica gels ("Extracted") versus control OVCAR-3 cells.

Canonical Signaling Pathways	-log(p-value)
Ephrin B Signaling	4.59
Hepatic Fibrosis / Hepatic Stellate Cell Activation	3.36
Antiproliferative Role of Somatostatin Receptor 2	2.74
IL-15 Production	2.37
PTEN Signaling	2.34
STAT3 Pathway	2.28
Corticotropin Releasing Hormone Signaling	2.22
Relaxin Signaling	2.19
Axonal Guidance Signaling	2.17
Cardiac Hypertrophy Signaling (Enhanced)	2.17
Tec Kinase Signaling	2.11
Glioblastoma Multiforme Signaling	2.10
NF-κB Signaling	2.04
Synaptic Long Term Depression	2.00
IL-8 Signaling	1.95
Role of NFAT in Cardiac Hypertrophy	1.89
Sperm Motility	1.87
Huntington's Disease Signaling	1.80
Cardiac Hypertrophy Signaling	1.79
Colorectal Cancer Metastasis Signaling	1.75
Sonic Hedgehog Signaling	1.62
G Protein Signaling Mediated by Tubby	1.60
Inhibition of Angiogenesis by TSP1	1.56
Ephrin A Signaling	1.42
Protein Kinase A Signaling	1.39
Glutamate Receptor Signaling	1.34
PCP pathway	1.32
Wnt/Ca+ pathway	1.31

2.3.5 OVCAR-3 cells selected by silica gel immobilization exhibit enhanced chemoresistance even when proliferative

Because RNA sequencing analysis showed a significant overlap between dormancy-capable cells and chemoresistant phenotypes, we investigated whether dormancy-capable cells would be more resistant to cisplatin chemotherapy. Surviving OVCAR-3 cells were extracted from silica gels following three days of immobilization, and one week post-extraction they were treated with 0.5 μM cisplatin for 24 hours (**Fig 2.10A, Scheme i**). These extracted (dormancy-capable) cells demonstrated enhanced resistance to cisplatin

treatment – despite being proliferative (**Fig. 2.6A**) – relative to control cells which were never previously encapsulated (**Fig. 2.10B**). Interestingly, when OVCAR-3 cells induced into quiescence via hypoxia[96,139] or serum starvation[97] were treated with cisplatin, these cells exhibited enhanced chemoresistance (**Fig. 2.11**), consistent with earlier reports [61,140,141]. However, after returning to a proliferative state upon removal of the stress (**Fig. 2.10A, Scheme ii**), these cells no longer had a survival advantage upon cisplatin treatment (**Fig. 2.10C&D**). These results demonstrate the uniqueness of physical confinement stress in silica gels, as it selects for cells which are chemoresistant even after the stress is lifted. This is further supported by our RNA sequencing analysis of "Extracted" cells, which demonstrated they regulate genes as if they had been treated with cisplatin and exhibit downstream signaling similar to "Treated" cells which survived cisplatin chemotherapy. It is possible that silica gels are a significantly harsher environment than hypoxia or serum starvation, and the stresses of physical confinement cause the majority of encapsulated cells to die, allowing for more efficient selection. Further, extracted cells may have enhanced chemoresistance due to mechanisms induced by growth inhibition and dysregulated cell-ECM substrate interactions experienced within gels. These cells may be able to mitigate pro-apoptotic signals that would be initiated under these stressful conditions and may instead sustain pro-survival pathways. The ability to resist programmed cell death would also be useful in resisting DNA damage-induced apoptosis via chemotherapy and could be a potential means for cells surviving confinement to also survive cisplatin treatment. Whether cells selected by immobilization are a unique subpopulation with innate capabilities or whether survival within silica gels is a learned adaptation by cells remains an important question for future study.

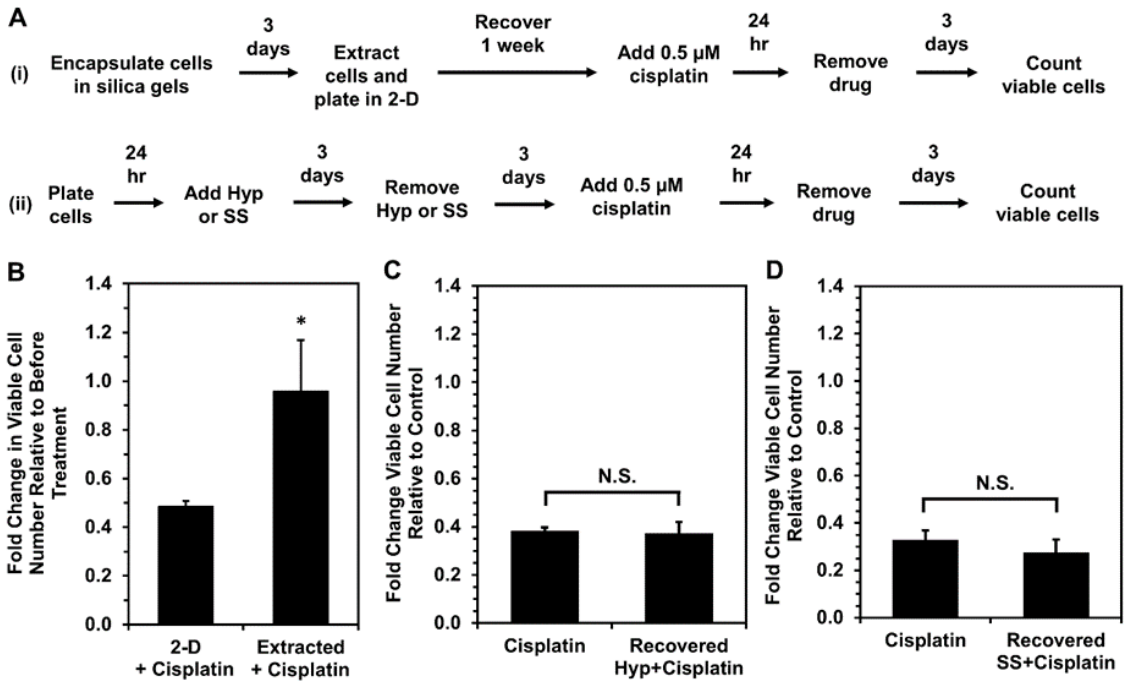

Figure 2.10: Silica gel immobilization selects for cells that are more chemoresistant even while proliferative. (**A**) Timeline for cisplatin treatment studies of cells either (**i**) surviving silica gel immobilization or (**ii**) recovered from hypoxia treatment or serum starvation. Recovery periods of three days after hypoxia or serum starvation and one week post-extraction allowed for similar cell densities and return to a proliferative state at the start of cisplatin treatment. (**B**) Response to cisplatin treatment of cells surviving silica gel immobilization ("Extracted+Cisplatin") relative to cells maintained in 2-D culture conditions ("2-D+Cisplatin"). Fold change in viable cell number indicates cell number at Day 3 post-cisplatin treatment relative to cell number before drug treatment (*$P < 0.05$ relative to 2-D). (**C,D**) Fold change in viable cell number for cells recovered from (**C**) hypoxia ("Recovered Hyp+Cisplatin") or (**D**) serum starvation ("Recovered SS+Cisplatin") and treated with 0.5 µM cisplatin for 24 hours relative to proliferating cells grown in standard culture conditions ("Cisplatin") after treatment. Fold change in viable cell number indicates cell number at Day 3 post-cisplatin treatment relative to untreated controls for each respective condition (*$P < 0.05$ compared to "Cisplatin").

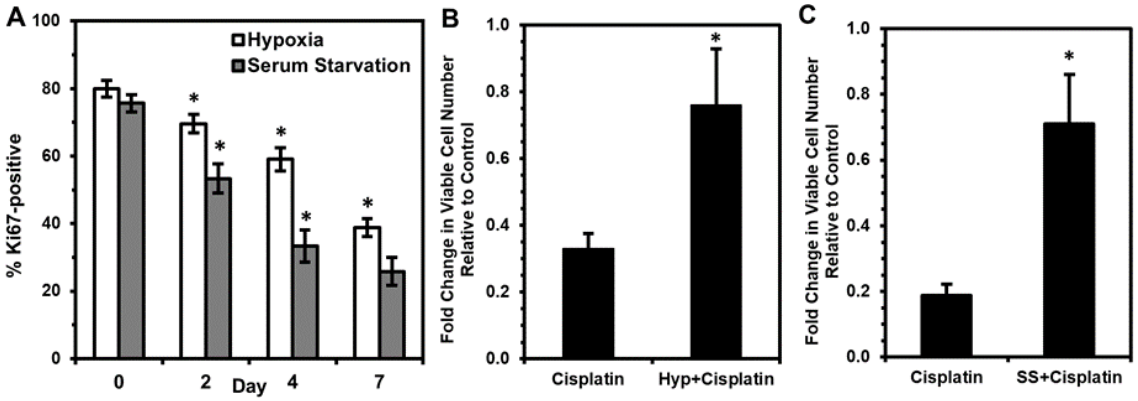

Figure 2.11: OVCAR-3 cells induced into a quiescent state are less susceptible to cisplatin treatment. (**A**) Percentage of Ki67-positive cells (number of Ki67-expressing cells normalized to number of DAPI-labeled cells) in cells cultured in 1% oxygen ("Hypoxia") or serum-free media ("Serum Starvation") conditions over a one-week period (*P < 0.05 compared to previous timepoint). Quiescent cells were obtained by culturing cells in 1% oxygen conditions or serum-free media for 3 days prior to drug addition. (**B,C**) Comparison of fold change in viable cell number for (**B**) hypoxia-treated cells ("Hyp+Cisplatin") or (**C**) serum-starved cells ("SS+Cisplatin") against cells grown in standard 10% FBS-supplemented media conditions ("Cisplatin") following treatment with 0.5 μM cisplatin for 24 hours. Fold change in viable cell number indicates cell number at Day 3 post-cisplatin treatment relative to untreated controls for each respective condition (*P < 0.05 compared to "Cisplatin").

2.3.6 Silica gel platform distinguishes cells with enhanced chemoresistance in other cell lines and towards taxane agents

SKOV-3, another commonly used ovarian cancer model cell line for drug treatment study, ovarian adenocarcinoma cells were immobilized in silica gels to ensure that selection of cells with quiescent behavior and enhanced chemoresistance was not specific to OVCAR-3 cells. The number of viable SKOV-3 cells significantly decreased over time once immobilized in silica gels (**Fig. 2.12A**). The percentage of Ki67-positive SKOV-3 cells also decreased over time in gels (**Fig. 2.12B**), and surviving cells could be extracted and cultured in 2-D. SKOV-3 cells are known to be more resistant to cisplatin than OVCAR-3 cells[142] and required a higher dose (5 μM) of cisplatin for significant cell death with recovery of a small chemoresistant subpopulation. Upon immobilization in silica gels, this cisplatin-resistant SKOV-3 cell population exhibited enhanced survival relative to control

cells with no previous drug treatment (**Fig. 2.12C**), consistent with the OVCAR-3 results. In separate studies, SKOV-3 cells surviving immobilization (dormancy-capable) were extracted from gels and found to have decreased sensitivity to cisplatin (**Fig. 2.12D**) along with enhanced viability upon re-immobilization (**Fig. 2.12E**), similar to OVCAR-3 cells. These results demonstrate that silica gel technology may be used to select for cells with enhanced chemoresistance and propensity to enter dormancy across ovarian cancer cell lines and may even show promise for application towards other cancer types.

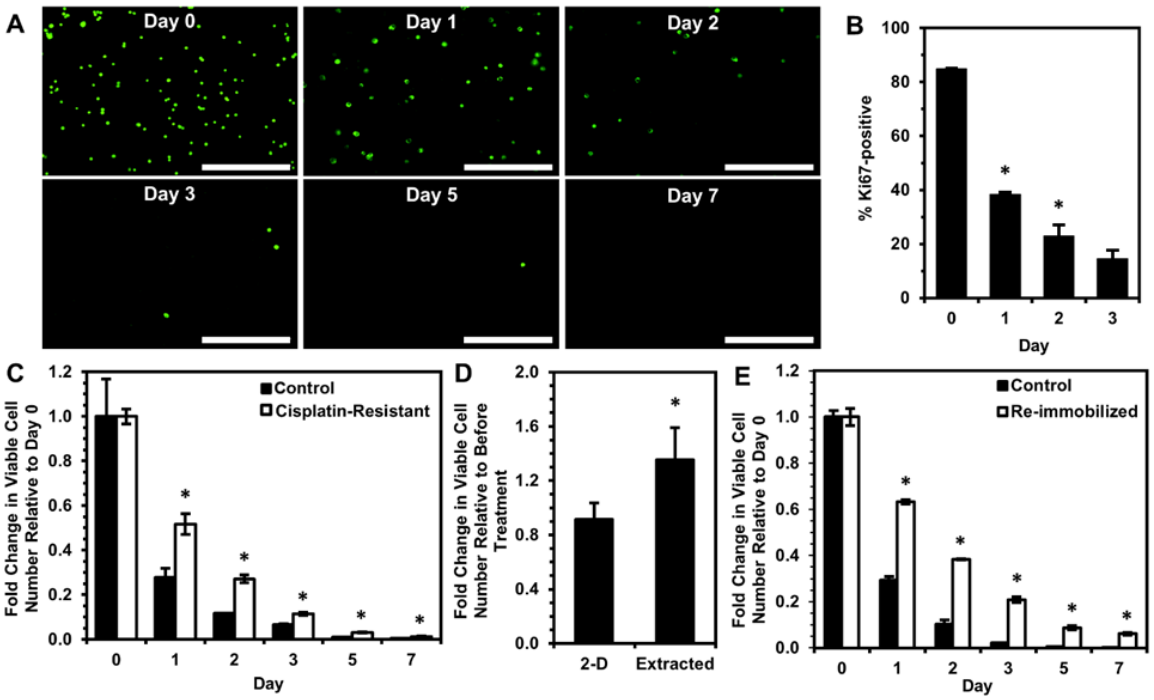

Figure 2.12: Selection of unique subpopulation via silica gel immobilization is also observed with SKOV-3 ovarian cancer cell line. (**A**) Calcein AM staining of viable SKOV-3 cells (green) immobilized for 0, 1, 2, 3, 5, and 7 days within silica gels. Scale bar indicates 400 µm. (**B**) Percentage of Ki67-positive SKOV-3 cells within silica gels over a three-day period (*P < 0.05 compared to previous timepoint). (**C**) Fold change in viable cell number relative to Day 0 of immobilized cisplatin-resistant SKOV-3 cells and untreated control cells (*P < 0.05 compared to "Control" at each timepoint). (**D,E**) SKOV-3 cells surviving immobilization for 24 hours were extracted and cultured in 2-D for 1 week and used to find (**D**) the fold change in viable cell number three days after 5 µM cisplatin treatment for 24 hours relative to before treatment (*P < 0.05 compared to "2-D") and (**E**) the fold change in viable cell number relative to Day 0 after re-immobilizing extracted SKOV-3 cells in silica gels relative to proliferating cells immobilized for the first time (Control) (*P < 0.05 compared to "Control" at each timepoint).

The taxane-based chemotherapeutic paclitaxel was also investigated in combination with silica gel immobilization, as addition of taxane agents in combination with platinum chemotherapy has been the standard regimen for the last decade[143]. OVCAR-3 cells extracted from silica gels were found to have decreased susceptibility to paclitaxel treatment relative to 2-D control cells, even though these extracted cells were proliferating at time of paclitaxel addition (**Fig. 2.13A**). Again, this result demonstrates that the subpopulation surviving immobilization has enhanced chemoresistance but not only towards platinum-based agents. Further, treatment of OVCAR-3 cells with paclitaxel followed by a two-week recovery period allowed for selection of a more paclitaxel-resistant population (**Fig. 2.14**). This population demonstrated significantly enhanced survival relative to untreated cells upon immobilization in silica gels (**Fig. 2.13B**), further demonstrating the ability of silica gels to identify ovarian cancer cells less susceptible to multiple types of chemotherapy.

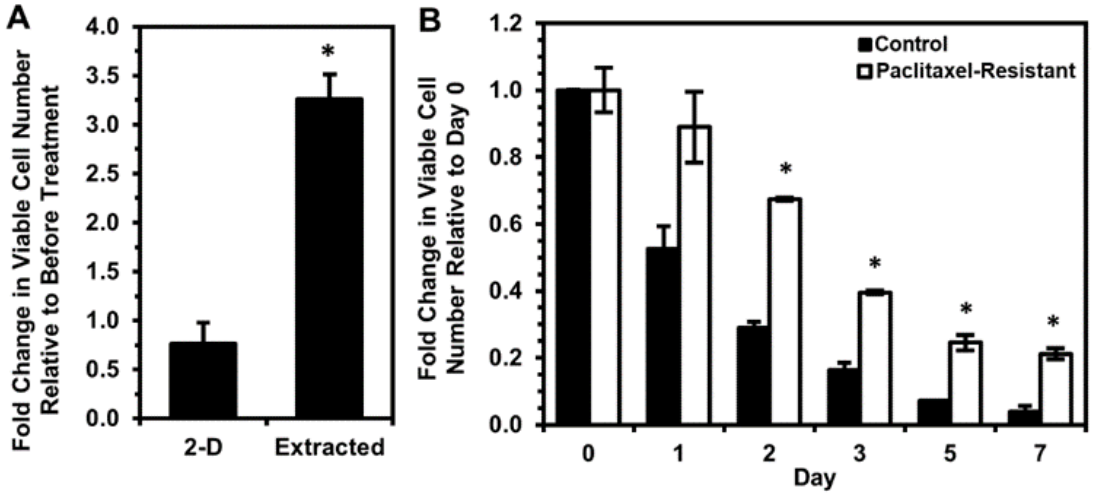

Figure 2.13: Extracted cells are less sensitive to paclitaxel, and paclitaxel-resistant cells exhibit enhanced survival upon immobilization. (**A**) Fold change in viable OVCAR-3 cell number three days after 30 nM paclitaxel for 24 hours relative to before treatment (*P < 0.05 compared to "2-D"). (**B**) Fold change in viable cell number relative to Day 0 of immobilized

paclitaxel-resistant OVCAR-3 cells and untreated control cells (*P < 0.05 compared to "Control" at each timepoint).

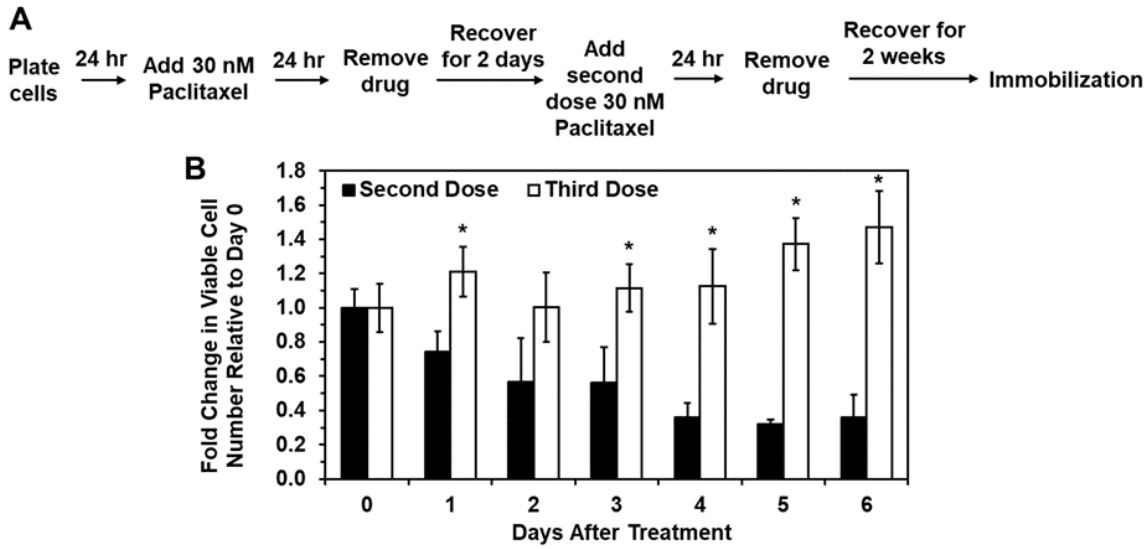

Figure 2.14: OVCAR-3 treatment with multiple doses of paclitaxel results in survival of a subset of cells that can recover and are less susceptible to an additional round of treatment. (**A**) Timeline for selection of more paclitaxel-resistant phenotype prior to silica gel immobilization. (**B**) Cells treated with a third dose of paclitaxel are less susceptible to treatment than cells undergoing secondary treatment. Each treatment dose is 30 nM paclitaxel for 24 hours, and cells receiving the third dose were allowed a 2 week-recovery period before treatment with the third dose. Viable cell number at Day 0 is the number of live cells counted immediately after drug removal. (*P < 0.05 compared to "Second Dose").

These last findings demonstrate the broad applicability of our physical confinement approach using stiff silica gels to investigate a unique subset of cells exhibiting dormant behavior upon immobilization and enhanced chemoresistance once removed from gels. We also showed cells surviving immobilization and extracted from silica gels were found to have enhanced viability upon re-immobilization, indicating these cells are distinct from the original population. Further, RNA sequencing analysis revealed that extracted cells also exhibit downstream signaling activity as if previously exposed to cisplatin, and differentially expressed genes resulted in terms associated with a more chemoresistant phenotype using GO analysis. While cells released from quiescence using other *in vitro*

platforms did not exhibit enhanced chemoresistance, cells selected by silica gels were less susceptible to platinum and taxane agents despite being in a proliferative state. This finding provides evidence that cells which have an enhanced ability to enter dormancy, not just cells that are quiescent at the time of treatment, may be a primary cause of chemoresistance. Future studies investigating pathways initiated by cells surviving immobilization which are also common to cells surviving cisplatin treatment could further elucidate the interplay between ability to enter dormancy and chemoresistance and ultimately identify new therapeutic targets for ovarian cancer. Moreover, as our results showed distinct behavior of cisplatin- and paclitaxel-resistant cells upon immobilization, future work immobilizing ovarian cancer cells isolated from patient biopsies would determine whether silica gels could be a facile method for identifying patients with increased risk of recurrence.

Chapter 3: Iron oxide-loaded polymer scaffolds for non-invasive hyperthermic treatment of infiltrated cells

3.1 Introduction

Another clinical challenge in ovarian cancer treatment is the lack of alternative treatment options to chemotherapy. However, an innovative modality that may be promising for ovarian cancer and could address chemoresistance and recurrence is focal therapy. Focal therapy consists of using energy-based methods such as hyperthermia/thermal ablation, cryoablation, and irreversible electroporation to kill cells and has garnered interest as an innovative treatment modality for cancer[144–147]. Further, hyperthermia and thermal ablation modalities are credited as minimally invasive or non-invasive ways to treat tumors and can also aid in stimulating an immune response against the killed cancer cells[144,145]. In hyperthermia and thermal ablation, high temperatures in a localized region are used to denature essential cellular proteins and damage tissue/vasculature structures, with cell damage and death depending on both the temperature during treatment and the duration of treatment[148]. Hyperthermic treatments rely on maintaining therapeutic temperatures of roughly 43 to 47 °C for tens of minutes to hours, while thermal ablation is a more rapid process with temperatures in excess of 50 °C and treatment times on the order of minutes. These methods have previously been used to treat localized solid tumors in the liver,

kidney, lung, breast, prostate, and bone[144]. However, although these approaches have shown success towards treating solid tumors, they cannot be readily applied to cancers that are often in a disseminated form, such as ovarian cancer. As mentioned in Chapter 1, ovarian cancer is often not diagnosed until it has reached an advanced stage, where cancer cells are often dispersed throughout the abdominal cavity of the patient[22,73]. The disseminated nature of this disease has made treatment difficult, and while the overall survival rate for ovarian cancer patients is only 20 to 30%[143], patients whose cancer is confined to the ovaries have a better prognosis, with up to 90% being cured with existing treatments[4].

A potential way to apply focal therapy to advanced stage ovarian cancer is to use a biomaterial implant to localize disseminated cells to a targetable site prior to treatment. Previous studies have demonstrated that porous scaffolds fabricated from poly(lactide-co-glycolide) or poly(ε-caprolactone) (PCL) could recruit and capture metastatic breast cancer cells *in vivo*[76,77]. Further, De la Fuente *et al.* implanted polystyrene/PCL-based scaffolds in the intraperitoneal cavity of mice and observed localization of SKOV-3 ovarian cancer cells at the scaffold, resulting in a decrease in tumor cell number at metastatic sites such as the pancreas and gonadal fat pad in a disseminated ovarian cancer model[75]. It was also shown that addition of recruitment moieties to the scaffold enhanced localization of disease, and its subsequent surgical removal significantly enhanced survival, likely by lowering the disease burden within the body[75]. However, another strategy in which the localized cancer cells could be destroyed at the scaffold site *in situ* using hyperthermic treatment would be advantageous to minimize additional invasive procedures. Furthermore, by destroying the cancer cells *in situ* using hyperthermia, the immune system

then has the ability to recognize cancer-specific antigens and garner anti-tumor immunity[145]. Overall, coupling focal therapy with biomaterial implants is desirable so that cancers which do not present in the form of a primary tumor (e.g. blood cancers) or are often disseminated (e.g. ovarian cancer) can be susceptible to this type of treatment.

Previous studies have demonstrated the ability to incorporate energy-absorptive materials within a biomaterial implant for successful heating. *In vitro* killing of HeLa cervical cancer cells has been shown using NIR laser irradiation of gelatin and gold nanoparticle composite scaffolds[149]. Studies with alginate hydrogels loaded with polydopamine and element-doped bioactive ceramic glass scaffolds have also exhibited successful *in vivo* destruction of breast and bone cancers, respectively[150,151]. More recently, focal therapy methods have been coupled with biomaterial scaffolds which have previously been used to recruit metastatic cancer cells. Non-invasive hyperthermia treatment of infiltrated cells was successfully completed *in vivo* using porous PCL scaffolds with an embedded aluminum disk under an alternating magnetic field[85]. Although heating of cells within the scaffold was achieved, the temperature gradient resulting from a single thermal seed at the center of the cylindrical scaffold requires longer treatment times to reach therapeutic temperatures at the radial edge of the scaffold and results in elevated temperatures in a significant region of surrounding tissue due to the scaffold geometry. Because of this drawback, we sought to investigate a scaffold design that still utilizes the advantages of non-invasive hyperthermia but exhibits more uniform heating via a distributed heat source throughout the PCL scaffold.

Magnetic materials have been investigated for thermal treatment in cancer, where magnetic nanoparticles are injected systemically or directly into the tumor and will generate heat in

the presence of an alternating magnetic field[152]. Numerous types of magnetic nanoparticles have been investigated including ones derived from cobalt, nickel, and iron; however, iron oxide is most commonly used because of its high magnetic moment and superior biocompatibility in comparison to other materials[153,154]. Initial studies characterizing magnetic particle heating carried out by Gilchrist *et al*. demonstrated that iron oxide was the most promising and exhibited no significant cytotoxic effects when administered to the lymph nodes in canines[155]. Since then, iron oxide particles alone or with various coatings (e.g. dextran, starch, amino-silane) have also been investigated for heating capability under alternating magnetic fields in the context of glioma[156], breast[157–159], and prostate cancers[160,161]. Furthermore, iron oxide has previously been incorporated into 3-D printed mesoporous bioactive glass/PCL scaffolds, resulting in heating when placed in an alternating magnetic field[162]. The clinical feasibility and safety of thermal therapy using iron oxide particles in humans has also been investigated. Prostate cancer patients received intratumoral delivery of iron oxide particles and were treated weekly for six weeks under an alternating magnetic field, and therapeutic temperatures were achieved within the tumors, demonstrating feasible clinical hyperthermia treatment using iron oxide[163,164]. In patients exhibiting recurrent glioblastoma multiforme, iron oxide delivered intracranially provided increased intratumoral temperatures under an alternating magnetic field with minimal or no adverse side effects[165]. Iron oxide has also been widely used for other biomedical and cancer applications such as MRI/diagnostics and drug delivery, demonstrating both its vast utility and safety in the clinic[166].

Given the ability to non-invasively generate heat from iron oxide under an alternating magnetic field and its widespread biomedical applications, we sought to incorporate iron

oxide into microporous PCL scaffolds previously shown to recruit disseminated breast cancer cells. Upon facile incorporation of bulk iron oxide particles into our scaffold fabrication protocol, iron oxide-loaded scaffolds exhibited magnetic behavior and heating under an alternating magnetic field, and ID8 ovarian cancer cells were successfully killed within these scaffolds *in vitro*. Further, iron oxide-loaded scaffolds were implanted into the intraperitoneal cavity of female mice and non-invasive hyperthermic treatment of cells within iron oxide-loaded scaffolds was demonstrated. These results show non-invasive hyperthermia can be used with a biomaterial scaffold in the intraperitoneal cavity, and iron oxide-loaded scaffolds could be used as a novel treatment modality towards disseminated ovarian cancer cells in the future.

3.2 Materials and Methods

3.2.1 Fabrication of iron oxide-loaded scaffolds

For PCL-only and iron oxide-loaded scaffolds, PCL microspheres were fabricated as described previously[77]. Iron oxide-loaded PCL scaffolds were fabricated by mixing the desired amount of iron oxide powder (0.5 to 2.0 mg of spherical, < 44 μm Fe_3O_4 particles, Lansco 8330M) with 3 mg PCL microspheres and 90 mg (250-425 μm) sieved salt particles then thoroughly mixed. The mixture was loaded into a 5 mm steel die (Specac) and then pressed to 1000 PSI for 45 seconds using a mechanical press. Scaffold disks were then heated at 60 °C for 5 minutes on each side prior to gas foaming overnight. PCL-only or iron oxide-loaded scaffolds were placed in deionized water on a shaker for 1.5 or at least 3 hours, respectively, to leach out the salt. Lastly, all scaffolds were sterilized in 70% ethanol, rinsed with sterile water, and dried prior to storage before use in experiments.

3.2.2 Scanning electron microscopy (SEM)

Cross-sections of iron oxide-loaded scaffolds were coated with a 10 nm-thick palladium layer using an EM ACE600 sputter coater (Leica) and then imaged using a cold field emission gun scanning electron microscope (Hitachi S-4700, Hitachi High-Technologies Corp.) at 5000 V accelerating voltage.

3.2.3 Radiofrequency heating studies

To generate an alternating magnetic field (10.0, 20.8, and 30.5 kA/m), a 1 kW inductive heating system with a water-cooled, 2.75 turn copper coil was used (Ameritherm Inc.). Iron oxide-loaded scaffolds were placed in 1 mL of deionized water in a cryovial wrapped in nitrile foam insulation to decrease the amount of conductive heating from the coil, and it was positioned so that the scaffold was in the center of the coil (**Fig. 3.1**). A fiber optic temperature probe (Qualitrol Company LLC) was placed in the center of the scaffold and used to measure temperature over time. Any background temperature rise from these studies, as measured in a deionized water blank, was subtracted for the final results. All tests for these studies were 15 minutes in duration.

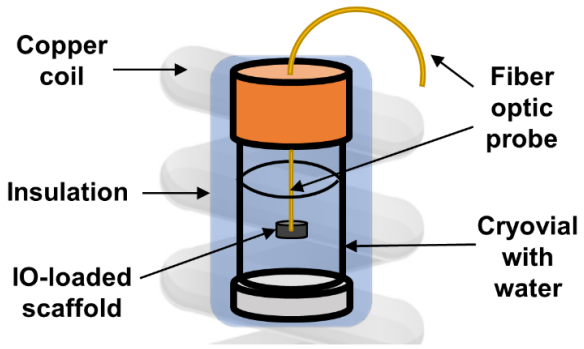

Figure 3.1: Schematic of experimental setup for temperature rise studies. Iron oxide-loaded scaffolds were placed in 1 mL of deionized water inside a cryovial and positioned to be at the center of a water-cooled copper coil (gray). A fiber optic temperature probe (yellow) was placed through the center of the scaffold, and nitrile foam insulation (blue) was placed between the coil and the cryovial.

3.2.4 In vitro cytotoxicity studies

Mouse ID8 ovarian cancer cells were a kind gift from Dr. Katherine Roby[167] and were cultured in Dulbecco's Modified Eagle's Medium (Millipore Sigma D6429) with 4% fetal bovine serum (Thermo Fisher Scientific), 1% insulin-transferrin-sodium selenite supplement (Millipore Sigma), and 1% penicillin-streptomycin (Thermo Fisher Scientific). For each scaffold, 100,000 ID8 ovarian cancer cells in 20 µL of 5 mg/mL Matrigel (Corning) solution were loaded onto sterilized PCL-only or iron oxide-loaded scaffolds and placed in a 37 °C and 5% CO_2 incubator for 5 minutes. Cell-loaded scaffolds were then moved to wells of a 48-well plate with fresh ID8 culture media and stored in the incubator until assay timepoints.

At each timepoint for the AlamarBlue assay, the culture media surrounding scaffolds was carefully aspirated, and 300 µL of 10% AlamarBlue solution (Thermo Fisher Scientific), diluted in fresh ID8 culture media, was added to each well. After incubation under 37 °C and 5% CO_2 for 1 hour, 100 µL of the AlamarBlue solution was collected and placed in a well of a black 96-well plate. Fluorescence of each sample was read with 560 nm excitation and 590 nm emission using a BioTek Synergy H1 microplate reader. Remaining AlamarBlue solution was aspirated from the wells and fresh ID8 culture media was added.

3.2.5 Iron release (Ferrozine) assay

Iron oxide-loaded scaffolds were placed in 1 mL of phosphate buffered saline (PBS, Thermo Fisher Scientific) in a 24-well plate placed under 37 °C and 5% CO_2 conditions. Every 7 days, all of the PBS solution was collected and stored at 4 °C, and 1 mL of fresh PBS was carefully added to each well. After 6 weeks, the iron oxide-loaded scaffolds were

then transferred to fresh PBS and treated under an alternating magnetic field for 15 minutes at 30.5 kA/m and 360 kHz, and the PBS solution after treatment was collected for testing.

Following the manufacturer's protocol, the Iron Colorimetric Assay Kit (Ferrozine Method) from AdipoGen (JAI-CFE-005) with a sensitivity range of 5 – 1000 µg/dL was used to investigate the amount of iron released. Briefly, 40 µL of blank (distilled water), standard, or sample was added in triplicate to a clear flat bottom 96-well plate. 200 µL of R-1 reagent was added to each well and incubated for 5 minutes at room temperature, followed by reading the absorbance of each well at 560 nm using a BioTek Synergy H1 microplate reader. 8 µL of R-2 reagent was then added to each well and incubated for 5 minutes at room temperature, and a second reading of absorbance values at 560 nm was taken.

3.2.6 In vitro and ex vivo heating studies

For *in vitro* heating studies, 400,000 ID8 ovarian cancer cells in 20 µL of 5 mg/mL Matrigel solution were loaded onto sterilized scaffolds and placed in a 37 °C and 5% CO_2 incubator for 5 minutes. For *ex vivo* heating studies, tissue-laden iron oxide-loaded scaffolds were collected from the intraperitoneal cavity of mice 6-7 weeks post-implantation. Negative control scaffolds for cell death ("IO no heat") were left in standard culture conditions at 37°C and 5% CO_2 in ID8 culture media. Scaffolds receiving hyperthermic treatment ("IO heat") were placed in 1 mL of PBS and placed in the presence of an alternating magnetic field for 15 minutes at 30.5 kA/m and 360 kHz.

To determine cell viability, a WST-1 assay was used. Each scaffold was minced with microscissors in 500 µL of fresh ID8 culture media with 50 µL WST-1 reagent (Takara

Bio) in a 48-well plate and incubated at 37 °C and 5% CO_2 for 1.5 hours. After incubation, the samples were centrifuged, and 400 µL of the supernatant solution was passed through a 70 µm mesh filter (Corning). Supernatant absorbance for each scaffold and media only controls (500 µL of fresh ID8 culture media with 50 µL WST-1 reagent incubated for 1.5 hours) was read in triplicate at 440 nm using a BioTek Synergy H1 microplate reader.

3.2.7 Scaffold implantation and in vivo heating

All animal studies were approved and conducted following the guidelines under the University of Minnesota's Institutional Animal Care and Use Committee. Female C57BL/6J mice were purchased from The Jackson Laboratory and were around 7-8 weeks old at time of scaffold implantation. For surgical implantation of scaffolds, mice were anesthetized and laid on their back so an incision at the abdominal midline could be made in the skin, followed by an incision in the peritoneal wall. One PCL-only or iron oxide-loaded scaffold was carefully placed adjacent to the intraperitoneal side of the wall to the left of the incision, and then the peritoneal wall and skin were each closed with sutures. For *in vivo* heating studies, mice with iron oxide-loaded scaffolds implanted for 6-7 weeks were anesthetized, and the hair on the belly was removed to visually locate the iron oxide-loaded scaffolds under the layers of skin. Anesthetized mice were carefully placed on their back underneath the copper coil on a height-adjustable platform. Due to the size constraints of the coil (1.75 cm inner diameter), this placement of the mice was used to position the scaffold located in the intraperitoneal cavity as close to the center of the coil as possible. For each mouse, the treatment period was 15 minutes at 26.4 ± 0.5 kA/m and 360 kHz fields, and the magnetic field strength at this position (~ 1-2 mm beneath the bottom of coil) was determined using a 2D HF Magnetic Field Probe (AMF Life Systems) and

TDS2002 Digital Oscilloscope (Tektronix). Treated scaffolds were harvested 3 days post-treatment for histological analysis.

3.2.8 Histological analysis

Scaffolds implanted in the intraperitoneal cavity of mice were harvested for histological analysis and immediately placed in 10% buffered formalin solution (Millipore Sigma) at least overnight prior to transfer to 70% ethanol and embedding in paraffin blocks. Scaffolds were sliced into 4 µm sections using a HM 315 microtome (Microm) then stained with hematoxylin and eosin (H&E) dyes. Stained scaffold sections were imaged using an EVOS FL Auto Microscope (Thermo Fisher Scientific).

3.2.9 Statistical analysis

Data are shown as mean ± standard deviation of three or more biological replicates. For the AlamarBlue assay, a two-way ANOVA in GraphPad Prism software was used to determine significance between "PCL-only" and "IO-loaded" groups. P-values were determined from Student's unpaired t-test for the radiofrequency heating studies and WST-1 assays using GraphPad Prism software, with a P-value < 0.05 considered to be statistically significant.

3.3 Results

3.3.1 Facile incorporation of iron oxide into microporous polymer scaffolds

To establish more uniform heating than our previous aluminum disk-PCL scaffold design[85], incorporation of iron oxide particles throughout porous PCL scaffolds was investigated. Microporous PCL scaffolds have previously been fabricated by pressing a PCL and salt mixture into a 5 mm disk using a mechanical press, followed by other post-

processing steps including leaching of the salt to create the porous architecture[77]. To easily incorporate and control the amount of iron oxide loaded into the scaffolds, iron oxide powder was directly weighed out and mixed with the initial salt and PCL polymer mixture (**Fig. 3.2A**). After soaking the fabricated scaffolds in water to leach out the salt, the iron oxide-loaded scaffolds maintained the dark black color of the scaffold prior to leaching, indicating successful loading and retention of iron oxide in the porous scaffolds. Successful loading of iron oxide was also confirmed by the fact that iron oxide-loaded scaffolds exhibited magnetic behavior and were able to adhere to the bottom of a strong neodymium magnet, while PCL-only scaffolds did not (**Fig. 3.3A**). Maintenance of the porous architecture was also a necessary design parameter of iron oxide-loaded scaffolds, as the pores allow for cell infiltration and consequently their destruction by hyperthermia. SEM imaging demonstrated that iron oxide-loaded scaffolds exhibited pores of expected size based on the sieved (250-425 μm) salt used (**Fig. 3.2B&C**). This simple method to incorporate iron oxide particles allowed for fine control of loading amount, which was visually observed by the color gradient of scaffolds loaded with increasing amounts of iron oxide (**Fig. 3.3B**).

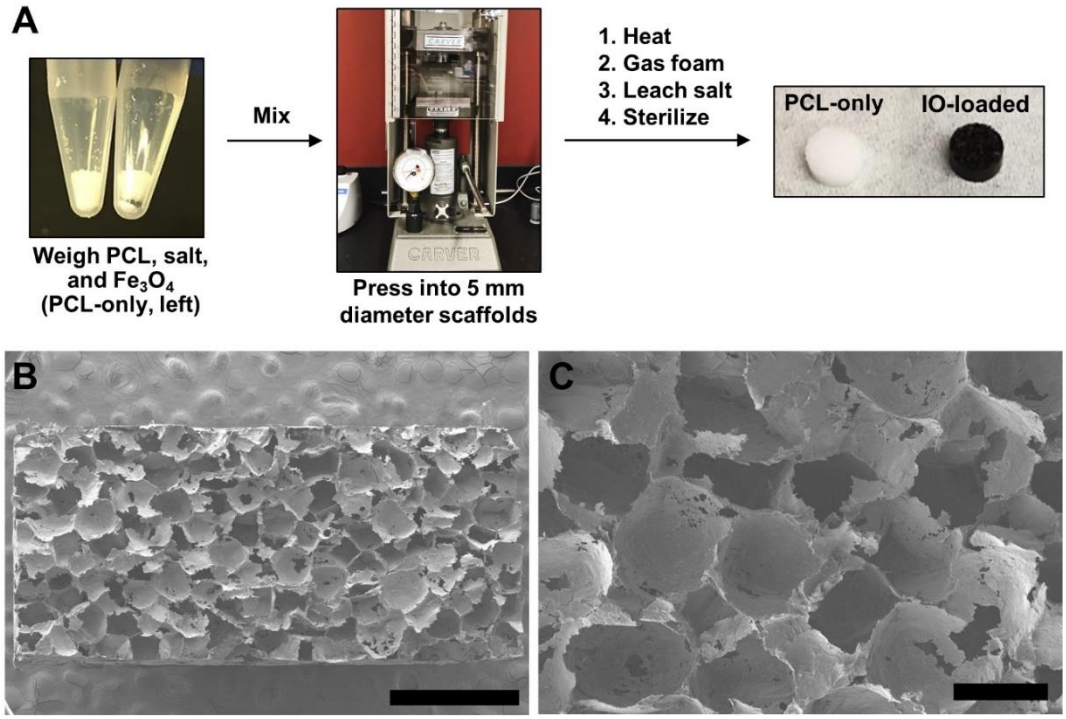

Figure 3.2: Iron oxide particles can easily be incorporated into microporous poly(caprolactone) (PCL) scaffolds. Iron oxide-loaded PCL scaffolds are 5 mm in diameter and have 250 – 425 μm porous architecture. (**A**) Schematic of fabrication process for iron oxide-loaded PCL scaffolds. (**B,C**) Scanning electron microscopy images of cross section of 2 mg iron oxide-loaded PCL scaffold at two magnifications. Scale bars indicate 1 mm and 250 μm for (**B**) and (**C**), respectively.

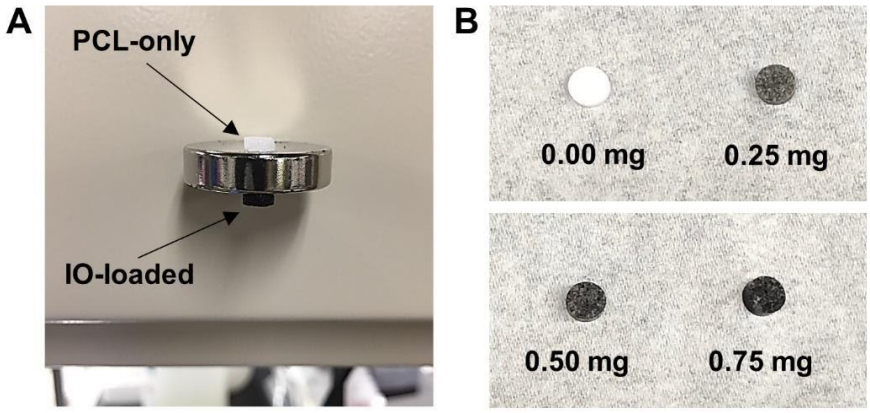

Figure 3.3: Iron oxide-loaded scaffolds exhibit magnetic behavior and can easily be loaded with varying amounts of iron oxide. (A) Image of iron oxide-loaded scaffold adhering to the bottom of a strong neodymium magnet while PCL-only scaffolds do not. **(B)** Image of PCL scaffolds loaded with varying amounts of iron oxide (0.00 – 0.75 mg).

3.3.2 Heating of iron oxide-loaded scaffolds can be modulated with tunable parameters

To confirm iron oxide-loaded scaffolds could heat in the presence of an alternating magnetic field, iron oxide-loaded scaffolds were submerged in 1 mL of deionized water and placed in the center of a copper coil attached to a 1 kW inductive heating system (**Fig. 3.1**). A fiber optic temperature probe was placed through the center of the scaffold, and the system was run for 15 minutes to establish the temperature rise ($T_{final} - T_{initial}$) of the scaffold in the presence of an alternating magnetic field. It was observed that increasing the amount of iron oxide loaded into the PCL scaffold (1.0, 1.5, and 2.0 mg) led to an increase in temperature rise (2.8 ± 0.6, 4.5 ± 1.1, and 7.2 ± 1.0 °C, respectively), which was expected (**Fig. 3.4A**). Additionally, the temperature rise increased (0.5 ± 0.3, 2.2 ± 0.5, and 6.5 ± 0.8 °C) with increasing magnetic field strength (10.0, 20.8, and 30.5 kA/m, respectively) when frequency and iron oxide amount were held constant (**Fig. 3.4B**). These results demonstrate that simple design and system parameters of the iron oxide-loaded scaffolds and the alternating magnetic field can be tuned for a desired temperature rise within the scaffold and consequently heating of infiltrated cells. Because greater iron oxide amounts and increasing magnetic field strength led to greater temperature rise, 2 mg iron oxide-loaded scaffolds in the presence of a 30.5 kA/m and 360 kHz alternating magnetic field were used for the rest of the studies.

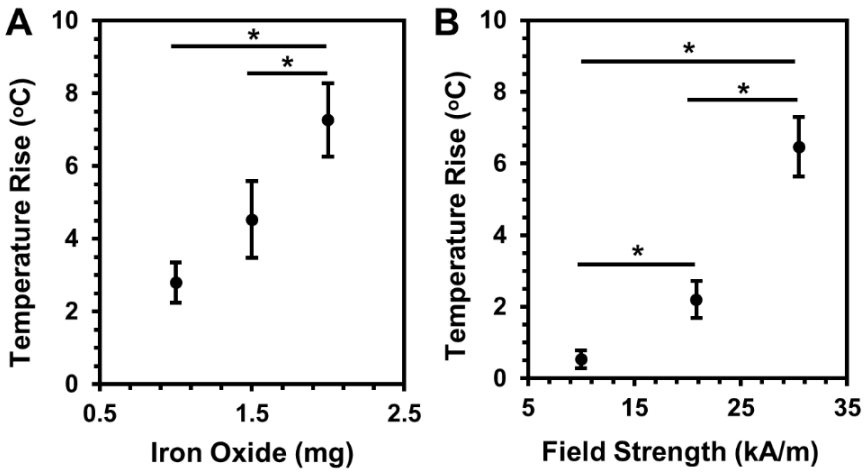

Figure 3.4: Heating of iron oxide-loaded scaffolds can be altered by tunable design and system parameters. (A) Temperature rise of iron oxide-loaded scaffolds with varying amounts of iron oxide under 30.5 kA/m field strength and 360 kHz frequency for 15 minutes. **(B)** Temperature rise of 2 mg iron oxide-loaded scaffolds under 360 kHz frequency for 15 minutes with various magnetic field strengths. *P-value < 0.05.

3.3.3 Ovarian cancer cells can be killed by heat using iron oxide-loaded scaffolds

After verifying the iron oxide-loaded scaffolds could heat in the presence of an alternating magnetic field, ID8 ovarian cancer cells in Matrigel were seeded into scaffolds to determine whether they could be killed by heat *in vitro*. First, to establish that the iron oxide loaded into scaffolds did not adversely affect loaded ovarian cancer cells, an AlamarBlue assay was used to determine whether cell proliferation was inhibited. Seeded ID8 ovarian cancer cells were able to proliferate in both types of scaffolds, and the growth of these cells in PCL-only and iron oxide-loaded scaffolds was not significantly different up to three days after seeding (**Fig. 3.5A**), suggesting the iron oxide incorporated into scaffolds did not cause cytotoxic effects.

Seeded ID8 ovarian cancer cells in PCL-only and iron oxide-loaded scaffolds were then treated with an alternating magnetic field at 30.5 kA/m and 360 kHz for 15 minutes, and a WST-1 assay was used to determine whether seeded cells were effectively killed. Cells

seeded within iron oxide-loaded scaffolds that were left at 37 ºC and 5% CO_2 conditions ("IO no heat", negative control for cell death) had the greatest cell viability, while cells seeded within iron oxide-loaded scaffolds treated with the alternating magnetic field ("IO heat") exhibited cell viability values similar to media only controls (positive control for cell death) (**Fig. 3.5B**). Ovarian cancer cells seeded within PCL-only scaffolds which were treated with the same field conditions ("PCL heat") also exhibited some decrease in cell viability, although not as significant as the treated iron oxide-loaded scaffold group. This decrease in cell viability in PCL-only scaffolds is attributed to the imperfect insulation between the coil system and the vial containing the scaffold, resulting in some conductive heat transfer from the coil to the cells within the scaffold (**Fig. 3.6**). Overall, we were able to demonstrate that iron oxide-loaded scaffolds can be used to kill ovarian cancer cells seeded within the scaffold by hyperthermia.

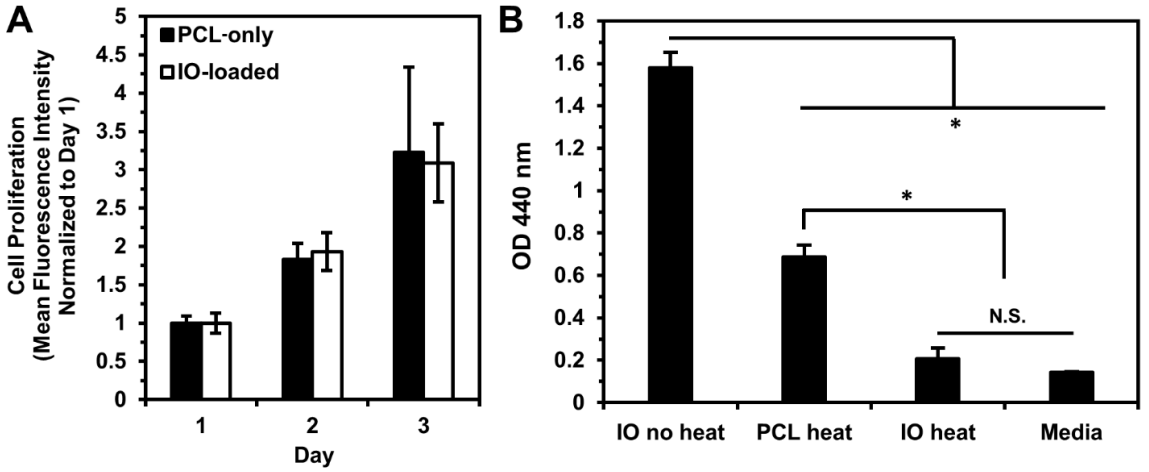

Figure 3.5: Iron oxide-loaded scaffolds are not cytotoxic and can kill ovarian cancer cells by hyperthermia *in vitro*. (A) Proliferation of ID8 ovarian cancer cells in PCL-only or iron oxide-loaded scaffolds for up to 3 days after seeding using an AlamarBlue assay. Bars indicate mean fold change and standard deviation normalized to Day 1. A two-way ANOVA determined there was no statistically significant difference between "PCL-only" and "IO-loaded" groups. **(B)** Viability of ID8 ovarian cancer cells seeded onto iron oxide-loaded scaffolds that were left in 37ºC and 5% CO_2 conditions ("IO no heat"), PCL-only scaffolds that were heated under an alternating magnetic field ("PCL heat"), and iron oxide-loaded scaffolds that were heated under an alternating magnetic field

("IO heat") using a WST-1 assay. No cell control of media only ("Media") was used as a positive control for cell death. Decreases in 440 nm absorbance indicate decreases in cell viability. All treatments under an alternating magnetic field were for 15 minutes at 30.5 kA/m and 360 kHz fields. *P-value < 0.05 relative to "IO no heat" or "PCL heat".

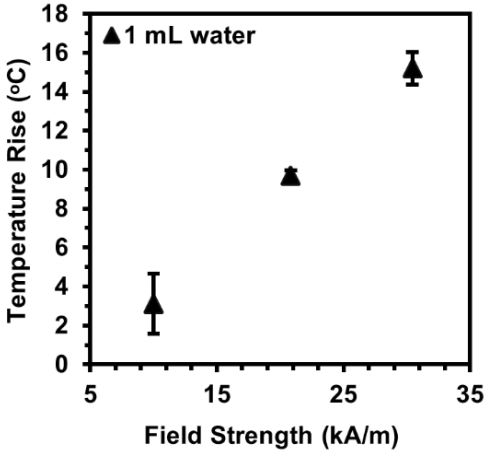

Figure 3.6: Example of background heating of copper coil during treatment. Control tests with 1 mL of deionized water only in a cryovial were completed, and the temperature rise after 15 minutes at 360 kHz and various field strengths was determined using a fiber optic temperature probe. All temperature rise studies investigating iron oxide loading amount and field strength had water only control tests, and the background heating was subtracted off to give final values.

3.3.4 Iron oxide-loaded scaffolds become infiltrated with cells after intraperitoneal implantation

PCL-only and iron oxide-loaded scaffolds were next implanted into the intraperitoneal cavity of female C57BL/6J mice to compare the infiltration of cells into the porous architecture and verify that iron oxide-loaded scaffolds can become properly infiltrated when implanted in this location. Initially, scaffolds were harvested after 3-4 weeks of implantation for histological analysis, as this timepoint has previously been shown to provide sufficient cell infiltration for PCL-only scaffolds[77,85,168]. As expected, the PCL-only scaffolds exhibited significant cell infiltration, as seen by the many nuclei visualized by hematoxylin and eosin (H&E) staining of PCL-only scaffold sections (**Fig. 3.7A**). However, it was evident from staining that iron oxide-loaded scaffolds demonstrated

decreased cell infiltration at 3-4 weeks post-implantation (**Fig. 3.7B**), suggesting a longer implantation period is needed for sufficient cell infiltration prior to treatment. After 6-7 weeks of implantation, iron oxide-loaded scaffolds harvested for histology demonstrated enhanced cell infiltration and exhibited similar infiltration as the PCL-only scaffolds (**Fig. 3.7C**). To verify that a sufficient amount of iron oxide would still be present within iron oxide-loaded scaffolds at this timepoint, an *in vitro* study of iron release from the scaffolds was performed. Negligible amounts of total iron released were observed after 6 weeks of scaffold incubation and subsequent heating *in vitro* (**Fig. 3.8**), indicating that there would be sufficient iron oxide present for non-invasive hyperthermic treatment after 6-7 weeks of implantation.

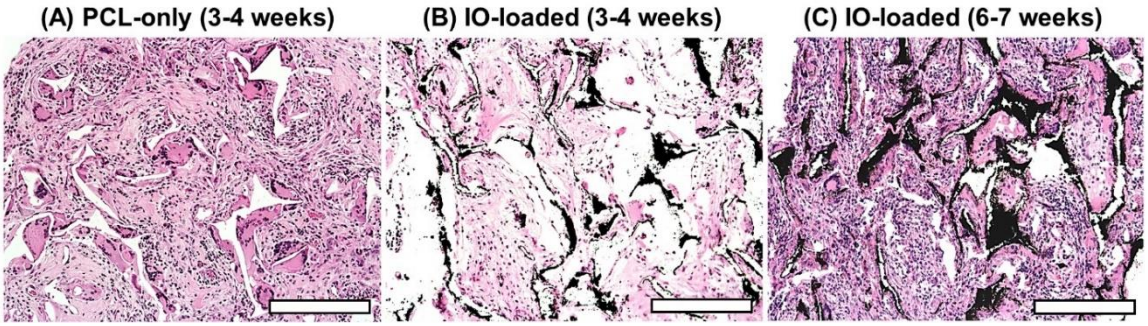

Figure 3.7: Iron oxide-loaded scaffolds can become fully infiltrated with cells when implanted *in vivo*, although requiring a longer implantation time than PCL-only scaffolds. Scaffolds were implanted by the intraperitoneal wall for 3-4 or 6-7 weeks in female C57BL/6J mice. **(A-C)** H&E staining of sections of a PCL-only scaffold **(A)**, IO-loaded scaffold implanted for 3-4 weeks **(B)**, or IO-loaded scaffold implanted for 6-7 weeks **(C)**. Black areas seen in "IO-loaded" histological images but not in "PCL-only" are the iron oxide. Scale bar indicates 200 μm.

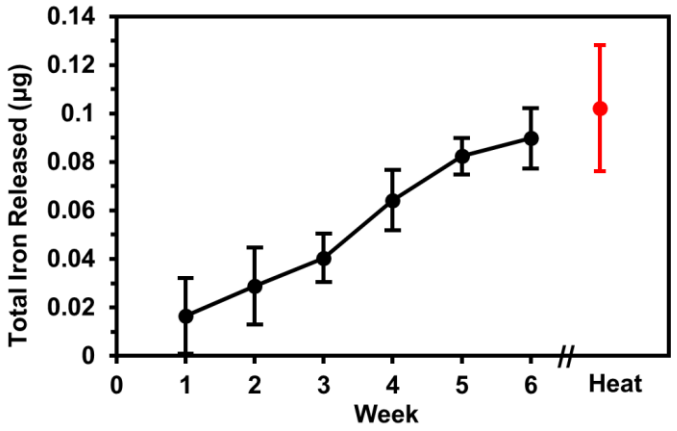

Figure 3.8: Iron oxide-loaded scaffolds exhibit negligible release of iron over a 6-week duration and after heating *in vitro*. The total amount of iron released was determined using a Ferrozine assay. Release was measured weekly for 6 weeks from 2 mg iron oxide-loaded scaffolds, which were placed in PBS and kept at 37 °C. At week 6, scaffolds were then treated with an alternating magnetic field for 15 minutes at 30.5 kA/m and 360 kHz. The additional amount of iron released after this treatment contributing to total iron released per scaffold is shown as "Heat" (red).

3.3.5 Cells in tissue-laden iron oxide-loaded scaffolds can be killed by hyperthermia ex vivo

To demonstrate that tissue-laden scaffolds could be successfully heated, iron oxide-loaded scaffolds were implanted in the intraperitoneal cavity of mice for 6-7 weeks, then harvested and placed in the center of the coil system for treatment in the presence of a 30.5 kA/m and 360 kHz alternating magnetic field for 15 minutes. Tissue-laden iron oxide-loaded scaffolds which were treated ("IO heat") exhibited cell viability similar to media only controls ("Media", positive control for cell death) after hyperthermic treatment (**Fig. 3.9**). As expected, cells infiltrated within tissue-laden iron oxide-loaded scaffolds left at standard culture conditions ("IO no heat", negative control for cell death) exhibited significantly higher viability. These *ex vivo* results are consistent with the *in vitro* studies using ID8 ovarian cancer cells, and they further demonstrate that endogenous proteins and matrix deposited by infiltrated cells within implanted iron oxide-loaded scaffolds do not hinder

the ability of iron oxide-loaded scaffolds to effectively kill infiltrated cells under an alternating magnetic field.

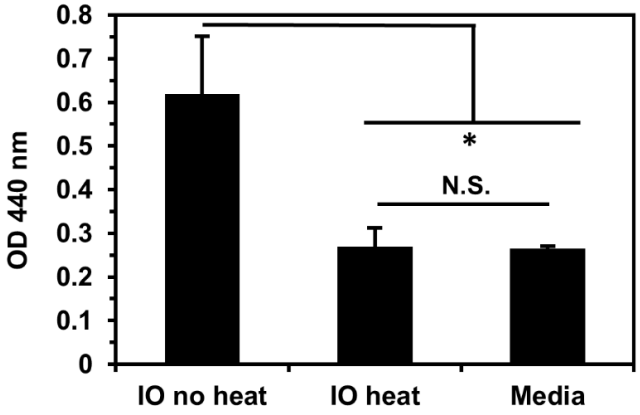

Figure 3.9: Cells within tissue-laden iron oxide-loaded scaffolds can be killed by heat *ex vivo* in the presence of an alternating magnetic field. Using a WST-1 assay, the viability of cells in tissue-laden scaffolds placed under standard culture conditions (37°C and 5% CO_2, "IO no heat") or after treatment for 15 minutes at 30.5 kA/m and 360 kHz ("IO heat") was investigated. Media only controls were used as a no cell control ("Media"). *P-value < 0.05 relative to "IO no heat".

3.3.6 Infiltrated cells in iron oxide-loaded scaffolds can be killed non-invasively by hyperthermia in vivo

Lastly, we sought to establish whether iron oxide-loaded scaffolds could be used to non-invasively kill infiltrated cells by heat in the intraperitoneal cavity *in vivo*. Mice with iron oxide-loaded scaffolds implanted intraperitoneally for 6-7 weeks were used to ensure there was proper cell infiltration prior to treatment. Due to the size constraints of the coil, mice were carefully placed on their backs with the abdominal cavity placed beneath the coil (**Fig. 3.10A**) and were treated with 26.4 ± 0.5 kA/m magnetic field strength (**Fig. 3.11**) and 360 kHz frequency for 15 minutes. Treated scaffolds were harvested three days post-treatment for histological analysis. Upon H&E staining, it was observed that the number of nuclei present in mice with proper placement of treated iron oxide-loaded scaffolds significantly decreased, with primarily protein/matrix left behind (**Fig. 3.10B&C**) as

compared to 6-7 week-implanted iron oxide-loaded scaffolds that did not receive treatment (**Fig. 3.7C**). Importantly, some treated iron oxide-loaded scaffolds exhibited regions of effective heating (**Fig. 3.10C**), while other regions of the same treated scaffold had significantly more nuclei present (**Fig. 3.10D**). Because the field strength decreases significantly once outside the center of the coil (both axially and radially)[169], these findings indicate sub-optimal placement of the iron oxide-loaded scaffold during treatment and demonstrate the importance of the scaffold's position within the magnetic field for effective cell death. Overall, it was demonstrated that iron oxide-loaded scaffolds in the intraperitoneal cavity can be used for hyperthermic treatment of infiltrated cells both non-invasively and in a relatively short treatment time *in vivo*.

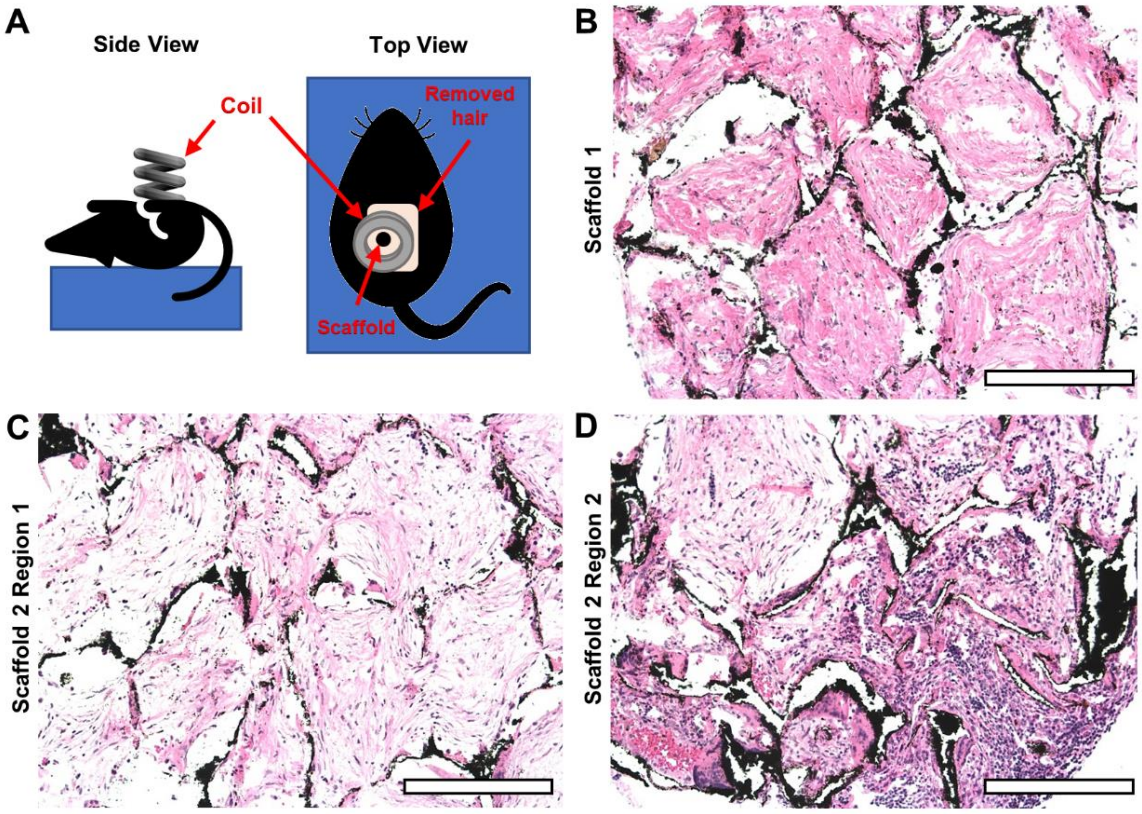

Figure 3.10: Cells within iron oxide-loaded scaffolds can be non-invasively killed *in vivo* in the presence of an alternating magnetic field. Iron oxide-loaded scaffolds were implanted into the intraperitoneal cavity of C57BL/6J mice for 6-7 weeks and then treated for 15 minutes at 26.4 ± 0.5 kA/m field strength and 360 kHz field frequency. Scaffolds were retrieved 3 days post-

treatment. **(A)** Schematic of mouse and scaffold positioning relative to the coil system for hyperthermic treatment. The hair on the belly of mice was removed to approximate the location of the implanted iron oxide-loaded scaffold in order to position it as close to the bottom of coil as possible for treatment. **(B-D)** Examples of H&E stained sections of iron oxide-loaded scaffolds with successful treatment **(B,C)** and a region with partial treatment **(D)**. Panels (**C**) and (**D**) are images of different regions from the same treated scaffold. Scale bar indicates 200 μm.

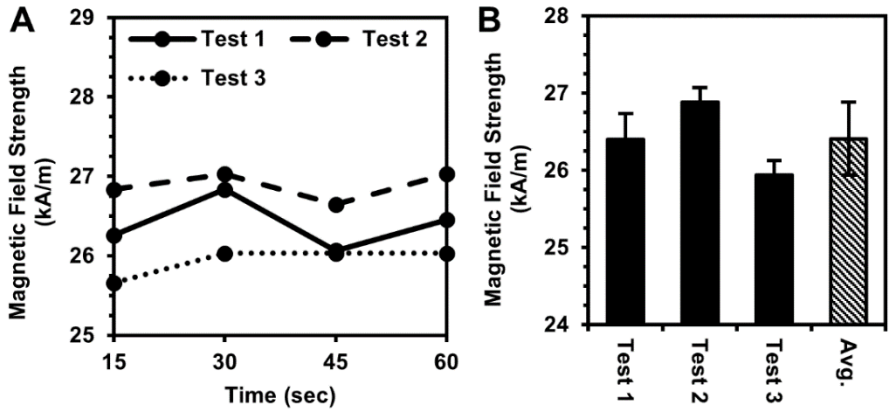

Figure 3.11: Magnetic field strength beneath coil for *in vivo* heating of iron oxide-loaded scaffolds was determined. The magnetic field strength in the radial center and ≈ 1-2 mm below the bottom of the coil was determined using a magnetic field probe. **(A)** Values of magnetic field strength at 15-second intervals during three tests (60-second duration total). **(B)** Average magnetic field strength for each 60-second test (black bars) and overall average magnetic field strength for all tests combined (striped bar, 26.4 ± 0.5 kA/m).

3.4 Discussion

Biomaterial implants which localize disseminated cancer cells are promising for ovarian cancer treatment, as this disease is often found in an advanced stage and thus in a highly disseminated form throughout the intraperitoneal cavity. Further, a biomaterial which can also locally, non-invasively, and repeatedly destroy cells by heat in the intraperitoneal cavity is of great interest due to the recurrent nature of ovarian cancer. Here, we incorporated iron oxide particles into porous PCL scaffolds previously shown to recruit cancer cells by mixing iron oxide particles with PCL microspheres and salt prior to mechanical pressing[77,85]. In our previous work, an aluminum disk was embedded in the center of these PCL scaffolds for hyperthermic treatment of infiltrated cells under an

alternating magnetic field[85]. However, using a single thermal seed within the scaffold will provide less uniform heating versus a scaffold design containing a heat source that is distributed throughout, such as iron oxide particles. Uniform scaffold heating allows for a lower maximum temperature needed within the scaffold for effective hyperthermia treatment of the entire scaffold, and a distributed heat source decreases the dependence of scaffold orientation (and its single thermal seed) with respect to the magnetic field on heating. In these studies, after leaching of salt and sterilization, iron oxide-loaded scaffolds were homogeneous in texture and color, indicating appropriate dispersion of iron oxide throughout and consequently suggesting more uniform heating for cell death than the previous design.

Extensive work has been completed to characterize the heating of iron oxide particles upon placement within alternating magnetic fields[154,170,171]. Iron oxide particles are known to generate heat through eddy current and hysteresis losses when > 1 μm in size, superparamagnetic mechanisms such as Neel or Brownian relaxation losses when < ≈ 20 nm, and hysteresis heating for those sized in between[154]. The iron oxide particles used here were spherical and sieved giving a < 44 μm size, and the use of iron oxide particle powder allowed for simple incorporation of iron oxide into the scaffold fabrication process along with easy modulation of loading amounts. Because each iron oxide particle acts as a thermal seed in the presence of an alternating magnetic field, larger concentrations of iron oxide lead to faster heating rates[171], which was observed in the temperature rise studies here. The size and shape of iron oxide particles can also influence heating[170–174], and testing various sizes or morphologies of iron oxide particles within porous PCL scaffolds could lead to scaffold designs with enhanced heating in future studies. Specifically, investigating

methods to incorporate and retain iron oxide nanoparticles into PCL scaffolds is of interest for optimized heating and/or reducing the iron oxide content in the scaffolds. It is also well understood that magnetic field parameters will influence the heating of iron oxide particles. Shah *et al*. observed greater temperature rise with increasing magnetic field strengths and frequencies for dextran-coated iron oxide particles[171]. Guardia *et al*. observed a similar trend where increasing field strength and frequency resulted in larger specific absorption rates (SAR) for iron oxide nanocubes[172], with SAR values indicating the rate at which a material absorbs energy per unit mass. The temperature rise of iron oxide-loaded scaffolds containing iron oxide powder with size < 44 μm also increased with greater magnetic field strengths in this study. Previous work indicates that quadratic dependence of field strength may be possible, while a linear dependence of frequency on SAR values is expected for various magnetic nanoparticles[172,175], suggesting further optimization of heating could be attained by testing iron oxide nanoparticles in PCL scaffolds under various magnetic field parameters. While the magnetic field strength has the dominant effect on heating, the field frequency is another parameter that could be optimized in the future if a greater temperature rise is desired for the iron oxide-loaded scaffolds.

In vitro and *in vivo* studies have shown effective direct cell killing at temperatures between 41 and 47 °C[148,176,177]. Additionally, it has been demonstrated that cell survival exponentially decreases with treatment time once temperatures reach and increase beyond 43 °C[177,178]. From the temperature rise studies, the greatest temperature rise observed was ≈ 7 °C, thus indicating potential temperatures of up to 43 °C *in vivo*. This temperature is suitable for the iron oxide-loaded PCL scaffolds due to the melting point of PCL (~10 to 15 °C above physiological temperature)[78], as significantly higher temperatures may cause

enhanced release of iron oxide and limit its potential for multiple hyperthermic treatments. Upon *in vitro* treatment of ID8 ovarian cancer cells within iron oxide-loaded scaffolds, cell viability decreased to that of media only controls. Consistent with the results reported here, 3-D printed mesoporous bioactive glass/PCL scaffolds with iron oxide demonstrated significant temperature rise in the presence of an alternating magnetic field; however the cell killing capability of those scaffolds was not investigated[162]. In addition, Zhang *et al*. fabricated folic acid-functionalized gelatin scaffolds with iron oxide, which killed HeLa cervical cancer cells upon NIR laser irradiation *in vitro*[179].

For its potential application towards ovarian cancer, iron oxide-loaded scaffolds were implanted by the intraperitoneal wall to investigate cell infiltration into the porous architecture. This site for implantation is of interest because ovarian cancer metastases are typically confined within the intraperitoneal cavity, and ovarian cancer cells disseminated from the primary tumor will adhere to the peritoneum which lines the cavity wall and abdominal organs[22]. Previously, PCL-only scaffolds had been implanted into the subcutaneous space or wrapped in the gonadal fat pad within the intraperitoneal cavity, and 3-4 weeks of implantation was sufficient for cell infiltration[77,85,168]. Here, PCL-only scaffolds exhibited many nuclei and deposited extracellular matrix within pores after 3-4 weeks when attached to the intraperitoneal wall, but iron oxide-loaded scaffolds required 6-7 weeks of implantation for similar levels of cell infiltration at this site. This decreased rate of infiltration is likely due to the low solubility of iron oxide in water, thus making the iron oxide-loaded scaffolds more hydrophobic, which will impact cell adhesion and consequently the rate of infiltration[180]. For *in vivo* applications, the advantage of a biomaterial implant containing iron oxide versus injection of free particles is that the iron

oxide can be directly placed within the intraperitoneal cavity in a high and localized concentration that is stable over a longer period of time. Iron oxide-loaded scaffolds could address the current challenges of traditional systemic delivery, such as fast clearance from the body and organ cytotoxicity due to the larger doses required to achieve sufficient concentrations at the targeted site[78]. Incorporation of iron oxide into PCL scaffolds did not significantly alter ID8 ovarian cancer cell proliferation, suggesting no significant cytotoxicity. This is consistent with previous reports with non-cancerous cell lines and cancer cell lines arising from glia, breast, liver, and cervix demonstrating *in vitro* biocompatibility towards iron oxide particles when using concentrations ranging from 0.1 to 50 μg/mL and toxicity occurring at a higher concentration of 100 μg/mL[181,182]. Further, iron oxide remained concentrated within the scaffold for up to 6 weeks and even after heating *in vitro*, and iron oxide particles should primarily be released only as the PCL polymer degrades, occurring through hydrolysis over the duration of months to years *in vivo*[183,184]. Additionally, the use of PCL polymer in this scaffold design and its slow degradation rate should allow for repeated use of non-invasive hyperthermic treatment due to the high retention of concentrated iron oxide within the scaffold.

After implantation for 6-7 weeks in the intraperitoneal cavity, it was demonstrated that tissue-laden iron oxide-loaded scaffolds could be used to kill infiltrated cells *ex vivo* in the presence of an alternating magnetic field. These *ex vivo* results are distinct from the *in vitro* results where iron oxide-loaded scaffolds heated ovarian cancer cells in Matrigel, as the extracellular matrix density and proteins deposited by infiltrated cells within the scaffold pores will likely differ. Most importantly, this *ex vivo* study demonstrated that infiltrated cells could be killed within iron oxide-loaded scaffolds when placed in the center of the

coil, where the field is most uniform. In contrast, iron oxide-loaded scaffolds were investigated for hyperthermia potential *in vivo* but had to be placed underneath the coil during treatment due to size constraints of the coil. Once outside of the inductive coil, the magnetic field strength can vary during treatment, and it will decrease significantly at positions away from the center of the coil[85,169]. When the scaffold was placed within the alternating magnetic field, killing of infiltrated cells could be accomplished, as evidenced by the decrease in number of nuclei through H&E staining. The observation that some regions within a scaffold were treated successfully while others had many remaining cells displays the importance of properly positioning the iron oxide-loaded scaffold within the magnetic field. To mitigate this, a larger coil in which the entire mouse could be placed in a uniform field volume during treatment would be useful for future studies, and this setup would be more representative of what is currently used in the clinic (e.g. MRI scanners). However, even though the iron oxide-loaded scaffolds had to be positioned outside of the coil for treatment, decreases in cell number were still observed. The scaffold design and magnetic field parameters should be further optimized for continued clinical translation, as the field strength and frequency (H×f) used for patients should be $< 5\times10^9$ A/(m·s)[185,186]. Potential options involve designing larger scaffolds allowing for increased iron oxide loading and thus achieving higher temperatures, or treatment duration could also be increased as these studies used treatment times of only 15 minutes. Clinical trials using hyperthermia in combination with other forms of treatment have consisted of hyperthermia treatment times of ≥ 30 minutes at a desired maximum temperature and often last an hour or more in total[187].

In conclusion, iron oxide was incorporated into porous PCL scaffolds previously shown to recruit disseminated cancer cells by simple mixing of iron oxide particles with PCL microspheres and salt at the beginning of fabrication. These iron oxide-loaded scaffolds exhibited magnetic behavior and maintained their porous architecture, which is necessary for cell infiltration. Further, scaffold design and magnetic field parameters – such as iron oxide loading and field strength, respectively – that can easily be modulated were shown to influence temperature rise. Incorporation of iron oxide did not exhibit cytotoxicity against ovarian cancer cells but did allow for their destruction under an alternating magnetic field *in vitro*. Iron oxide-loaded scaffolds were implanted by the intraperitoneal cavity wall of female mice and exhibited extensive cell infiltration and extracellular matrix deposition in the porous architecture after 6-7 weeks. The infiltrated cells within iron oxide-loaded scaffolds could be killed both *ex vivo* and *in vivo* under an alternating magnetic field, demonstrating the therapeutic potential of iron oxide-loaded scaffolds to kill cells locally and non-invasively. The incorporation of iron oxide into biomaterials that can capture tumor cells enables application of hyperthermia to cancers that are disseminated, addressing the challenges of systemic delivery by facilitating a sufficiently high and localized concentration of the iron oxide particles to achieve therapeutic heating levels.

Chapter 4: Characterizing recruitment potential of biomaterial scaffolds for cancer cell capture in an advanced stage ovarian cancer mouse model

4.1 Introduction

After establishing that iron oxide-loaded scaffolds can be used to non-invasively kill infiltrated cells under an alternating magnetic field (AMF) *in vivo*, additional questions need to be answered to determine if this approach could be therapeutically applied to ovarian cancer. In this chapter, studies were conducted to investigate whether our previously developed PCL-only and iron oxide-loaded scaffolds could capture disseminated ovarian cancer cells *in vivo* in an advanced stage ovarian cancer mouse model. We also sought to identify when cancer cells would be evident at the scaffolds during disease progression and where the cancer cells would be located (i.e. within scaffold pores or on the outside). By better understanding these conditions, future therapeutic studies can be designed so that the therapeutic benefit of iron oxide-loaded scaffolds under AMF can be maximized, and non-invasive hyperthermic treatment of disseminated ovarian cancer cells can be investigated as a novel alternative treatment modality for advanced stage ovarian cancer.

As indicated above, any new technology or treatment must first be investigated in *in vivo* models before it can be translated to the clinic. Ovarian cancer mouse models consist of patient derived-xenograft (PDX) models, models established using *in vitro* human tumor cell lines, and syngeneic models. In ovarian cancer, PDX models are established from patient primary tumor tissue or tumor cells from ascites. PDX models allow for patient-

specific study of a tumor's response to various treatments, but this type of model requires a lot of time to graft the patient material into mice and to expand the colonies of mice which have successfully established tumors. Additionally, because human material is being grafted into mice, immunodeficient mice (which are genetically modified to lack certain immune cell populations) are required for use. In ovarian cancer, three commonly used immunodeficient mouse strains are nude mice (T cell deficient), severe combined immunodeficient (SCID) mice (T cell and B cell deficient), and NOD SCID gamma (NSG) mice (B cell, T cell, and NK cell deficient, hemolytic complement deficient, and have defective macrophages and dendritic cells)[188,189]. Similarly, ovarian cancer mouse models established from *in vitro* human tumor cell lines, like SKOV-3 and IGROV-1, also require immunodeficient mice. Because immunodeficient mice lack immune system components, "humanized mouse models" - where not only human tumor cells are injected but also human hematopoietic stem cells for later differentiation *in vivo* - have been developed[188,190]. Although this type of model allows for immunotherapy studies, some cell lineages are never developed (i.e. erythrocytes, neutrophils[190]) or only differentiate to an immature state (i.e. T and B cells[191]).

Contrastingly, syngeneic mouse models are established from allografts of mouse tumor cell lines into mice of the same genetic strain, and consequently, these mouse models have fully intact immune systems. The ID8 murine ovarian cancer cell line is the most widely used cell line for syngeneic ovarian cancer mouse models. The ID8 cell line was developed through serial passaging of C57/BL6 mouse ovarian surface epithelial cells[167], and they exhibited an altered morphology and loss of contact-inhibited growth. Further, the tumorigenicity of these cells was verified after their subcutaneous and intraperitoneal (i.p.)

injection into C57/BL6 mice resulted in tumor formation. Since its creation, the ID8 mouse model has been extensively used in therapeutic studies investigating drug treatments and immunotherapy applications due to the model having a fully intact immune system. Because our ultimate goal is to determine whether iron oxide-loaded scaffolds can kill ovarian cancer cells under AMF and potentially elicit an antitumor immune response, use of the syngeneic ID8 ovarian cancer mouse model in these studies is desired.

As mentioned previously, polymer scaffolds have been shown to localize disseminated ovarian cancer cells *in vivo* in a mouse model[75]. However, these findings were demonstrated in a model using the human SKOV-3 ovarian cancer cell line and immunodeficient SCID Beige mice, and even the authors acknowledged that a "limitation is that these preclinical studies have been conducted in immuno[deficient] mice." Although a therapeutic benefit was observed when these scaffolds were implanted and then later removed after disease localization, the design of our iron oxide-loaded scaffolds improves upon this by allowing for repeated non-invasive heating and killing of cancer cells under AMF and would not require surgical removal to lower the disease burden. Iron oxide/gelatin composite scaffolds functionalized with folic acid for enhanced cancer cell recognition have previously been used to heat and kill HeLa cervical cancer cells *in vitro*[179], but their ability to successfully capture cancer cells in an *in vivo* model was never examined. Lastly, our group has demonstrated the utility of microporous PCL scaffolds to recruit and kill metastatic cancer cells in a breast cancer mouse model[76,77,85], but the therapeutic potential of our scaffolds has yet to be explored in an ovarian cancer mouse model.

In this chapter, we investigated whether our PCL-only and iron oxide-loaded scaffolds can capture disseminated ovarian cancer cells *in vivo*. Disseminated ovarian cancer cells were successfully captured using both types of scaffolds in an advanced stage ID8 ovarian cancer mouse model. The ID8 mouse model exhibited hallmarks of advanced patient disease, including ascites formation and peritoneal metastases. Because the ID8 cell line was not labeled with a fluorescent or bioluminescent marker, a method to quantify the disease state through necropsy evaluation was developed for tracking disease progression and comparing experimental groups in future studies. PCL-only scaffolds captured ID8 cells regardless of whether they were implanted before or during disease formation. Lastly, iron oxide-loaded scaffolds captured ID8 cells before extensive disease formation, allowing for potential hyperthermic treatment prior to significant disease burden in future therapeutic studies.

4.2 Materials and Methods

4.2.1 ID8 ovarian cancer mouse model

All animal studies were approved and conducted following the guidelines under the University of Minnesota's Institutional Animal Care and Use Committee. As mentioned in Chapter 3.2.4, mouse ID8 ovarian cancer cells were kindly gifted from Dr. Katherine Roby and were cultured as previously described. To establish an advanced stage ovarian cancer mouse model, 10 million ID8 cells in 400 μL phosphate buffered saline (PBS) were injected i.p. with a 25.5 gauge needle (0.0143 inch nominal inner diameter to minimize cell shearing) into female C57/BL6J mice (Jackson Laboratory). The weight and abdomen size (length and width) of each mouse were measured immediately prior to ID8 cell injection

and measured periodically throughout disease progression using a scale and digital calipers, respectively. For studies monitoring disease progression to end-stage disease, a disease end-point metric of a 30 gram (g) weight and visual abdominal swelling was used, and mice were humanely euthanized at this point of significant disease burden.

4.2.2 Scaffold fabrication and implantation

PCL-only and iron oxide-loaded scaffolds were fabricated as previously described in Chapter 3.2.1. For these studies, PCL-only scaffolds were created from 3 mg PCL microspheres and 90 mg sieved salt (250 - 425 μm), while iron oxide-loaded scaffolds were created from 3 mg PCL microspheres, 90 mg sieved salt (250 - 425 μm), and 2 mg of iron oxide bulk powder (spherical, < 44 μm Fe_3O_4 particles, Lansco 8330M). Surgical implantation of scaffolds into the i.p. cavity was also completed in the same manner as previously described in Chapter 3.2.7. In studies investigating capture of ID8 cells by PCL-only scaffolds, one PCL-only scaffold was implanted per mouse and placed on the left side of the midline incision next to the i.p. wall. The final study investigating capture of ID8 cells by iron oxide-loaded scaffolds involved implantation of two iron oxide-loaded scaffolds in the i.p. cavity of each mouse, with a scaffold on each side of the midline incision next to the i.p. wall.

4.2.3 Necropsy evaluation

Weight and abdominal measurements were taken prior to necropsy evaluation as described above. Glucose levels were measured by sampling blood from the tail vein using a glucometer (Contour Next EZ, Bayer). At study end-points, all ascites fluid was carefully removed from the intact abdominal cavity using a needle and syringe, and the total volume removed was recorded. After removal of ascites fluid, the abdominal cavity was opened,

and digital calipers were used to measure metastatic nodules on the i.p. wall. Visual disease scoring was done consistently by the same individual, and scores for individual organs/tissues and an overall score were given following the criteria shown below in **Table 4.1** and **Table 4.2**, respectively.

Table 4.1: Criteria adapted from Roby *et al*. used for visual disease scoring of individual organs and tissues during necropsy evaluation[167].

Score	Criteria
0	No metastases evident by visual examination
1	Metastases visually evident in an isolated area of tissue/organ
2	Moderate formation of metastases in multiple areas of tissue/organ
3	Extensive metastases on majority of tissue/organ

Table 4.2: Criteria adapted from Roby *et al.* used to assign an overall disease score for each mouse[167].

Score	Criteria
0	No metastases evident by visual examination
1	One tissue/organ with metastases
2	Moderate metastases on more than one tissue/organ
3	Extensive metastases on multiple tissues/organs

4.2.4 Histological analysis

Processing, slicing, and hematoxylin and eosin (H&E) staining were completed for harvested scaffolds as described previously in Chapter 3.2.8. Briefly, harvested scaffolds were immediately placed in 10% buffered formalin solution (Millipore Sigma) then later transferred to 70% ethanol prior to being embedded in paraffin blocks. 4 µm sections were obtained using a HM 315 microtome (Microm) then stained with H&E dyes. Stained scaffold sections were imaged using an EVOS FL Auto Microscope (Thermo Fisher Scientific).

4.3 Results

4.3.1 ID8 ovarian cancer mouse model exhibits hallmarks of advanced patient disease

To investigate whether iron oxide-loaded scaffolds under AMF can be used as a novel treatment modality for ovarian cancer, an advanced stage ovarian cancer mouse model representative of patient disease is needed. In initial studies, ID8 cell number and needle size used for i.p. injection of cells into female mice were optimized, and 10 million ID8 cells resulted in significant disease formation. Control mice which received no ID8 cells maintained a normal body type throughout the study (**Fig. 4.1A**), while mice which received ID8 cells eventually exhibited visual abdominal swelling (**Fig. 4.1B**) due to significant production and accumulation of ascites fluid (**Fig. 4.1C**), which is consistent with what is observed in patients in the clinic. Further, metastases were evident throughout the peritoneal cavity of the mice, and metastatic nodules could be clearly seen on the i.p. lining or as clusters on abdominal organs and tissues (**Fig. 4.1D&E**). A disease end-point metric of 30 g weight and visual abdominal swelling for significant disease burden was established during these studies, which occurred around 14 to 16 weeks after ID8 cell injection.

Figure 4.1: ID8 ovarian cancer mouse model exhibits hallmarks of advanced patient disease. **(A)** Example of control mouse with no ID8 cell injection. **(B,C)** Images of ID8 mouse with advanced disease as seen by clear abdominal swelling **(B)** due to significant accumulation of ascites fluid **(C)**. **(D,E)** Macrometastases are visible on organs and tissues in the abdominal cavity (dashed circles) and are also present as metastatic nodules on the i.p. wall (arrow, **E**).

Using histology, the i.p. lining of control mice and ID8-injected mice was also compared. H&E staining of sections of i.p. lining showed a smooth surface with a thin layer of cells in control mice (**Fig. 4.2A**). In ID8-injected mice, micrometastases presenting as large clusters of cells attached to the i.p. lining were observed by histology (**Fig. 4.2B**), in addition to the larger macrometastatic nodules visible by eye. Metastatic nodules exhibited densely packed nuclei along with evidence of blood vessel formation (**Fig. 4.2C**). Overall, the i.p. injection of the ID8 cell line was verified to establish an advanced stage ovarian cancer mouse model that exhibits hallmarks of advanced patient disease, such as ascites accumulation and metastases throughout the peritoneal cavity.

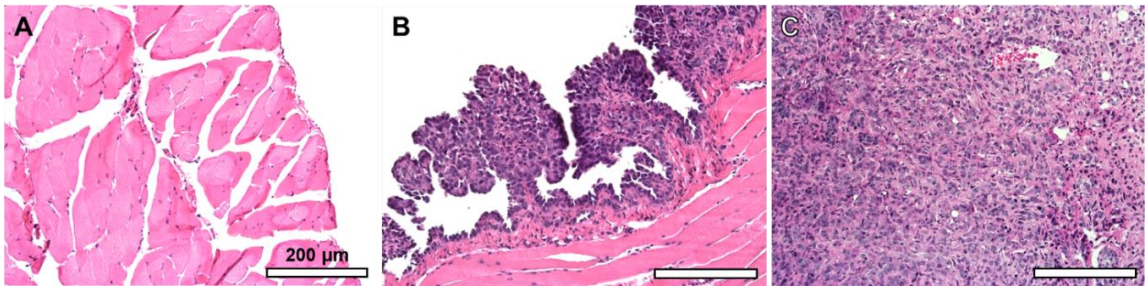

Figure 4.2: Histology of tissues from naïve and ID8 mice. Images of H&E staining of i.p. lining from a control mouse (no ID8 cells injected, **A**), i.p. lining from an ID8 mouse (**B**), and ID8 metastatic nodule (**C**). Scale bar indicates 200 µm.

4.3.2 PCL-only scaffolds implanted during disease progression capture disseminated ID8 cells

The next study evaluated whether PCL-only scaffolds could capture disseminated ID8 cells *in vivo*. Ten million ID8 cells were injected i.p. into female mice, and PCL-only scaffolds were implanted into mice next to the i.p. wall 9 weeks into disease progression and later harvested for histology (**Fig. 4.3A**). This experimental scheme where scaffolds are implanted after ID8 cell injection would be representative of a clinical situation where patients have remaining disease after initial treatment or exhibit recurrence, and a scaffold is implanted to capture disseminated cells. A group of ID8 mice which did not receive scaffolds ("ID8") was used to compare disease progression, and a group of naïve mice (no ID8 cell injection) that received PCL-only scaffolds was used as a control ("PCL-only"). After ID8 cell injection, the weight and abdomen size of the mice were monitored over time (**Fig. 4.3B&C**). Mice receiving ID8 cells exhibited a sharp increase in these two parameters around 90 days post-ID8 injection due to onset of ascites accumulation, while control mice with scaffolds only maintained a steady increase in weight and abdomen size. When ID8 mice reached the end-point of the study, the weight (30.8 ± 4.0 g and 31.0 ± 4.7

g for ID8 and ID8+PCL, respectively) and abdomen size (1060 ± 220 mm^2 and 1080 ± 310 mm^2 for ID8 and ID8+PCL, respectively) of these mice were similar whether or not mice received PCL-only scaffolds (**Fig. 4.3D&E**). Control mice had an average weight of 25 ± 0 g and an abdomen size of 570 ± 30 mm^2. Lastly, the pancreas was observed to be significantly infiltrated with metastases in ID8 mice, so blood glucose level was compared across experimental groups to evaluate whether it could be used as a metric for monitoring disease progression. However, across all groups - including naïve mice - glucose levels were not found to be significantly different (**Fig. 4.3F**).

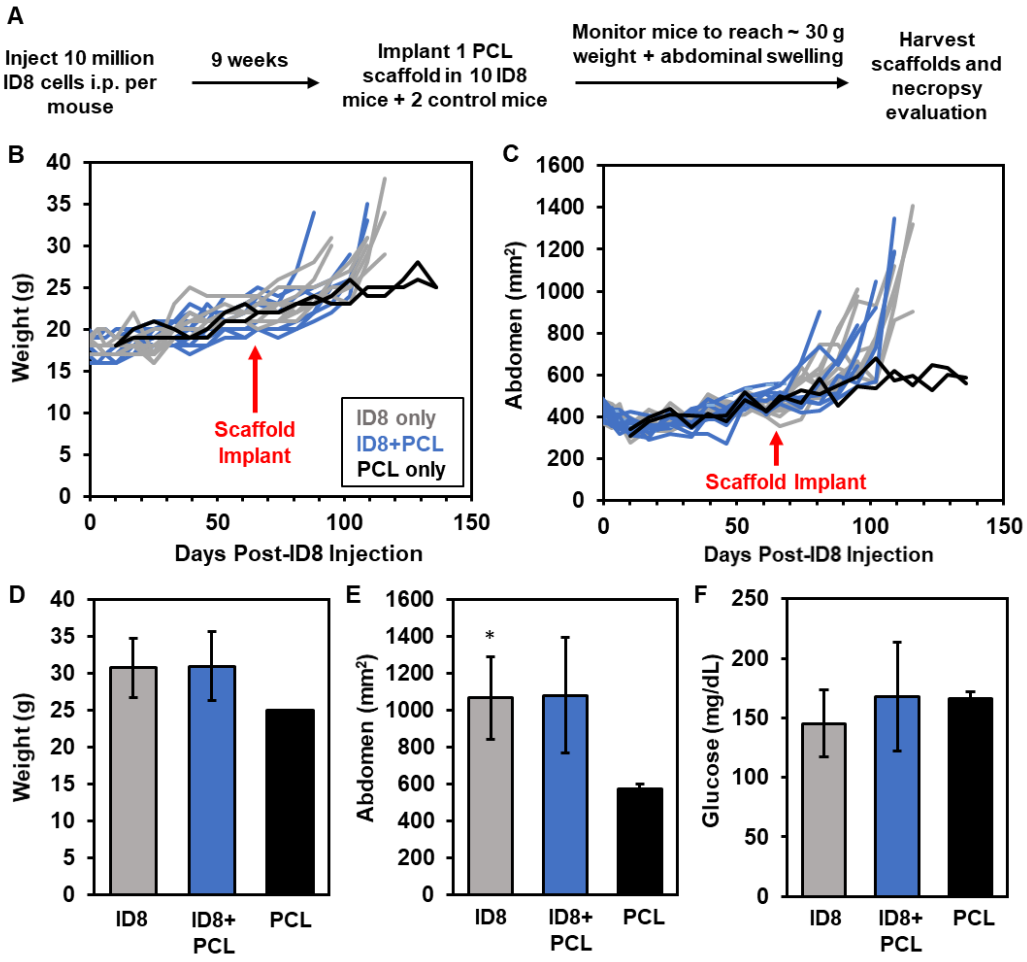

Figure 4.3: Study of PCL-only scaffolds implanted during disease progression. (**A**) Timeline for ID8 ovarian cancer mouse study where PCL-only scaffolds were implanted after ID8 cell injection. (**B,C**) Comparison of weight (**B**) and abdomen size (length×width, **C**) over time after

ID8 cell injection across different experimental groups. (**D**-**F**) Average values for weight (**D**), abdomen size (**E**), and glucose level (**F**) at the 30 g weight and visual abdominal swelling disease end-point. *indicates P-value < 0.05 relative to "PCL" control group.

Further, at disease end-point, mice receiving ID8 cells had a significant amount of ascites fluid (11.3 ± 4.6 mL and 12.2 ± 5.2 mL for ID8 and ID8+PCL, respectively, **Fig. 4.4A**). The maximum nodule size on the i.p. lining was found to be larger on average - although not statistically significant - in ID8 mice that did not receive PCL-only scaffolds than in ID8 mice with PCL-only scaffolds implanted at 9 weeks (**Fig. 4.4B**). Additional characterization of the disease state in the ID8 model at the end of this study was done through disease scoring of various tissues and organs in the abdominal cavity (**Fig. 4.4C**). In most ID8 mice with or without PCL-only scaffolds, the i.p. lining and pancreas were assigned a disease score of ~3 (2.9 ± 0.3 and 3 ± 0 for i.p. lining of ID8 and ID8+PCL, respectively, while both groups have a pancreas score of 3 ± 0), where extensive metastases are visible throughout. The liver was observed to have lower disease burden (disease scores of 1.8 ± 0.4 and 1.7 ± 0.5 for ID8 and ID8+PCL, respectively), where most mice had moderate metastases in multiple areas of the liver. Overall, extensive metastases were evident throughout the peritoneal cavity in all ID8 mice.

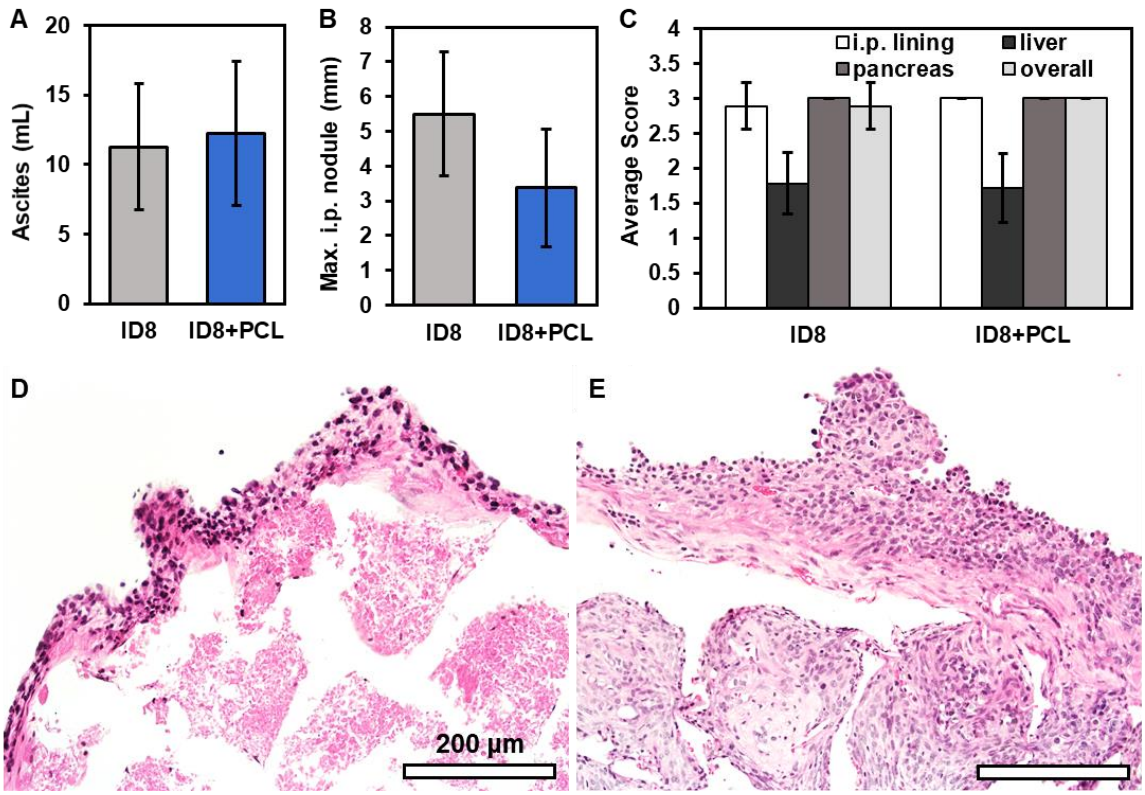

Figure 4.4: PCL-only scaffolds implanted during disease progression capture ID8 cells. (**A,B**) Amount of ascites fluid (**A**) and maximum i.p. nodule size (**B**) in ID8 mice without ("ID8") or with PCL-only scaffolds ("ID8+PCL") at the 30 g weight and abdominal swelling disease end-point. PCL-only scaffolds were implanted at 9 weeks post-ID8 injection. (**C**) Extent of disease by visual scoring of the i.p. lining, liver, pancreas, and all organs/tissues ("overall") at the disease end-point. (**D**) H&E staining of a PCL-only scaffold that was found floating in ascites fluid in the abdominal cavity. (**E**) H&E staining of a PCL-only scaffold that was found attached to the i.p. wall. Scale bar indicates 200 µm.

When PCL-only scaffolds were harvested for histology, it was observed through H&E staining that most scaffolds had captured ID8 cells on the border of the scaffold with evidence of nodules forming (**Fig. 4.4D**). Cell infiltration into the scaffolds was observed to a lesser extent, which is likely due to the late implantation of the PCL-only scaffolds (9 weeks post-ID8 injection). At this time-point, some mice had ascites fluid during scaffold implantation, and significant ascites accumulation would occur soon after, likely hindering the ability of scaffolds to become embedded in the i.p. wall and to readily capture disseminated cells. This is supported by the fact that most scaffolds were found floating in

the ascites fluid. One scaffold which was found to be embedded in the i.p. wall exhibited enhanced cell infiltration along with formation of nodules on the border of the scaffold (**Fig. 4.4E**). These findings demonstrate PCL-only scaffolds can capture disseminated ID8 cells, although they should be implanted earlier in disease progression or attached to the i.p. wall for enhanced integration. Additionally, a method to quantitatively characterize the end-stage disease state of the ID8 mouse model was implemented, and it can be used in experiments investigating earlier time-points in disease progression or when studying the therapeutic benefit of scaffold-based interventions.

4.3.3 PCL-only scaffolds implanted prior to disease formation capture disseminated ID8 cells

Conversely, an experimental scheme where PCL-only scaffolds were implanted prior to ID8 cell injection was investigated to similarly characterize how disease progresses in this case and whether PCL-only scaffolds could capture ID8 cells. A clinical scenario for this scheme would be when patients who are known to be at a higher risk of developing ovarian cancer - due to hereditary mutations (i.e. BRCA1, BRCA2)[3,192] - may receive scaffolds prior to disease formation. Most mice received PCL-only scaffolds while a group of mice received mock surgeries, and 10 weeks later, 10 million ID8 cells were injected i.p. into mice (**Fig. 4.5A**). Again, control naïve mice receiving PCL-only scaffolds but not ID8 cells were used. A sharp increase in the weight and abdomen size was observed around 90 days post-ID8 injection (**Fig. 4.5B&C**), which is consistent with the previous study. Similarly, the weight of mice receiving ID8 cells (**Fig. 4.5D**, 31.0 ±1.4 g and 30.7 ± 2.4 g for ID8 and ID8+PCL, respectively) and their abdomen size (**Fig. 4.5E**, 910 ± 160 mm^2 and 950 ± 200 mm^2 for ID8 and ID8+PCL, respectively) were not significantly different whether or not

mice received PCL-only scaffolds beforehand. The weight of PCL-only mice was lower at 25 ± 0 g and the abdomen size was on average 640 ± 20 mm^2 at the end of the study. Glucose levels were also comparable across groups and consistent with the levels of all mice in the previous study (**Fig. 4.5F**).

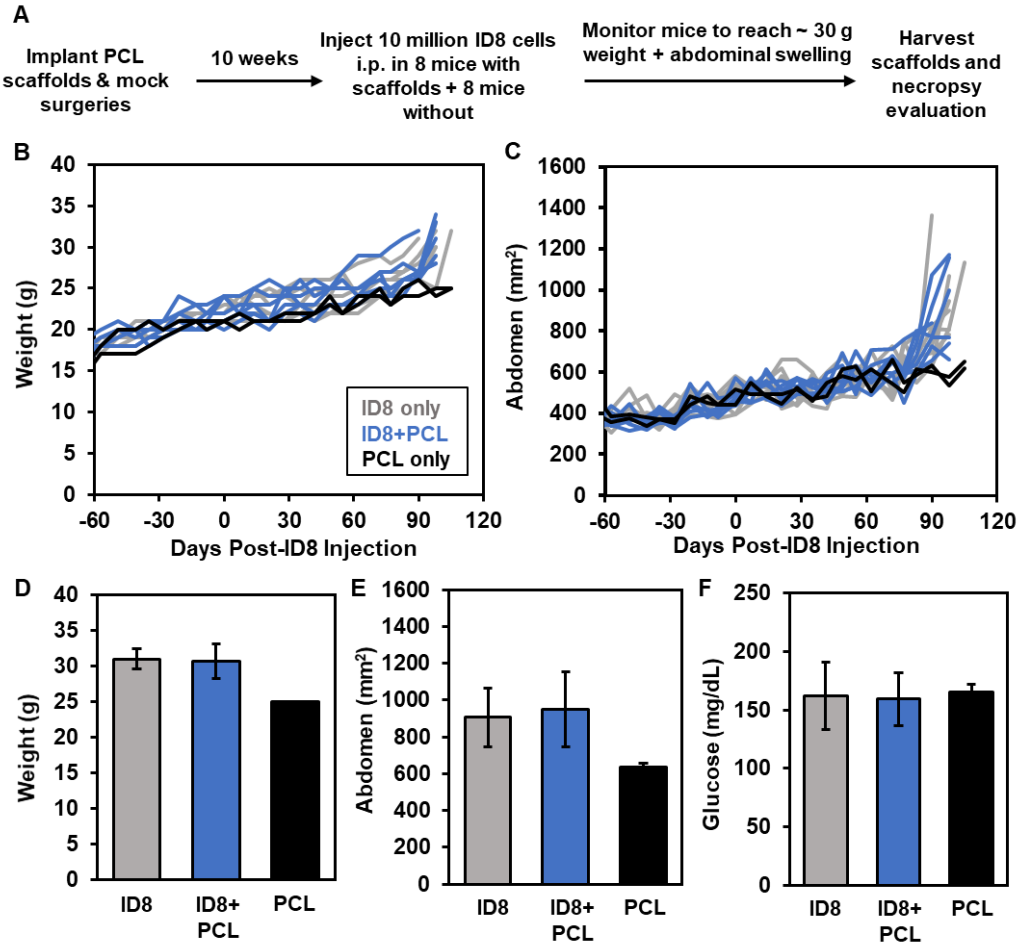

Figure 4.5: Study of PCL-only scaffolds implantated prior to disease formation. (**A**) Timeline for ID8 ovarian cancer mouse study with implantation of PCL-only scaffolds before ID8 cell injection. (**B,C**) Comparison of weight (**B**) and abdomen size (length×width, **C**) over time following ID8 cell injection across different experimental groups. (**D-F**) Average values for weight (**D**), abdomen size (**E**), and glucose level (**F**) at the 30 g weight and visual abdominal swelling disease end-point.

When comparing only the mice which received ID8 cells, the amount of ascites fluid (**Fig. 4.6A**, 8.3 ± 2.4 mL and 7.0 ± 5.4 mL for ID8 and ID8+PCL, respectively) and maximum

i.p. nodule size (**Fig. 4.6B**, 3.8 ± 1.2 mm and 2.0 ± 0.8 mm for ID8 and ID8+PCL, respectively) were similar whether or not mice had PCL-only scaffolds. Lastly, average disease scores again showed extensive metastases on the pancreas (3 ± 0 and 2.6 ± 0.5 for ID8 and ID8+PCL, respectively) and i.p. lining (2.3 ± 0.8 and 2.6 ± 0.7 for ID8 and ID8+PCL, respectively), while the liver exhibited moderate disease burden (1.1 ± 0.4 and 0.9 ± 0.4 for ID8 and ID8+PCL, respectively) (**Fig. 4.6C**).

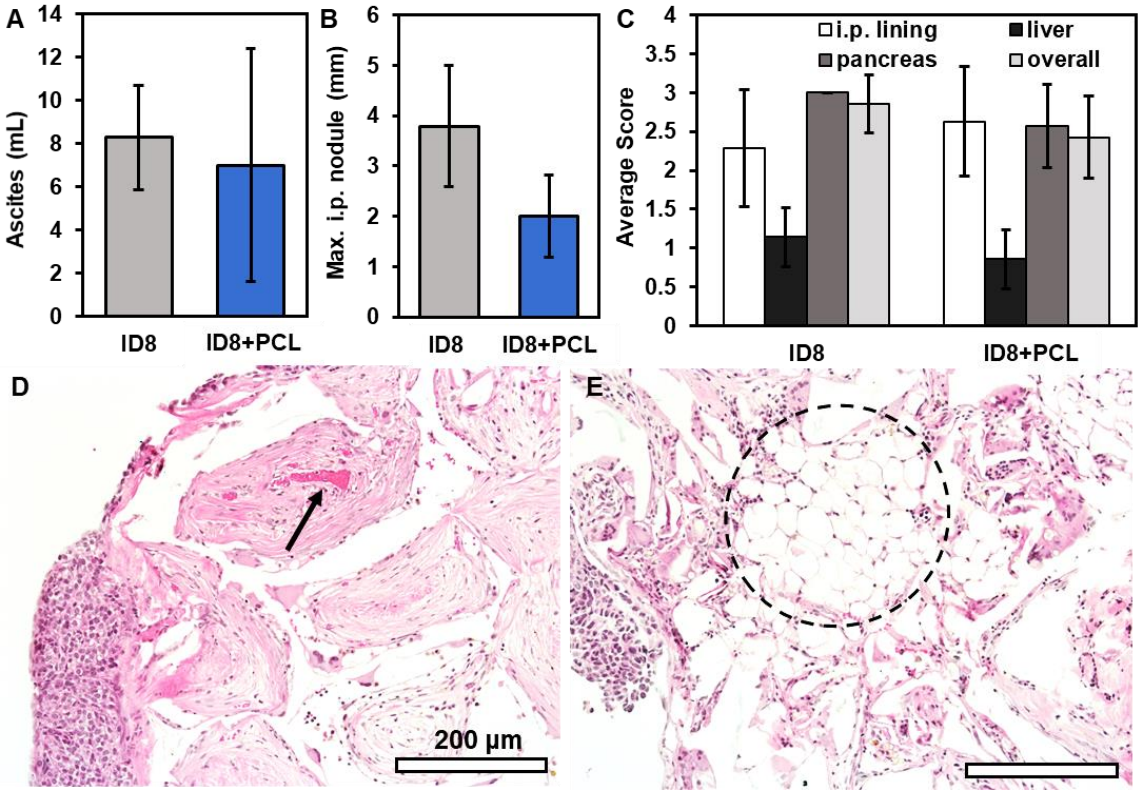

Figure 4.6: PCL-only scaffolds implanted prior to disease formation capture ID8 cells. (**A,B**) Amount of ascites fluid (**A**) and maximum i.p. nodule size (**B**) in ID8 mice without ("ID8") or with PCL-only scaffolds ("ID8+PCL") at the 30 g weight and abdominal swelling disease end-point. PCL-only scaffolds were implanted 10 weeks prior to ID8 injection. (**C**) Extent of disease by visual scoring of the i.p. lining, liver, pancreas, and all organs/tissues ("overall") at end-stage disease. (**D,E**) H&E staining of PCL-only scaffolds showing evidence of infiltration with protein and cells, as well as evidence of vessel formation (arrow, **D**) and fat deposits (dashed circle, **E**). Scale bar indicates 200 µm.

The PCL-only scaffolds in this study were mostly found embedded in the i.p. wall or in fat near the incision site, and consequently, these scaffolds were more infiltrated with

extracellular matrix and cells (**Fig. 4.6D&E**). Like before, a substantial layer of cells and evidence of metastatic nodule growth on the border of scaffolds was seen (**Fig. 4.7**), along with blood vessel formation in some scaffolds (**Fig. 4.6D**). Fat deposits within the scaffold pores were also observed which is consistent with where they were found during harvest (**Fig. 4.6E**). Overall, these two studies where PCL-only scaffolds were implanted into the abdominal cavity of advanced stage ovarian cancer mice demonstrate that PCL-only scaffolds can capture disseminated ID8 cells *in vivo*, regardless of whether scaffolds are implanted before or during disease formation.

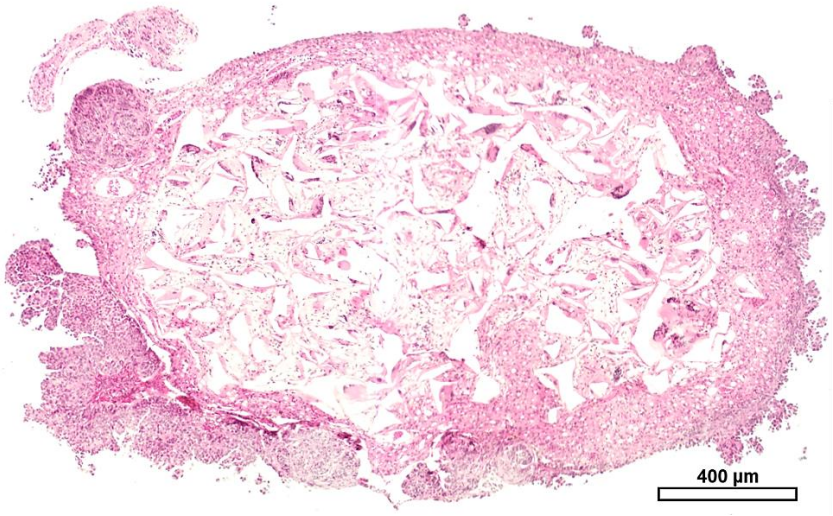

Figure 4.7: Cross-sectional view of PCL-only scaffold with captured ID8 cells. Two 10x magnification images combined to provide a full cross-sectional view of a H&E-stained PCL-only scaffold that was implanted for 10 weeks prior to ID8 cell injection. Scale bar indicates 400 µm.

4.3.4 Iron oxide-loaded scaffolds become infiltrated with ID8 cells throughout disease progression

Lastly, we wanted to 1) verify iron oxide-loaded scaffolds could capture disseminated ID8 cells *in vivo* and 2) identify how early in disease progression these cells would be evident at the scaffold to inform the design of future therapeutic studies using iron oxide-loaded

scaffolds under AMF. All mice received 10 million ID8 cells i.p., and 4.5 weeks later, 2 iron oxide-loaded scaffolds were implanted into the i.p. cavity of each mouse (**Fig. 4.8A&B**). This timeline was chosen since the primary therapeutic application of iron oxide-loaded scaffolds would be when patients have residual disease after debulking surgery or in early stages of recurrence after unsuccessful chemotherapy. At 8.5, 10.5, and 11.5 weeks post-ID8 injection, necropsy evaluation was completed and iron oxide-loaded scaffolds were harvested to characterize disease progression and ID8 cell infiltration of scaffolds prior to significant disease formation (~14 to 16 weeks).

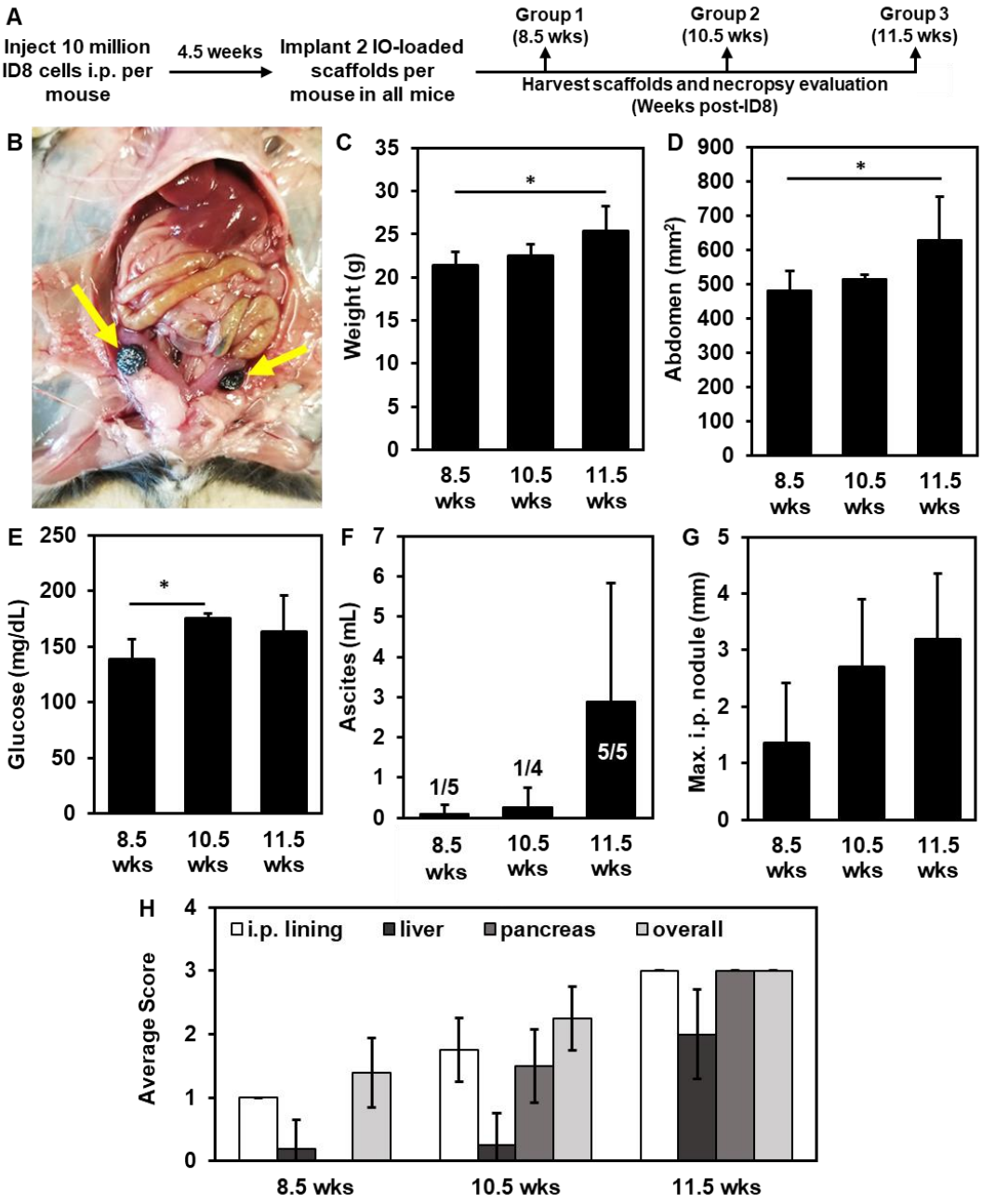

Figure 4.8: Study of iron oxide-loaded scaffolds implanted 4.5 weeks post-ID8 injection then harvested at various timepoints during disease progression. (**A**) Timeline for ID8 ovarian cancer mouse study in which 2 iron oxide-loaded scaffolds were implanted 4.5 weeks after ID8 cell injection, and scaffolds were harvested at various timepoints during disease progression. (**B**) Image of mouse during necropsy evaluation and location of iron oxide-loaded scaffolds (arrows) in the abdominal cavity. (**C-E**) Comparison of average weight (**C**), abdomen size (length×width, **D**), and glucose level (**E**) at various timepoints during disease progression (weeks post-ID8 injection). (**F,G**) Amount of ascites fluid (**F**) and maximum i.p. nodule size (**G**) observed during necropsy evaluation at various timepoints during disease progression. Fractions in (**F**) indicate portion of mice with ascites in each group. (**H**) The extent of disease by visual scoring of the i.p. lining, liver, pancreas, and all organs/tissues ("overall"). *indicates P-value < 0.05 between indicated groups.

Because necropsy evaluation occurred at multiple time-points during disease progression, the weight and abdomen size increased over time (**Fig. 4.8C&D**). Glucose levels for each group were also measured (**Fig. 4.8E**), and although the glucose level at 10.5 weeks post-ID8 injection was significantly higher than at 8.5 weeks post-ID8 injection, further studies would need to be done to ensure this finding is consistent. Overall, the glucose levels in this study were similar to previous values in the PCL-only scaffold studies.

The amount of ascites fluid and maximum i.p. nodule size also increased over time (**Fig. 4.8F&G**). Although the difference in average ascites fluid amount was not statistically significant across time-points, it is important to note that only one mouse at 8.5 weeks and 10.5 weeks post-ID8 injection had ascites fluid (0.5 mL and 1 mL, respectively), while all mice at 11.5 weeks post-ID8 injection had notable ascites accumulation (0.5 to 7 mL) (**Fig. 4.8F**). Disease scores of organs and tissues in the abdominal cavity also increased over time (**Fig. 4.8H**). At 8.5 weeks post-ID8 injection, a disease score of 1 was given to all mice for the i.p. lining (indicating some metastatic nodules isolated to a single region), while most mice in this group had no visual metastases on the liver or the pancreas. However, just 2 weeks later, mice were observed to have moderate metastases formation on the i.p. lining and pancreas, with 10 - 20% of the pancreas having visible disease. By 11.5 weeks post-ID8 injection, most mice have extensive metastases across the i.p. lining and pancreas (80% covered) and moderate to extensive metastases on the liver. These findings indicate that future therapeutic studies investigating hyperthermic treatment of iron oxide-loaded scaffolds under AMF should utilize hyperthermic treatment prior to 11.5 weeks post-ID8 injection before the disease burden is too high. Additionally, the

quantitative method which was developed to characterize the disease state of the ID8 model was further validated and was shown to be indicative of disease progression over time.

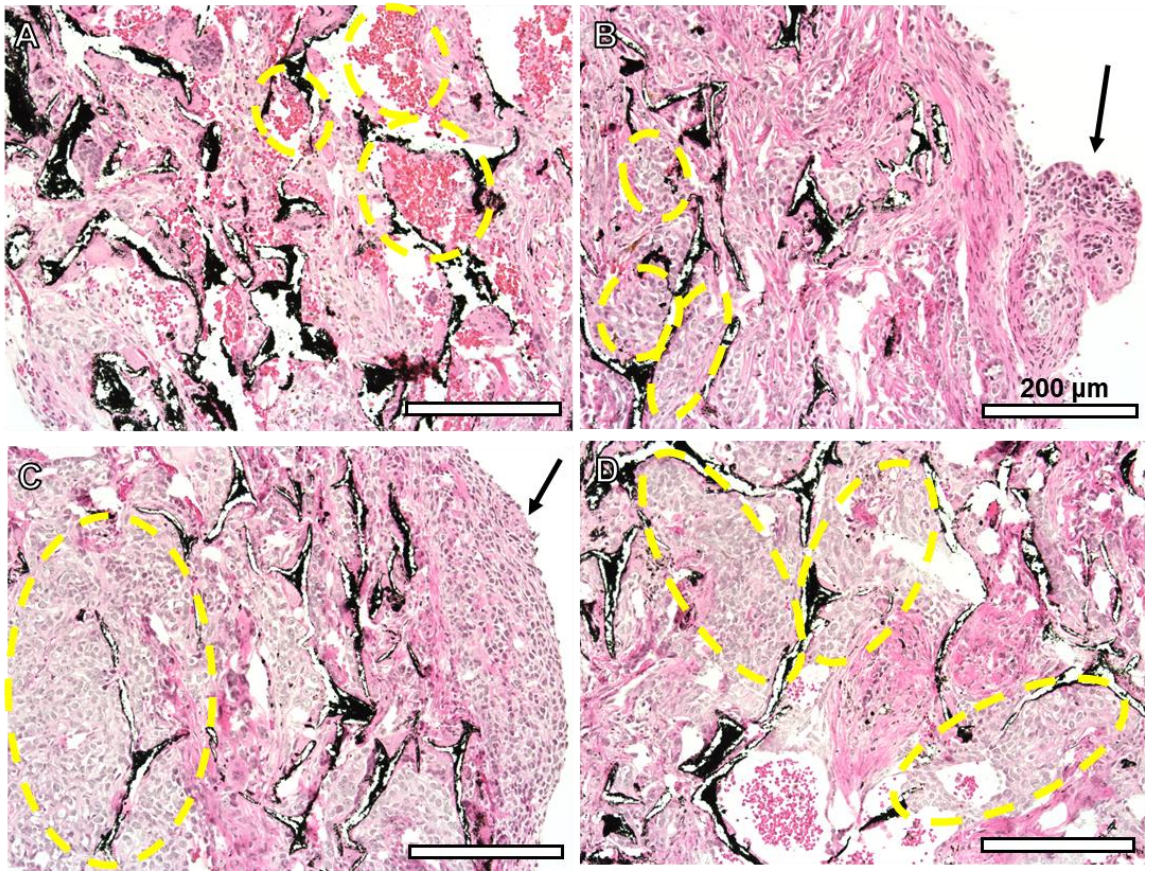

Figure 4.9: Iron oxide-loaded scaffolds capture ID8 cells throughout disease progression. Images of H&E staining of an iron oxide-loaded scaffold with presence of blood from ascites fluid (dashed circles) within pores at 8.5 weeks post-ID8 injection (**A**) and iron oxide-loaded scaffolds harvested at 8.5 weeks (**B**), 10.5 weeks (**C**), and 11.5 weeks (**D**) post-ID8 injection. Nodules and tumor cell clusters can be seen on the edges of the scaffolds (arrows, **B & C**) and cancer cells are observed within all scaffolds as clusters of large, misshapen nuclei (dashed circles, **B-D**). Black material in images is iron oxide left behind after processing and staining. Scale bar indicates 200 µm.

Lastly, H&E staining of iron oxide-loaded scaffold sections was completed to characterize the infiltration and capture of ID8 cells over time. Evidence of ascites (red blood cells, dashed circles) within scaffold pores was observed in some iron oxide-loaded scaffolds (**Fig. 4.9A**). Importantly, even at the earliest evaluated time-point of 8.5 weeks post-ID8 injection, clusters of large, misshapen nuclei (dashed circles) were seen throughout the iron

oxide-loaded scaffolds, indicating successful infiltration of ID8 cancer cells (**Fig. 4.9B**). Further, evidence of nodule formation on the border of iron oxide-loaded scaffolds (arrow) is seen even at this stage of disease. Consequently, at later time-points of 10.5 and 11.5 weeks post-ID8 injection, these clusters of ID8 cells (dashed circles) are even larger and can fill almost the entirety of iron oxide-loaded scaffold pores (**Fig. 4.9C&D**). Again, large nodules appear to be forming on the scaffold border (arrow, **Fig. 4.9C**). Overall, these findings show that iron oxide-loaded scaffolds can successfully capture disseminated ID8 cells *in vivo* (both within and on the outside of scaffolds), and more importantly, ID8 cells are observed at the iron oxide-loaded scaffolds prior to significant disease formation.

4.4 Discussion

Due to the lack of treatment options for advanced stage ovarian cancer patients, this chapter focused on further investigating whether our previously developed PCL-only and iron-oxide loaded scaffolds could be used as an alternative treatment modality for disseminated disease. More specifically, the potential of these scaffolds to capture disseminated cancer cells *in vivo* in an advanced stage ovarian cancer mouse model was investigated. First, tumor inoculation was optimized in order to successfully implement this model, which was new to our group, and it was determined that ID8 cell number and the needle size used for i.p. injection of the cells were critical for successful establishment of metastatic disease in the model (data not shown). Because this work aims to help advanced stage ovarian cancer patients, the ID8 mouse model was verified to exhibit hallmarks of advanced patient disease, such as ascites accumulation and metastases throughout the abdominal cavity. In ID8 mice, significant accumulation of ascites fluid resulted in visual abdominal swelling

which was used as a metric for end-stage disease. This characteristic of the mouse model is clinically-relevant, as most ovarian cancer patients will present with advanced stage disease at time of diagnosis and some will already have ascites[193]. In ovarian cancer patients, a typical cellular distribution of 37% lymphocytes, 29% mesothelial cells, 32% macrophages, and less than 0.1% adenocarcinoma cells in ascites fluid has been reported[194]. The accumulation of ascites is due to a disrupted balance between fluid production and filtration in the peritoneal cavity[195]. Impaired fluid draining through lymphatics due to tumor cell obstruction has long been hypothesized as one of the main mechanisms for ascites accumulation[196]. Additionally, increased flow of fluid into the peritoneal cavity through enhanced microvessel permeability[197] and multiple mechanisms due to enhanced vascular endothelial growth factor (VEGF) expression[195] are suggested.

Further, ID8 mice exhibited extensive metastases (both micrometastases visualized by microscopy and macrometastases visible by eye) on the tissues and organs of the abdominal cavity. As seen in the ID8 model, ovarian cancer patients typically have locally advanced disease confined within the peritoneal cavity, and spread of ovarian cancer cells from the primary tumor differs from other cancers which often metastasize through blood vasculature[22]. Shedding of ovarian cancer cells from the primary tumor and their subsequent transport via fluid throughout the peritoneal cavity is widely accepted as one of the main routes of passive metastasis in epithelial ovarian cancer[22,198,199]. Consequently, if no accumulated fluid is present, cancer cells would be restricted to dispersing at sites nearby the primary tumor[200,201], demonstrating the significant role ascites fluid plays in ovarian cancer disease progression.

Most notably, although disseminated ovarian cancer cells spread throughout the peritoneal cavity, the distribution of metastases is not completely random, and common sites of metastasis are the peritoneum and the omentum[26]. The peritoneum is the membrane lining the peritoneal cavity and abdominal organs, and ovarian cancer cells will adhere to its outer layer called the mesothelium, then upregulate matrix metalloproteinase-2 (MMP-2) to invade further into the cell layer[22]. Knowing that disseminated ovarian cancer cells are typically confined within the peritoneal cavity of patients and will spread to the peritoneum, the i.p. wall was chosen as the site of scaffold implantation to increase the capture of disseminated cancer cells.

Another consideration with the ID8 mouse model used here is that since the tumor cells are injected i.p., this model is representative only of late stage disease where cancer cells are already in a disseminated state. I.p. injection of tumor cells is a standard method for establishing disease in ovarian cancer mouse models; however, an advanced stage ovarian cancer mouse model can be achieved through orthotopic injection of ID8 cells into the ovarian bursa of female mice, allowing primary tumors to grow first followed by metastatic spread[202–204]. An orthotopic model and natural progression to metastatic disease is indeed more representative of what will occur in patients, but the procedure to inject ID8 cells directly into the ovarian bursa is much more complex and requires surgery when compared to a simple i.p. injection. However, it may be advantageous to use an orthotopic ID8 mouse model in future studies to establish whether iron oxide-loaded scaffolds can capture disseminated ID8 cells even during the earliest stages of metastasis from a primary tumor.

Regardless of whether or not PCL-only scaffolds were implanted, a sharp increase in weight and abdomen size began around 90 days post-ID8 injection in all ID8 mice. These

results were consistent with findings observed by Greenaway *et al*., where ID8 orthotopic tumors were first formed and by 90 days post-injection, significant peritoneal metastases and ascites fluid were present[203]. Further, the original work describing the creation of the ID8 cell line reports that the average time to death (determined by visual abdominal swelling) was 114 ± 3 days[167] in mice, which is close to the time it took our ID8 mice to reach the disease end-point metric of 30 g and visual abdominal swelling (14 to 16 weeks). The consistency in disease progression across these studies and ours demonstrates the robustness of the disease timeline for the ID8 model. Although the disease timeline is consistent, the ID8 cells do not express a fluorescent or bioluminescent marker, which makes tracking the disease burden over time and comparing experimental groups more difficult. However, a quantitative method to characterize the disease state in the ID8 mouse model was developed through necropsy evaluation, and it will be used in future therapeutic studies to track disease progression after treatment (i.e. hyperthermic treatment with iron oxide-loaded scaffolds under AMF).

The localization of ID8 cells within PCL-only scaffolds was also characterized. For the PCL-only scaffolds that were implanted during disease progression, most scaffolds were found floating in ascites with ID8 cells primarily seen on the scaffold border, while one scaffold that was found to be embedded in the i.p. wall had enhanced cell infiltration. Capture of ID8 cells primarily on the border is likely because the scaffolds were implanted too late into disease progression (9 weeks post-ID8 injection). Mice will begin to accumulate ascites fluid shortly after this time, and a couple of mice already had some ascites during scaffold implantation. Significant fluid accumulation and fluid flow would hinder the integration of scaffolds into the i.p. wall and consequent cell migration and

infiltration into scaffolds. Furthermore, previous studies showed PCL-only scaffolds implanted at this location in naïve mice exhibited cell infiltration. Additional studies where scaffolds are attached to the i.p. wall during implantation (i.e. using surgical glue) should be completed to determine if scaffolds can still become infiltrated with cells in the presence of ascites fluid. These studies would indicate whether scaffold integration into the i.p. wall is necessary for successful cell infiltration or if significant fluid in the peritoneal cavity alone would disrupt cell adherence and migration into scaffolds. If scaffolds cannot effectively capture ID8 cells when significant ascites fluid is present, scaffolds could be implanted earlier in disease progression prior to formation of ascites or ascites fluid could be periodically drained - which is routinely done in patients - after scaffold implantation.

When PCL-only scaffolds were implanted prior to ID8 cell injection, most scaffolds were found to be embedded in the i.p. wall or in fat. All of these scaffolds exhibited tissue infiltration within the scaffold pores, in addition to evidence of metastatic nodule formation on the scaffold border. Scaffold embedment into fat in the peritoneal cavity and evidence of fat within scaffold pores are interesting since 80% of serous ovarian cancer patients will have metastases at the omentum[205], a fat pad made up largely of adipocytes. Further, numerous studies have found evidence strongly suggesting adipocytes contribute to the homing, migration, and proliferation of metastatic ovarian cancer cells[199,205], and the fat surrounding and within scaffolds could also be aiding in ID8 cell recruitment. These studies demonstrated that PCL-only scaffolds could capture disseminated cancer cells in an advanced stage ovarian cancer mouse model, whether the scaffolds were implanted before ID8 cell injection or during disease formation. These PCL-only scaffolds have previously been shown to capture metastatic cancer cells in a breast cancer mouse model[76,77,85];

however, this is the first time they have been shown to capture disseminated ovarian cancer cells *in vivo*.

In a final study, iron-oxide loaded scaffolds were investigated for their potential to capture ID8 cells *in vivo*. Iron oxide-loaded scaffolds were implanted earlier in disease progression (4.5 weeks post-ID8 injection) because this timeline is most clinically-relevant, as patients could receive iron oxide-loaded scaffolds to treat residual disease after debulking surgery or after detecting recurrence. Necropsy evaluation occurred at 8.5, 10.5, and 11.5 weeks post-ID8 injection, and trends of increasing values in weight, abdomen size, ascites fluid, maximum i.p. nodule size, and disease scores were observed over time which was expected due to disease progression. Interestingly, disseminated ID8 cells were observed at iron oxide-loaded scaffolds at all these time-points, and extensive disease formation was not necessary for ID8 cells to be captured, indicating AMF treatment could be given prior to significant disease burden. Because ID8 cells are captured at iron oxide-loaded scaffolds and we previously demonstrated that cells within iron oxide-loaded scaffolds can be killed non-invasively under AMF[206], future *in vivo* studies investigating whether this modality can be used for a therapeutic benefit are warranted. As mentioned in Chapter 3, a larger coil is needed for this, so that the mouse and the entire implanted iron oxide-loaded scaffold can be uniformly treated under AMF *in vivo*. Although no significant differences were observed in the disease progression between ID8 mice that received PCL-only scaffolds and ID8 mice that did not, iron oxide-loaded scaffolds could slow disease progression by repeatedly heating and killing captured ID8 cancer cells to lower disease burden and by also potentially eliciting an antitumor immune response. To address ID8 cells observed on the scaffold border, a longer AMF treatment time could be used, where the surrounding

tissue around the iron oxide-loaded scaffold would reach appropriate temperatures for cell death[85]. Another option is to find earlier timepoints where a significant layer of cells do not form on the scaffold border, and treating at an earlier time in disease progression would be beneficial because a significant volume of ascites fluid in the peritoneal cavity at later stages of disease would affect the heating and heat transfer of iron oxide-loaded scaffolds. Future studies investigating whether ID8 cells are observed at iron oxide-loaded scaffolds prior to 8.5 weeks post-ID8 injection should be considered, as it is highly likely that ID8 cells would be observed at these scaffolds earlier although in lesser numbers. Overall, this last finding that ID8 cells are captured by iron oxide-loaded scaffolds prompts future work investigating whether ID8 cells which are killed via hyperthermic treatment can elicit an antitumor immune response and mitigate disease progression.

Chapter 5: Conclusions and future directions

5.1 General conclusions

The overall goal of this research was to improve ovarian cancer treatment through development of innovative biomaterial-based approaches which could help address the long-standing clinical challenges of recurrence, chemoresistance, and limited therapeutic options for advanced stage disease. In the first project, ovarian cancer cell response to immobilization in stiff silica gels was extensively characterized. While most immobilized cells die within days, it was discovered that a subset of ovarian cancer cells have enhanced survival under physical confinement by entering dormancy. These cells that survived immobilization could be extracted from gels and demonstrated enhanced survival upon re-immobilization relative to the starting population, indicating that immobilization quickly identifies a unique subpopulation that can readily enter dormancy in order to tolerate physical confinement stress. These cells also exhibited enhanced resistance to cisplatin and paclitaxel, despite being proliferative during treatment. Other *in vitro* platforms which have been used to study quiescence were unable to effectively select for chemoresistant ovarian cancer cells upon lifting the environmental stress, demonstrating that the rapid selection of chemoresistant cells after stress removal is unique to the silica gel platform. Lastly, ovarian cancer cells which were more resistant to both types of chemotherapy had enhanced survival in silica gels relative to more chemosensitive cells.

In the next project, iron oxide particles were incorporated into biomaterial scaffolds which have previously been shown to recruit metastatic breast cancer cells[76,77,85]. After successful incorporation of iron oxide into scaffolds, it was demonstrated that simple design

parameters, such as iron oxide loading amount and magnetic field strength, could be tuned to alter the heating of iron oxide-loaded scaffolds under an alternating magnetic field (AMF). Addition of iron oxide into scaffolds did not cause significant cytotoxicity, and ID8 ovarian cancer cells were effectively heated and killed in iron oxide-loaded scaffolds under AMF *in vitro*. These scaffolds were implanted into the abdominal cavity of female mice and became infiltrated with tissue after 6-7 weeks. When removed and placed in the center of a radiofrequency coil, tissue-laden iron oxide-loaded scaffolds effectively killed infiltrated cells *ex vivo* under AMF. It was lastly demonstrated that implanted iron oxide-loaded scaffolds could be used to successfully kill infiltrated cells *in vivo* in a non-invasive manner under AMF.

In final studies, an advanced stage ovarian cancer mouse model using the ID8 cell line was verified to exhibit hallmarks of advanced patient disease, including ascites accumulation and extensive metastases within the peritoneal cavity. A quantitative method using necropsy evaluation was implemented to characterize the disease state during disease progression and at the end-stage of disease. PCL-only scaffolds were able to capture disseminated ID8 cells *in vivo* in the advanced stage mouse model, regardless of whether they were implanted before ID8 injection or during disease progression. Most importantly, iron oxide-loaded scaffolds captured ID8 cells prior to significant disease formation, indicating that hyperthermic treatment of cancer cells could be administered prior to extensive disease burden. With this last finding and previous work showing iron oxide-loaded scaffolds can kill infiltrated cells under AMF *in vivo*, future studies investigating whether this treatment modality can provide a therapeutic benefit are of significant interest.

5.2 Future directions

5.2.1 Silica gel immobilization of patient ovarian cancer cells to predict patient outcome

In Chapter 2, chemoresistant ovarian cancer cells demonstrated a differential response - as evidenced by enhanced survival - to physical confinement when compared to cells which were more chemosensitive. Similarly, ovarian cancer cells with enhanced ability to enter dormancy also showed enhanced survival upon immobilization. Because these ovarian cancer cell populations can lead to recurrence, studies should be done to investigate whether patient tumor cell survival within silica gels indicates whether or not patients may have these evasive types of cancer cells and are at high risk of recurrence.

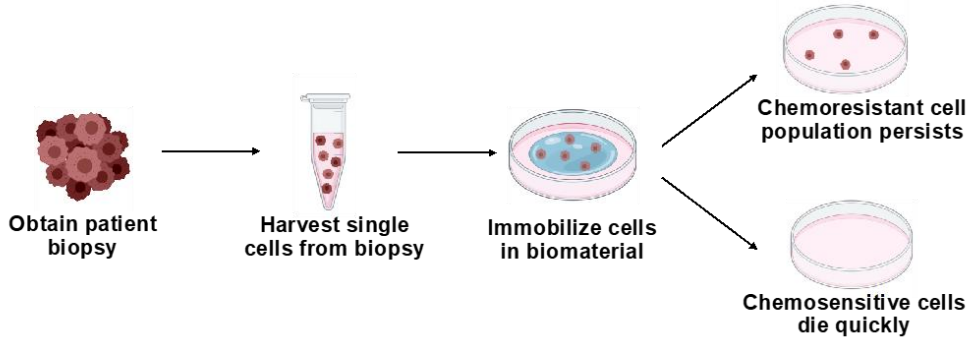

Figure 5.1: Schematic of silica gel immobilization of ovarian cancer patient cells to investigate whether patient tumor cell survival is indicative of a patient's response to chemotherapy or risk of recurrence.

In preliminary studies immobilizing cells from patient samples (**Fig. 5.1**), samples were obtained from the UMN Tissue Procurement Facility, and the Miltenyi Biotec Tumor Dissociation Kit protocol was used to isolate cells for encapsulation. The protocol utilizes enzymatic degradation to break down the extracellular matrix and other unwanted proteins comprising the tumor's tissue structure, followed by homogenization of the sample using a dissociator and mesh filter to mechanically remove any remaining tissue fragments leaving a cell suspension. Steps including accutase treatment to aid in further singularizing

cells and use of red blood cell lysis buffer to remove red blood cells were added to this protocol. This protocol provides a suitable method for initial collection of cells from tumors; however, all cells present in the tissue sample – including stromal cells such as fibroblasts – will be collected.

Since the existing protocol will collect most cell types from the tumor sample, an additional step separating the ovarian cancer cells from the other stromal cells is required. It was predicted that many of the undesired cells retrieved from patient tumor samples would be fibroblasts as they are one of the most abundant cell types in the tumor stroma[207]. Previous reports have shown that separation of fibroblasts from other cells in solution may be completed by taking advantage of the relatively fast adhesion rate of fibroblasts[208], and fibroblasts have been successfully removed by using a short incubation period where fibroblasts will adhere quickly to the flask surface and ovarian cancer cells will be left in suspension[209]. In our preliminary studies, an incubation period of 30 minutes for selective adherence of fibroblasts was used, and this incubation time should be further validated or optimized for the condition where most fibroblasts have adhered to the surface while ovarian cancer cells remain in suspension. Fibroblast removal efficiency should be determined using appropriate cell markers such as cytokeratin-7/CA-125 and CD90[210,211] for ovarian cancer cells and fibroblasts, respectively. Cytokeratin-7 is characterized as an ovarian epithelial marker[212], and CA-125 is used as a standard ovarian cancer marker by clinicians[213,214].

If this method utilizing a short incubation period for selective adherence of fibroblasts results in poor fibroblast removal, previously used methods including cold Trypsin/EDTA

washes, culture in low-serum media, or magnetic bead separation may be tested as well[211]. It is likely that some stromal cells will be encapsulated within silica gels since 100% removal would be extremely difficult, but ovarian cancer cells can be specifically stained for within silica gels (i.e. cytokeratin-7 and CA-125 used in our preliminary work). Immobilization of a small number of stromal cells may not greatly alter the results of ovarian cancer cell survival within silica gels, as previous work has shown that non-cancerous cell types demonstrate a rapid drop in metabolic activity after 1 – 1.5 days within silica gels[98]. However, future experiments should be done to verify these cells will die off quickly. Overall, if the cell extraction efficiency from samples and/or viability is found to be too low prior to immobilization, alternative protocols for collecting cancer cells from ovarian cancer biopsy samples that have been successfully used by Strauss *et al.* or Pribyl *et al.* could be explored[215,216].

After immobilization of ovarian cancer cells in silica gels, cell survival should be evaluated over a one-week period as done in previous work (**Fig. 5.2**), and the patient's response to chemotherapy quantified by duration of progression-free survival (PFS) and the duration until recurrence following completion of treatment should be monitored. If strong correlations between cell survival and rate of recurrence/PFS are found, silica gel immobilization may be promising as a method to predict which patients are likely to recur. Further, if initial studies with ovarian cancer cells from tumor samples appear promising, ovarian cancer cells collected from the ascites fluid of patients may be encapsulated for another set of studies. This could also be an alternative option if there is difficulty isolating enough viable ovarian cancer cells from primary tumor samples, as cancer cells can be isolated from ascites fluid with less difficulty[209]. Overall, if a statistically significant

difference in survival of immobilized cells is observed between patients who recur within six months of completing treatment (chemoresistant) and patients who do not, these results may indicate the potential use of silica gels as a method to quickly identify patients who are likely to recur or have a poor response to chemotherapy.

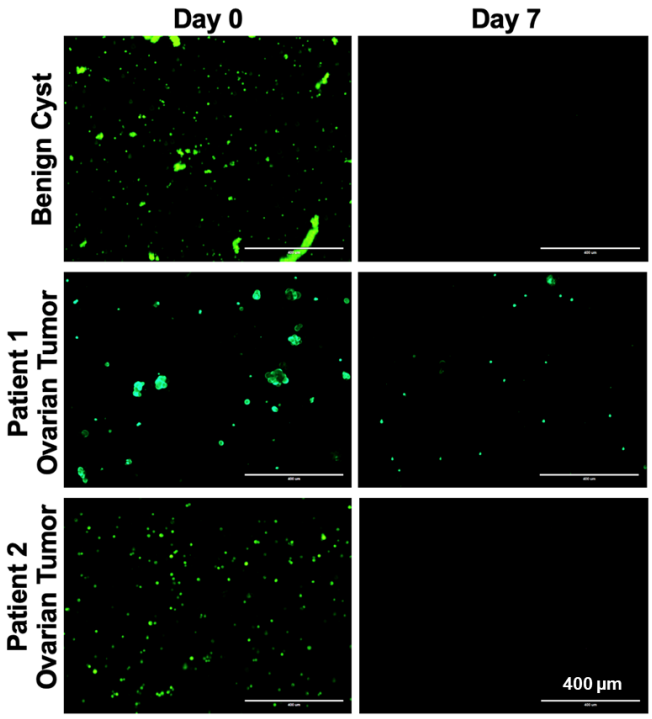

Figure 5.2: Preliminary studies evaluating cell survival upon silica gel immobilization using cells from various patient samples (both benign and malignant samples). Viable immobilized cells were stained and imaged at Day 0 and 7 of immobilization. Multi-cellular clusters are shown in images but additional optimization has improved singularization of cells prior to immobilization. Scale bar indicates 400 µm.

5.2.2 Mechanistic studies to probe findings of RNA sequencing data analysis

Experiments investigating findings from RNA sequencing data analysis of immobilized, extracted, and cisplatin-treated ovarian cancer cells are of interest. These data provided insight on the transcriptome-level response of surviving ovarian cancer cells to being physically confined or to being treated with cisplatin. Identifying altered signaling pathways in these cells relative to control cells cultured in standard 2-D conditions may

explain how cells within silica gels are entering dormancy under immobilization stress. A potential mechanism that has been identified from the RNA sequencing data involves activation of interferon signaling pathways.

Multiple analyses indicated altered interferon signaling in our samples. The fold change in gene expression of genes known to become activated during interferon signaling (*IFIT1*, *IFIT2*, *OAS1*, and *MX1*) were significantly upregulated in all samples relative to controls (data not shown). Further, "Type 1 Interferon Signaling Pathway" was an enriched term in gene ontology (GO) enrichment analysis of Day 1 and Day 3 immobilized samples, and "Interferon Signaling" was identified as the most activated top canonical pathway (by z-score) for these samples using Ingenuity Pathway Analysis (IPA) (**Fig. 5.3A**). Also from IPA, the upstream regulators function - which identifies regulators that are most likely to have caused the differential gene expression exhibited by our samples - identified many different interferons as potential activators of the differential gene expression we observed in our immobilized samples (**Fig. 5.3B**).

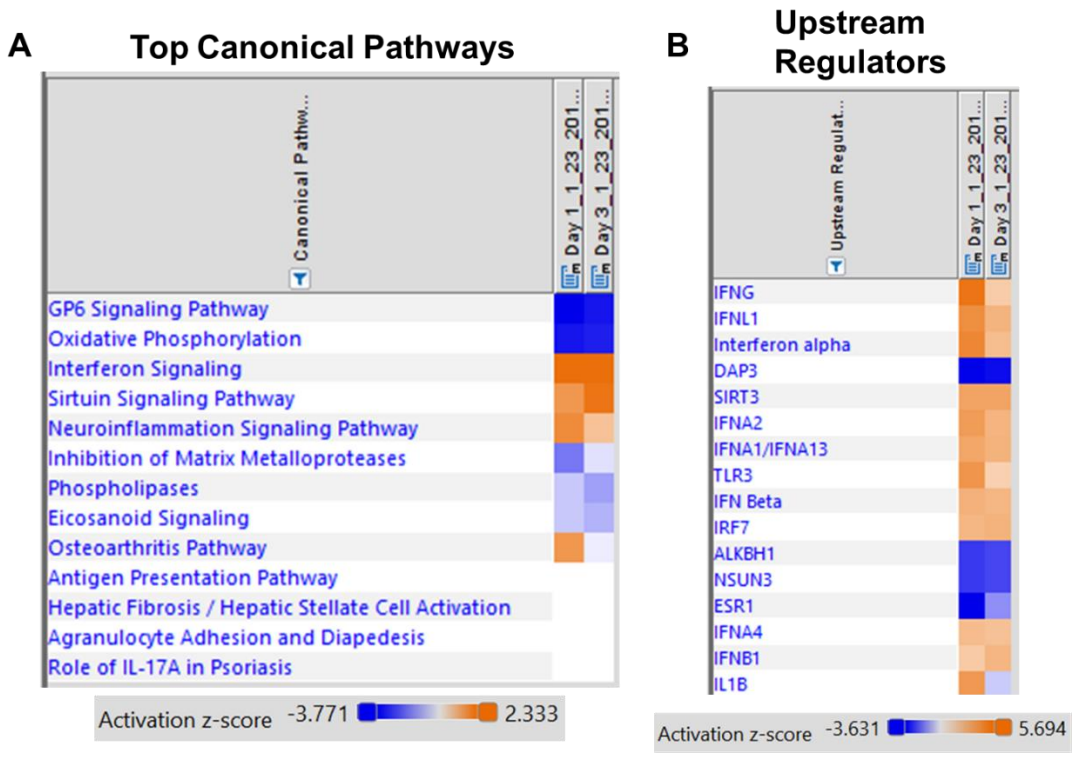

Figure 5.3: In Ingenuity Pathway Analysis, differentially expressed genes of Day 1 and Day 3 immobilization samples were used, and differentially expressed genes were defined as genes with abs(log_2FC) > 1, P-value < 0.05, and FDR < 0.05. **(A)** Top canonical signaling pathways (by z-score) shared between Day 1 and Day 3 samples identified by IPA, where the activation z-score indicates the level of predicted activation (orange) or inhibition (blue) of a pathway based upon the differential expression of the genes. **(B)** Top upstream regulators (by z-score) predicted to lead to the differential expression observed in Day 1 and Day 3 samples, where the activation z-score indicates the level of predicted activation (orange) or inhibition (blue) of a regulator based upon the differential expression of the genes.

Further analysis of the RNA sequencing data showed that the fold change in gene expression for interferon-alpha (*IFNA1*), interferon-beta (*IFNB1*), and interferon-gamma (*IFNG*) was negligible, but the fold change in gene expression of the gene for interferon-lambda (*IFNL1*) was increased relative to controls in all experimental groups. It was later verified with RT-qPCR that *IFNL1*, *OAS1*, and *MX1* were significantly upregulated in Day 1 and Day 3 samples relative to controls (data not shown). Using an ELISA, evidence of interferon-lambda present in the media from silica gels with OVCAR-3 cells immobilized for 3 days was observed, but it was present in very low amounts (data not shown). Future

studies investigating if soluble interferons are being secreted by immobilized cells and causing downstream signaling in an autocrine or paracrine manner would be interesting, since interferons have previously been implicated in cell cycle arrest in multiple types of cancer. In gastric carcinoma cells, interferon-alpha and -gamma suppressed growth *in vitro* by inducing cell cycle arrest[217], and interferon-lambda-1 was shown to specifically induce arrest in the G1 phase[109]. Similarly, G1 phase cell cycle arrest without apoptosis induction was observed in renal cancer cells *in vitro* due to interferon-alpha activation of parts of the Jak-Stat pathway[218]. Induction of p21 - a cyclin dependent kinase inhibitor that promotes cell cycle arrest under cellular stress - and growth inhibition were observed in ovarian and colon cancer cell lines after treatment with interferon-gamma[219] and type I interferons[220], respectively. We also observed statistically significant upregulation of the *CDKN1A* gene (which codes for p21) in our immobilized samples relative to controls using RT-qPCR (data not shown). Overall, the RNA sequencing data has provided avenues for identification and exploration of genes and pathways altered in immobilized, extracted, and treated samples. Additional experiments could improve mechanistic understanding of how a subset of cells enter dormancy in silica gels while many will quickly undergo apoptosis instead.

5.2.3 Applying silica gel immobilization to other types of cancer cell lines and chemotherapies

Because silica gel immobilization rapidly distinguished ovarian cancer cells with enhanced chemoresistance and ability to enter dormancy, studies determining whether this phenomenon would also be seen when immobilizing other cancer cell lines are warranted. Using the same studies as described in Chapter 2, experiments immobilizing other cancer

cell types should be done to see if surviving cells exhibit enhanced chemoresistance or survival upon re-immobilization, despite being in a proliferative state. Cancer cell types where it is also common for a subset of patients to exhibit recurrence after initial treatment (i.e. breast cancer[221], lymphoma[222]) would be of greatest interest. Furthermore, because extracted ovarian cancer cells exhibited enhanced chemoresistance to platinum- and taxane-based chemotherapeutics, other drug types could be screened in this platform. Treating extracted ovarian cancer cells with other types of chemotherapies would inform whether the selected cells from silica gel immobilization have enhanced resistance to specific types of drugs or if they may have innate mechanisms which grant them decreased susceptibility to chemotherapies, regardless of the drug mechanism of action.

5.2.4 Identifying in vitro hyperthermia conditions for an enhanced antitumor immune response using iron oxide-loaded scaffolds under AMF

In Chapter 3, iron oxide-loaded scaffolds were shown to effectively generate heat under AMF and could be used to kill ovarian cancer cells *in vitro*. Further, the overall temperature rise during a 15-minute treatment could be changed by altering simple design parameters, such as the amount of iron oxide loaded into scaffolds and the magnetic field strength. Additional studies generating ovarian cancer cell lysates using different temperatures and heating durations could be completed to identify which hyperthermia conditions lead to generation of an effective antitumor immune response *in vitro*. These studies are of interest because there is limited understanding of which temperatures and treatment durations are best for robust antitumor immunity[145,223]. Previous work has shown that a difference of just a few degrees in cancer cell heating can cause different immune responses[224,225], but it is not understood why or which conditions are best.

In addition to iron oxide loading amount and magnetic field strength, there are opportunities to tune the heating of these scaffolds by also investigating other parameters, such as magnetic field frequency and iron oxide particle size and morphology. As mentioned in Chapter 3, superparamagnetic iron oxide nanoparticles have been extensively characterized in heating studies under AMF and could be incorporated into scaffolds for faster heating rates and to reach higher temperatures. Ovarian cancer cell lysates could be generated from different heating conditions using iron oxide-loaded scaffolds under AMF, and these lysates could be investigated for the ability to elicit an antitumor immune response as measured by antigen-specific T cell proliferation or functionality.

If significant differences in T cell behavior are observed, additional lysate characterization studies could be completed to further elucidate which mechanisms led to differences in T cell response. Characterizing the mode of cell death (apoptosis vs. necrosis) - which is known to cause differences in immune response[226] - and comparing the amounts of immunomodulatory proteins known to be important in antitumor immunity (e.g. HSP70, HSP90)[145] would be of interest. Further, dendritic cell uptake, processing, and presentation of antigen from different ovarian cancer lysates could be evaluated, and this would help determine if hyperthermia conditions influence the development of antitumor immunity via dendritic cells. Overall, potential findings from studies like these would help advance the field, because the intersection of focal therapies - including hyperthermia - and immunology is a relatively new area.

5.2.5 Evaluating in vivo therapeutic potential of iron oxide-loaded scaffolds under AMF in an advanced stage ovarian cancer mouse model

In Chapter 4, it was verified that iron oxide-loaded scaffolds could capture disseminated ID8 cells *in vivo* prior to significant disease formation. This finding prompts studies investigating whether these captured ID8 cells can be successfully killed under AMF and whether hyperthermic treatment of ID8 cells can act as an *in situ* vaccination method to elicit an antitumor immune response and mitigate disease progression. We have already observed ID8 cells captured at the iron oxide-loaded scaffolds as early as 8.5 weeks post-ID8 injection, but it is likely that ID8 cells are present before then and AMF treatment could be administered earlier. Similar to previous studies, histological analysis of iron oxide-loaded scaffolds three days after AMF-treatment would verify whether ID8 cells were successfully killed. After verifying ID8 cells can be killed at iron oxide-loaded scaffolds, it would be interesting to determine if ID8 cells re-infiltrate scaffolds after successful AMF treatment and whether hyperthermic treatment could be administered multiple times to repeatedly decrease the disease burden.

Further studies should investigate how early AMF treatment is needed or if AMF treatment is needed multiple times for disease progression to be slowed, relative to ID8 mice with iron oxide-loaded scaffolds that do not receive AMF treatment and ID8 mice with no scaffolds. Mice weight and abdomen size could easily be monitored throughout the study for comparison, and necropsy evaluation and disease scoring could be used to identify whether AMF treatment decreased the extent of disease of ID8 mice at the study end-point. To investigate whether hyperthermic treatment of ID8 cells elicits an antitumor immune response *in vivo*, phenotyping of immune cells in the peritoneal cavity could be done.

Comparison of pro-tumor and antitumor immune cell populations in ID8 mice with iron oxide-loaded scaffolds before and after AMF treatment would be most interesting to see if hyperthermia results in a less immunosuppressive environment. Overall, the time to disease end-point (30 g weight and visual abdominal swelling) for each experimental group would indicate whether iron oxide-loaded scaffolds under AMF can be effectively used to slow disease progression and enhance survival. Synergistic treatments combining iron oxide-loaded scaffolds with other immunotherapies (i.e. immune checkpoint inhibition) should also be considered also in the future, since our collaborative work has previously shown the promise of coupling focal therapies with immunotherapy to help mitigate secondary disease.

Bibliography

1. Stewart C, Ralyea C, Lockwood S. Ovarian Cancer: An Integrated Review. *Semin Oncol Nurs*. 2019;35(2):151-156.

2. Jayson GC, Kohn EC, Kitchener HC, Ledermann JA. Ovarian Cancer. *Lancet*. 2014;384(9951):1376-1388.

3. Neff RT, Senter L, Salani R. BRCA mutation in ovarian cancer: testing, implications and treatment considerations. *Ther Adv Med Oncol*. 2017;9(8):519-531.

4. Bast R, Hennessy B, Mills G. The biology of ovarian cancer: new opportunities for translation. *Nat Rev Cancer*. 2009;9(6):1-28. doi:10.1038/nrc2644.The

5. Bast R, Mills G. The Molecular Basis of Cancer. In: J M, P H, M I, J G, C T, eds. *The Molecular Basis of Cancer*. 3rd ed. Philadelphia: W.B. Saunders Co.; 2008:441-455.

6. Cancer Genome Atlas Research Network . Integrated genomic analyses of ovarian carcinoma. *Nature*. 2011;474(7353):609-615.

7. Zhang Y, Cao L, Nguyen D, Lu H. TP53 mutations in epithelial ovarian cancer. *Transl Cancer Res*. 2016;5(6):650-663. doi:10.21037/tcr.2016.08.40

8. Rubin SC, Blackwood MA, Bandera C, et al. BRCA1, BRCA2, and hereditary nonpolyposis colorectal cancer gene mutations in an unselected ovarian cancer population: relationship to family history and implications for genetic testing. *Am J Obstet Gynecol*. 1998;178(4):670-677.

9. Lancaster JM, Wooster R, Mangion J, et al. BRCA2 mutations in primary breast and ovarian cancers. *Nat Genet*. 1996;13(2):238-240.

10. Domcke S, Sinha R, Levine DA, Sander C, Schultz N. Evaluating cell lines as tumour models by comparison of genomic profiles. *Nat Commun*. 2013;4(2126):1-10. doi:10.1038/ncomms3126

11. Tavassoli F, Devilee P. Tumors of the ovary and peritoneum. In: *Pathology and Genetics of Tumours of the Breast and Female Genital Organs*. 3rd ed. Lyon, France: IARC Press; 2003:113-203.

12. Seidman JD, Horkayne-Szakaly I, Haiba M, Boice CR, Kurman RJ, Ronnett BM. The histologic type and stage distribution of ovarian carcinomas of surface epithelial origin. *Int J Gynecol Pathol*. 2004;23(1):41-44.

13. Gershenson DM, Sun CC, Lu KH, et al. Clinical behavior of stage II-IV low-grade serous carcinoma of the ovary. *Obstet Gynecol*. 2006;108(2):361-368.

14. Bowtell DDL. The genesis and evolution of high-grade serous ovarian cancer. *Nat Rev Cancer*. 2010;10(11):803-808.

15. Fathalla MF. Incessant ovulation--a factor in ovarian neoplasia? *Lancet*. 1971;2(7716).

16. Piek JMJ, Diest PJ van, Zweemer RP, et al. Dysplastic changes in prophylactically removed Fallopian tubes of women predisposed to developing ovarian cancer. *J Pathol*.

2001;195(4):451-456.

17. Kindelberger DW, Lee Y, Miron A, et al. Intraepithelial Carcinoma of the Fimbria and Pelvic Serous Carcinoma: Evidence for a Causal Relationship. *Am J Surg Pathol*. 2007;31(2):161-169.

18. Koshiyama M, Matsumura N, Konishi I. Recent Concepts of Ovarian Carcinogenesis: Type I and Type II. *Biomed Res Int*. 2014;2014:1-11.

19. Barretina J, Caponigro G, Stransky N, et al. The Cancer Cell Line Encyclopedia enables predictive modelling of anticancer drug sensitivity. *Nature*. 2012;483(7391):603-607.

20. Bénard J, Da Silva J, De Blois MC, et al. Characterization of a Human Ovarian Adenocarcinoma Line, IGROV1, in Tissue Culture and in Nude Mice. *Cancer Res*. 1985;45(10):4970-4979.

21. Hamilton TC, Young RC, Mckoy WM, et al. Characterization of a human ovarian carcinoma cell line (NIH:OVCAR-3) with androgen and estrogen receptors. *Cancer Res*. 1983;43:5379-5389.

22. Lengyel E. Ovarian cancer development and metastasis. *Am J Pathol*. 2010;177(3):1053-1064. doi:10.2353/ajpath.2010.100105

23. Huber MA, Kraut N, Beug H. Molecular requirements for epithelial-mesenchymal transition during tumor progression. *Curr Opin Cell Biol*. 2005;17(5):548-558.

24. Cavallaro U, Christofori G. Cell adhesion and signalling by cadherins and Ig-CAMs in cancer. *Nat Rev Cancer*. 2004;4(2):118-132.

25. Kalluri R, Weinberg RA. The basics of epithelial-mesenchymal transition. *J Clin Invest*. 2009;119(6):1420-1428.

26. Sehouli J, Senyuva F, Fotopoulou C, et al. Intra-abdominal tumor dissemination pattern and surgical outcome in 214 patients with primary ovarian cancer. *J Surg Oncol*. 2009;99(7):424-427.

27. Cannistra SA, Kansas GS, Niloff J, DeFranzo B, Kim Y, Ottensmeier C. Binding of ovarian cancer cells to peritoneal mesothelium in vitro is partly mediated by CD44H. *Cancer Res*. 1993;53(16):3830-3838.

28. Strobel T, Swanson L, Cannistra SA. In vivo inhibition of CD44 limits intra-abdominal spread of a human ovarian cancer xenograft in nude mice: a novel role for CD44 in the process of peritoneal implantation. *Cancer Res*. 1997;57(7):1228-1232.

29. Strobel T, Cannistra SA. Beta1-integrins partly mediate binding of ovarian cancer cells to peritoneal mesothelium in vitro. *Gynecol Oncol*. 1999;73(3):362-367.

30. Slack-Davis JK, Atkins KA, Harrer C, Hershey ED, Conaway M. Vascular Cell Adhesion Molecule-1 Is a Regulator of Ovarian Cancer Peritoneal Metastasis. *Cancer Res*. 2009;69(4):1469-1476.

31. Mesiano S, Ferrara N, Jaffe RB. Role of vascular endothelial growth factor in ovarian cancer: Inhibition of ascites formation by immunoneutralization. *Am J Pathol*. 1998;153(4):1249-1256. doi:10.1016/S0002-9440(10)65669-6

32. Munnell EW. The changing prognosis and treatment in cancer of the ovary. A report of

235 patients with primary ovarian carcinoma 1952-1961. *Am J Obstet Gynecol*. 1968;100(6):790-805.

33. Griffiths CT. Surgical resection of tumor bulk in the primary treatment of ovarian carcinoma. *Natl Cancer Inst Monogr*. 1975;42(101-104).

34. Eisenkop SM, Friedman RL, Wang HJ. Complete cytoreductive surgery is feasible and maximizes survival in patients with advanced epithelial ovarian cancer: a prospective study. *Gynecol Oncol*. 1998;69(2):103-108.

35. Helm CW, States JC. Enhancing the efficacy of cisplatin in ovarian cancer treatment – could arsenic have a role. *J Ovarian Res*. 2009;2(1):2. doi:10.1186/1757-2215-2-2

36. Agarwal R, Kaye SB. Ovarian cancer: strategies for overcoming resistance to chemotherapy. *Nat Rev Cancer*. 2003;3(7):502-516. doi:10.1038/nrc1123

37. Kalir TA, Kohtz DS. Chemoresistance, dormancy and recurrence in platinum drug therapy of ovarian cancers. In: *Tumor Dormancy, Quiescence, and Senescence, Vol. 3*. Vol 3. ; 2014:79-97. doi:10.1007/978-94-017-9325-4

38. McGuire WP, Hoskins WJ, Brady MF, et al. Cyclophosphamide and cisplatin compared with paclitaxel and cisplatin in patients with stage III and stage IV ovarian cancer. *N Engl J Med*. 1996;334(1):1-6.

39. Piccart MJ, Bertelsen K, James K, et al. Randomized intergroup trial of cisplatin-paclitaxel versus cisplatin-cyclophosphamide in women with advanced epithelial ovarian cancer: three-year results. *J Natl Cancer Inst*. 2000;92(9):699-708.

40. Jordan MA, Wilson L. Microtubules as a target for anticancer drugs. *Nat Rev Cancer*. 2004;4:253-265.

41. Mantia-Smaldone GM, Edwards RP, Vlad AM. Targeted treatment of recurrent platinum-resistant ovarian cancer: Current and emerging therapies. *Cancer Manag Res*. 2011;3(1):25-38. doi:10.2147/CMR.S8759

42. Pfisterer J, Ledermann JA. Management of platinum-sensitive recurrent ovarian cancer. *Semin Oncol*. 2006;33(SUPPL. 6):12-16. doi:10.1053/j.seminoncol.2006.03.012

43. Oronsky B, Ray CM, Spira AI, Trepel JB, Carter CA, Cottrill HM. A brief review of the management of platinum-resistant–platinum-refractory ovarian cancer. *Med Oncol*. 2017;34(6):1-7. doi:10.1007/s12032-017-0960-z

44. Markman M, Markman J, Webster K, et al. Duration of response to second-line, platinum-based chemotherapy for ovarian cancer: implications for patient management and clinical trial design. *J Clin Oncol*. 2004;22(15):3120-3125.

45. Ushijima K. Treatment for recurrent ovarian cancer - At first relapse. *J Oncol*. 2009;2010. doi:10.1155/2010/497429

46. Liu J, Matulonis UA. New strategies in ovarian cancer: Translating the molecular complexity of ovarian cancer into treatment advances. *Clin Cancer Res*. 2014;20(20):5150-5156. doi:10.1158/1078-0432.CCR-14-1312

47. Kim A, Ueda Y, Naka T, Enomoto T. Therapeutic strategies in epithelial ovarian cancer. *J Exp Clin Cancer Res*. 2012;31(1):14. doi:10.1186/1756-9966-31-14

48. Markman M, Bookman MA. Second-line treatment of ovarian cancer. *Oncologist*. 2000;5(1):26-35.

49. Weroha S, Becker M, Enderica-Gonzalez, S Harrington S, et al. Tumorgrafts as in vivo surrogates for women with ovarian cancer. *Clin Cancer Res*. 2014;20(5):1288-1297.

50. Topp MD, Hartley L, Cook M, et al. Molecular correlates of platinum response in human high-grade serous ovarian cancer patient-derived xenografts. *Mol Oncol*. 2014;8(3):656-668.

51. Kim HS, Kim TJ, Chung HH, et al. In vitro extreme drug resistance assay to taxanes or platinum compounds for the prediction of clinical outcomes in epithelial ovarian cancer: a prospective cohort study. *J Cancer Res Clin Oncol*. 2009;135(11).

52. Cree IA. Chemosensitivity and chemoresistance testing in ovarian cancer. *Curr Opin Obstet Gynecol*. 2009;21(1):39-43.

53. Schrag D, Garewal HS, Burstein HJ, Samson DJ, Hoff DD Von, Somerfield MR. American Society of Clinical Oncology Technology Assessment: Chemotherapy Sensitivity and Resistance Assays. *J Clin Oncol*. 2004;22(17):3631-3638.

54. Lloyd KL, Cree IA, Savage RS. Prediction of resistance to chemotherapy in ovarian cancer: a systematic review. *BMC Cancer*. 2015;15(117).

55. Grendys Jr. EC, Fiorica J V., Orr Jr. JW, et al. Overview of a chemoresponse assay in ovarian cancer. *Clin Transl Oncol*. 2014;16(9):761-769.

56. Steffensen KD, Waldstrøm M, Jakobsen A. The relationship of platinum resistance and ERCC1 protein expression in epithelial ovarian cancer. *Int J Gynecol Cancer*. 2009;19(5):820-825. doi:10.1111/IGC.0b013e3181a12e09

57. Ling K-S, Chen G-D, Tsai H-J, Lee M-S, Wang P-H, Liua F-S. Mechanisms Involved in Chemoresistance in Ovarian Cancer. *Taiwan J Obstet Gynecol*. 2005;44(3):209-217.

58. Joncourt F, Buser K, Altermatt H, Bacchi M, Oberli A, Cerny T. Multiple drug resistance parameter expression in ovarian cancer. *Gynecol Oncol*. 1998;70(2):176-182.

59. Fraser M, Leung B, Jahani-Asl A, Yan X, Thompson WE, Tsang BK. Chemoresistance in human ovarian cancer: the role of apoptotic regulators. *Reprod Biol Endocrinol*. 2003;1(66).

60. Chien J, Kuang R, Landen C, Shridhar V. Platinum-sensitive recurrence in ovarian cancer: the role of tumor microenvironment. *Front Oncol*. 2013;3(September):1-6. doi:10.3389/fonc.2013.00251

61. Kondoh E, Mori S, Yamaguchi K, et al. Targeting slow-proliferating ovarian cancer cells. *Int J Cancer*. 2010;126(10):2448-2456. doi:10.1002/ijc.24919

62. Scholzen T, Gerdes J. The Ki-67 protein: From the known and the unknown. *J Cell Physiol*. 2000;182(3):311-322. doi:10.1002/(SICI)1097-4652(200003)182:3<311::AID-JCP1>3.0.CO;2-9

63. Páez D, Labonte MJ, Bohanes P, et al. Cancer dormancy: A model of early dissemination and late cancer recurrence. *Clin Cancer Res*. 2012;18(3):645-653. doi:10.1158/1078-0432.CCR-11-2186

64. Aguirre-Ghiso JA. Models, mechanisms and clinical evidence for cancer dormancy. *Nat Rev Cancer*. 2007;7(11):834-846. doi:10.1038/nrc2256

65. Yoneda J, Kuniyasu H, Crispens MA, Price JE, Bucana CD, Fidler IJ. Expression of Angiogenesis-Related Genes and Progression of Human Ovarian Carcinomas in Nude Mice. *J Natl Cancer Inst*. 1998;90(6):447-454.

66. Monk BJ, Minion LE, Coleman RL. Anti-angiogenic agents in ovarian cancer: past, present, and future. *Ann Oncol*. 2016;27(1):33-39.

67. Burger RA, Sill MW, Monk BJ, Greer BE, Sorosky JI. Phase II trial of bevacizumab in persistent or recurrent epithelial ovarian cancer or primary peritoneal cancer: a Gynecologic Oncology Group Study. *J Clin Oncol*. 2007;25(33):5165-5171.

68. Klotz DM, Wimberger P. Overcoming PARP inhibitor resistance in ovarian cancer: what are the most promising strategies? *Arch Gynecol Obstet*. 2020;302(5):1087-1102.

69. Wang W, Liu JR, Zou W. Immunotherapy in ovarian cancer. *Surg Oncol Clin N Am*. 2020;28(3):447-464. doi:10.1016/j.soc.2019.02.002.Immunotherapy

70. Rosenberg SA, Yang JC, Sherry RM, et al. Durable complete responses in heavily pretreated patients with metastatic melanoma using T-cell transfer immunotherapy. *Clin Cancer Res*. 2011;17(13):4550-4557.

71. Kelderman S, Heemskerk B, Fanchi L, et al. Antigen-specific TIL therapy for melanoma: A flexible platform for personalized cancer immunotherapy. *Eur J Immunol*. 2016;46(6):1351-1360.

72. Kandalaft LE, Odunsi K, Coukos G. Immunotherapy in Ovarian Cancer : Are We There Yet ? *J Clin Oncol*. 2019;37(27):2460-2472. doi:10.1200/JCO.19.00508

73. Liu B, Nash J, Runowicz C, Swede H, Stevens R, Li Z. Ovarian cancer immunotherapy: Opportunities, progresses and challenges. *J Hematol Oncol*. 2010;3:1-11. doi:10.1186/1756-8722-3-7

74. Wang W, Liu JR, Zou W. Immunotherapy in Ovarian Cancer. In: *Surgical Oncology Clinics of North America*. ; 2019:447-464.

75. De La Fuente A, Alonso-Alconada L, Costa C, et al. M-Trap: Exosome-Based Capture of Tumor Cells as a New Technology in Peritoneal Metastasis. *J Natl Cancer Inst*. 2015;107(9):1-10. doi:10.1093/jnci/djv184

76. Azarin SM, Yi J, Gower RM, et al. In vivo capture and label-free detection of early metastatic cells. *Nat Commun*. 2015;6. doi:10.1038/ncomms9094

77. Rao SS, Bushnell GG, Azarin SM, et al. Enhanced survival with implantable scaffolds that capture metastatic breast cancer cells in vivo. *Cancer Res*. 2016;76(18):5209-5218. doi:10.1158/0008-5472.CAN-15-2106

78. Chew SA, Danti S. Biomaterial-Based Implantable Devices for Cancer Therapy. *Adv Healthc Mater*. 2017;6(2). doi:10.1002/adhm.201600766

79. Singh A, Brito I, Lammerding J. Beyond Tissue Stiffness and Bioadhesivity: Advanced Biomaterials to Model Tumor Microenvironments and Drug Resistance. *Trends in Cancer*. 2018;4(4):281-291.

80. Fang JY, Tan SJ, Wu YC, Yang Z, Hoang BX, Han B. From competency to dormancy: a 3D model to study cancer cells and drug responsiveness. *J Transl Med*. 2016;14(38):1-13. doi:10.1186/s12967-016-0798-8

81. Liu Y, Lv J, Liang X, et al. Fibrin Stiffness Mediates Dormancy of Tumor-Repopulating Cells via a Cdc42-Driven Tet2 Epigenetic Program. *Cancer Res*. 2018;78(14):3926-3938. doi:10.1158/0008-5472.CAN-17-3719

82. Pavan Grandhi TS, Potta T, Nitiyanandan R, Deshpande I, Rege K. Chemomechanically engineered 3D organotypic platforms of bladder cancer dormancy and reactivation. *Biomaterials*. 2017;142:171-185. doi:10.1016/j.biomaterials.2017.07.008

83. Lee HR, Pelaez F, Silbaugh AM, Leslie F, Racila E, Azarin SM. Biomaterial Platform to Establish a Hypoxic Metastatic Niche in Vivo. *ACS Appl Bio Mater*. 2019;2(4):1549-1560. doi:10.1021/acsabm.8b00837

84. Levy A, Leynes C, Baig M, Chew SA. The Application of Biomaterials in the Treatment of Platinum-Resistant Ovarian Cancer. *ChemMedChem*. 2019;14(21):1810-1827.

85. Pelaez F, Manuchehrabadi N, Roy P, et al. Biomaterial scaffolds for non-invasive focal hyperthermia as a potential tool to ablate metastatic cancer cells. *Biomaterials*. 2018;166:27-37. doi:10.1016/j.biomaterials.2018.02.048

86. Seib FP, Berry JE, Shiozawa Y, Taichman RS, Kaplan DL. Tissue engineering a surrogate niche for metastatic cancer cells. *Biomaterials*. 2015;51:313-319.

87. Bersani F, Lee J, Yu M, et al. Bioengineered Implantable Scaffolds as a Tool to Study Stromal-Derived Factors in Metastatic Cancer Models. *Cancer Res*. 2014;74(24).

88. Thibaudeau L, Taubenberger A V, Holzapfel BM, et al. A tissue-engineered humanized xenograft model of human breast cancer metastasis to bone. *Dis Model Mech*. 2014;7(2):299-309.

89. Holzapfel BM, Wagner F, Loessner D, et al. Species-specific homing mechanisms of human prostate cancer metastasis in tissue engineered bone. *Biomaterials*. 2014;35(13):4108-4115.

90. Aguado BA, Caffe JR, Nanavati D, et al. Extracellular matrix mediators of metastatic cell colonization characterized using scaffold mimics of the pre-metastatic niche. *Acta*. 2016;33(1):13-24.

91. Aguado BA, Hartfield RM, Bushnell GG, et al. Biomaterial Scaffolds as Pre-metastatic Niche Mimics Systemically Alter the Primary Tumor and Tumor Microenvironment. *Adv Healthc Mater*. 2018;7(10).

92. Bushnell GG, Hardas TP, Hartfield RM, et al. Biomaterial Scaffolds Recruit an Aggressive Population of Metastatic Tumor Cells In Vivo. *Cancer Res*. 2019;79(8).

93. Scott CL, Mackay HJ, Haluska Jr. P. Patient-derived xenograft models in gynecologic malignancies. In: *American Society of Clinical Oncology Educational Book*. ; 2014:258-266.

94. Raghavan S, Mehta P, Ward MR, et al. Personalized Medicine Based Approach to Model Patterns of Chemoresistance, and Tumor Recurrence Using Ovarian Cancer Stem Cell Spheroids. *Clin Cancer Res*. 2017;23(22):6934-6945.

95. Rashidi MRW, Mehta P, Bregenzer M, et al. Engineered 3D Model of Cancer Stem Cell Enrichment and Chemoresistance. *Neoplasia*. 2019;21(8):822-836.

96. Carcereri de Prati A, Butturini E, Rigo A, et al. Metastatic breast cancer cells enter into dormant state and express cancer stem cells phenotype under chronic hypoxia. *J Cell Biochem*. 2017;118(10):3237-3248. doi:10.1002/jcb.25972

97. Oya N, Zölzer F, Werner F, Streffer C. Effects of serum starvation on radiosensitivity, proliferation and apoptosis in four human tumor cell lines with different p53 status. *Strahlentherapie und Onkol*. 2003;179(2):99-106. doi:10.1007/s00066-003-0973-8

98. Preciado JA, Reátegui E, Azarin SM, Lou E, Aksan A. Immobilization platform to induce quiescence in dormancy-capable cancer cells. *Technology*. 2017;05(03):129-138. doi:10.1142/S2339547817500078

99. Koti M, Gooding RJ, Nuin P, et al. Identification of the IGF1/PI3K/NF κB/ERK gene signalling networks associated with chemotherapy resistance and treatment response in high-grade serous epithelial ovarian cancer. *BMC Cancer*. 2013;13:1-11. doi:10.1186/1471-2407-13-549

100. Reátegui E, Kasinkas L, Kniesz K, Lefebvre MA, Aksan A. Silica–PEG gel immobilization of mammalian cells. *J Mater Chem B*. 2014;2(42):7440-7448. doi:10.1039/C4TB00812J

101. Gerdes J, Lemke H, Baisch H, Wacker HH, Schwab U, Stein H. Cell cycle analysis of a cell proliferation-associated human nuclear antigen defined by the monoclonal antibody Ki-67. *J Immunol*. 1984;133(4):1710-1715.

102. Sosa MS, Avivar-Valderas A, Bragado P, Wen HC, Aguirre-Ghiso JA. ERK1/2 and p38α/β signaling in tumor cell quiescence: Opportunities to control dormant residual disease. *Clin Cancer Res*. 2011;17(18):5850-5857. doi:10.1158/1078-0432.CCR-10-2574

103. Raingeaud J, Gupta S, Rogers JS, et al. Pro-inflammatory Cytokines and Environmental Stress Cause p38 Mitogen-activated Protein Kinase Activation by Dual Phosphorylation on Tyrosine and Threonine. *J Biol Chem*. 1995;270:7420-7426.

104. Brancho D, Tanaka N, Jaeschke A, et al. Mechanism of p38 MAP kinase activation in vivo. *Genes Dev*. 2003;17:1969-1978. doi:10.1101/gad.1107303.on

105. V.Bulavin D, Fornace Jr. AJ. p38 MAP Kinase's Emerging Role as a Tumor Suppressor. In: *Advances in Cancer Research*. ; 2004:95-118.

106. Aguirre-ghiso JA, Ossowski L, Rosenbaum SK. Green Fluorescent Protein Tagging of Extracellular Signal-Regulated Kinase and p38 Pathways Reveals Novel Dynamics of Pathway Activation during Primary and Metastatic Growth. *Cancer Res*. 2004;418:7336-7345.

107. Aguirre-ghiso JA, Liu D, Mignatti A, Kovalski K, Ossowski L. Urokinase Receptor and Fibronectin Regulate the ERK MAPK to p38 MAPK Activity Ratios That Determine Carcinoma Cell Proliferation or Dormancy In Vivo. *Mol Biol Cell*. 2001;12:863-879.

108. Aguirre-ghiso JA, Estrada Y, Liu D, Ossowski L. ERK MAPK Activity as a Determinant of Tumor Growth and Dormancy ; Regulation by p38 SAPK. *Cancer Res*. 2003;63(7):1684-1695.

109. Gao Z, Zhu M, Wu Y, Gao P, Qin Z, Wang H. Interferon-λ1 induces G1 phase cell cycle arrest and apoptosis in gastric carcinoma cells in vitro. *Oncol Rep*. 2014;32(1):199-204.

110. Tate DJ, Patterson JR, Finkel-Jimenez B, Zea AH. Interferon (IFNγ) induces cell cycle arrest in RCC cell lines. *J Immunother Cancer*. 2013;1(1):125.

111. Wall L, Burke F, Barton C, Smyth J, Balkwill F. IFN-γ Induces Apoptosis in Ovarian Cancer Cells in Vivo and in Vitro. *Clin Cancer Res*. 2003;9(3).

112. Wang N. Review of Cellular Mechanotransduction. *J Phys D Appl Phys*. 2017;50(23).

113. Katsumi A, Orr AW, Tzima E, Schwartz MA. Integrins in Mechanotransduction. *J Biol Chem*. 2004;279:12001-12004.

114. Touil Y, Zuliani T, Wolowczuk I, et al. The PI3K/AKT signaling pathway controls the quiescence of the low-Rhodamine123-retention cell compartment enriched for melanoma stem cell activity. *Stem Cells*. 2013;31(4):641-651.

115. Correa RJM, Peart T, Valdes YR, Dimattia GE, Shepherd TG. Modulation of AKT activity is associated with reversible dormancy in ascites-derived epithelial ovarian cancer spheroids. *Carcinogenesis*. 2012;33(1):49-58. doi:10.1093/carcin/bgr241

116. Sosa MS, Bragado P, Aguirre-Ghiso JA. Mechanisms of disseminated cancer cell dormancy: an awakening field. *Nat Rev Cancer*. 2014;14(9):611-622.

117. Daubriac J, Fleury-Feith J, Kheuang L, et al. Malignant pleural mesothelioma cells resist anoikis as quiescent pluricellular aggregates. *Cell Death Differ*. 2009;16:1146-1155.

118. Pang J, Jiang P, Wang Y, et al. Cross-linked hyaluronan gel inhibits the growth and metastasis of ovarian carcinoma. *J Ovarian Res*. 2018;11(22).

119. Yeh AC, Ramaswamy S. Mechanisms of Cancer Cell Dormancy—Another Hallmark of Cancer? *Cancer Res*. 2015;75(23).

120. Patel D, Gao Y, Son K, et al. Microfluidic co-cultures with hydrogel-based ligand trap to study paracrine signals giving rise to cancer drug resistance. *Lab Chip*. 2015;(24):4614-4624.

121. Ware KE, Hinz TK, Kleczko E, et al. A mechanism of resistance to gefitinib mediated by cellular reprogramming and the acquisition of an FGF2-FGFR1 autocrine growth loop. *Oncogenesis*. 2013;2(3).

122. Fenig E, Wieder R, Paglin S, et al. Basic fibroblast growth factor confers growth inhibition and mitogen-activated protein kinase activation in human breast cancer cells. *Clin Cancer Res*. 1997;3(1).

123. Wang H, Rubin M, Fenig E, et al. Basic Fibroblast Growth Factor Causes Growth Arrest in MCF-7 Human Breast Cancer Cells while Inducing both Mitogenic and Inhibitory G1 Events. *Cancer Res*. 1997;57(9).

124. Roussos ET, Condeelis JS, Patsialou A. Chemotaxis in cancer. *Nat Rev Cancer*. 2014;11(8):573-587.

125. Son H, Moon A. Epithelial-mesenchymal Transition and Cell Invasion. *Toxicol Res*. 2010;26(4).

126. Zhang C, Ji Q, Yang Y, Li Q, Wang Z. Exosome: Function and Role in Cancer Metastasis and Drug Resistance. *Technol Cancer Res Treat*. 2018;17.

127. Samuel P, Mulcahy LA, Furlong F, et al. Cisplatin induces the release of extracellular vesicles from ovarian cancer cells that can induce invasiveness and drug resistance in bystander cells. *Philos Trans R Soc Lond B Biol Sci*. 2018;373.

128. Foley JM, II DJS, Monks NR, et al. Anoikis-resistant subpopulations of human osteosarcoma display significant chemoresistance and are sensitive to targeted epigenetic therapies predicted by expression profiling. *J Transl Med*. 2015;13.

129. Eguchi R, Fujita Y, Tabata C, et al. Inhibition of Src family kinases overcomes anoikis resistance induced by spheroid formation and facilitates cisplatin-induced apoptosis in human mesothelioma cells. *Oncol Rep*. 2015;34(5):2305-2310.

130. Wheeler LJ, Watson ZL, Qamar L, et al. CBX2 identified as driver of anoikis escape and dissemination in high grade serous ovarian cancer. *Oncogenesis*. 2018.

131. Liao J, Qian F, Tchabo N, et al. Ovarian Cancer Spheroid Cells with Stem Cell-Like Properties Contribute to Tumor Generation, Metastasis and Chemotherapy Resistance through Hypoxia-Resistant Metabolism. *PLoS One*. 2014;9(1).

132. Hirst J, Pathak HB, Hyter S, et al. Licofelone Enhances the Efficacy of Paclitaxel in Ovarian Cancer by Reversing Drug Resistance and Tumor Stem-like Properties. *Cancer Res*. 2018;78(15).

133. Annunziata CM, Stavnes HT, Kleinberg L, et al. NF-κB transcription factors are co-expressed and convey poor outcome in ovarian cancer. *Cancer*. 2010;116(13).

134. Godwin P, Baird AM, Heavey S, Barr MP, O'Byrne KJ, Gately K. Targeting Nuclear Factor-Kappa B to Overcome Resistance to Chemotherapy. *Front Oncol*. 2013;3(120).

135. Barlin JN, Jelinic P, Olvera N, et al. Validated gene targets associated with curatively treated advanced serous ovarian carcinoma. *Gynecol Oncol*. 2013;128(3):512-517.

136. Yoshikawa T, Miyamoto M, Aoyama T, et al. JAK2/STAT3 pathway as a therapeutic target in ovarian cancers. *Oncol Lett*. 2018;15(4):5772-5780.

137. Permuth-Wey J, Fulp WJ, Reid BM, et al. STAT3 polymorphisms may predict an unfavorable response to first-line platinum-based therapy for women with advanced serous epithelial ovarian cancer. *Int J Cancer*. 2016;138(3):612-619.

138. Abubaker K, Latifi A, Chan E, et al. Enhanced activation of STAT3 in ascites-derived recurrent ovarian tumors: inhibition of cisplatin-induced STAT3 activation reduced tumorigenicity of ovarian cancer by a loss of cancer stem cell-like characteristics. *J Cancer Stem Cell Res*. 2015;3:1-17.

139. Lee HR, Leslie F, Azarin SM. A facile in vitro platform to study cancer cell dormancy under hypoxic microenvironments using CoCl2. *J Biol Eng*. 2018;12(12):1-15.

140. Wosikowski K, Silverman JA, Bishop P, Mendelsohn J, Bates SE. Reduced growth rate accompanied by aberrant epidermal growth factor signaling in drug resistant human breast cancer cells. *Biochim Biophys Acta - Mol Cell Res*. 2000;1497(2):215-226. doi:10.1016/S0167-4889(00)00062-8

141. Onozuka H, Tsuchihara K, Esumi H. Hypoglycemic/hypoxic condition in vitro mimicking the tumor microenvironment markedly reduced the efficacy of anticancer drugs. *Cancer Sci*. 2011;102(5):975-982.

142. Kim M, Pak JH, Choi WH, Park J-Y, Nam J-H, Kim J-H. The relationship between cisplatin resistance and histone deacetylase isoform overexpression in epithelial ovarian cancer cell lines. *J Gynecol Oncol*. 2012;23(3):182-189. doi:10.3802/jgo.2012.23.3.182

143. Cristea M, Han E, Salmon L, Morgan RJ. Review: Practical considerations in ovarian cancer chemotherapy. *Ther Adv Med Oncol*. 2010;2(3):175-187. doi:10.1177/1758834010361333

144. Diederich C. Thermal ablation and high-temperature thermal therapy: overview of technology and clinical implementation. *Int J Hyperth*. 2005;21:745-753. doi:10.1080/02656730500271692.

145. Toraya-Brown S, Fiering S. Local tumour hyperthermia as immunotherapy for metastatic cancer. *Int J Hyperth*. 2014;30(8):531-539. doi:10.3109/02656736.2014.968640.

146. Bai J, Liu P, Xu L. Recent advances in thermal treatment techniques and thermally induced immune responses against cancer. *IEEE Trans Biomed Eng*. 2014;61:1497-1505. doi:10.1109/TBME.2014.2314357.

147. Scheffer H, Nielsen K, de Jong M, et al. Irreversible electroporation for nonthermal tumor ablation in the clinical setting: a systematic review of safety and efficacy. *J Vasc Interv Radiol*. 2014;25(7):997-1011. doi:10.1016/j.jvir.2014.01.028.

148. Dewey WC. Arrhenius relationships from the molecule and cell to the clinic. *Int J Hyperth*. 1993;25(1):3-20. doi:10.1080/02656730902747919.

149. Zhang J, Li J, Kawazoe N, Chen G. Composite scaffolds of gelatin and gold nanoparticles with tunable size and shape for photothermal cancer therapy. *J Mater Chem B*. 2017;5:245-253. doi:10.1039/C6TB02872A

150. Luo Y, Wei X, Wan Y, Lin X, Wang Z, Huang P. 3D printing of hydrogel scaffolds for future application in photothermal therapy of breast cancer and tissue repair. *Acta Biomater*. 2019;92:37-47. doi:10.1016/j.actbio.2019.05.039

151. Liu Y, Li T, Ma H, et al. 3D-printed scaffolds with bioactive elements-induced photothermal effect for bone tumor therapy. *Acta Biomater*. 2018;73:531-546. doi:10.1016/j.actbio.2018.04.014

152. Day ES, Morton JG, West JL. Nanoparticles for thermal cancer therapy. *J Biomech Eng*. 2009;131(7):1-5. doi:10.1115/1.3156800

153. Akbarzadeh A, Samiei M, Davaran S. Magnetic nanoparticles: preparation, physical properties, and applications in biomedicine. *Nanoscale Res Lett*. 2012;7(1):144. doi:10.1186/1556-276X-7-144

154. Ashikbayeva Z, Tosi D, Balmassov D, Schena E, Saccomandi P, Inglezakis V. Application of nanoparticles and nanomaterials in thermal ablation therapy of cancer. *Nanomaterials*. 2019;9(9). doi:10.3390/nano9091195

155. Gilchrist RK, Medal R, Shorey WD, Hanselman RC, Parrott JC, Taylor CB. Selective Inductive Heating of Lymph Nodes. *Ann Surg*. 1957;146(4):596-606.

doi:10.1097/00000658-195710000-00007.

156. Jordan A, Scholz R, Maier-Hauff K, et al. The effect of thermotherapy using magnetic nanoparticles on rat malignant glioma. *J Neurooncol*. 2006;78(1):7-14. doi:10.1007/s11060-005-9059-z

157. Hilger I, Hiergeist R, Hergt R, Winnefeld K, Schubert H, Kaiser WA. Thermal Ablation of Tumors Using Magnetic Nanoparticles An In Vivo Feasibility Study. *Invest Radiol*. 2002;37(10):580-586. doi:10.1097/00004424-200210000-00008.

158. Kettering M, Winter J, Zeisberger M, et al. Magnetic nanoparticles as bimodal tools in magnetically induced labelling and magnetic heating of tumour cells: an in vitro study. *Nanotechnology*. 2007;18(17). doi:10.1088/0957-4484/18/17/175101

159. Hilger I, Andrä W, Hergt R, Hiergeist R, Schubert H, Kaiser WA. Electromagnetic Heating of Breast Tumors in Interventional Radiology: In Vitro and in Vivo Studies in Human Cadavers and Mice. *Radiology*. 2001;218(2). doi:10.1148/radiology.218.2.r01fe19570

160. Johannsen M, Jordan A, Scholz R, et al. Evaluation of Magnetic Fluid Hyperthermia in a Standard Rat Model of Prostate Cancer. *J Endourol*. 2004;18(5). doi:10.1089/0892779041271715.

161. Johannsen M, Thiesen B, Jordan A, et al. Magnetic fluid hyperthermia (MFH) reduces prostate cancer growth in the orthotopic Dunning R3327 rat model. *Prostate*. 2005;64:283-292. doi:10.1002/pros.20213.

162. Zhang J, Zhao S, Zhu M, et al. 3D-printed magnetic Fe3O4/MBG/PCL composite scaffolds with multifunctionality of bone regeneration, local anticancer drug delivery and hyperthermia. *J Mater Chem B*. 2014;2(43):7583-7595. doi:10.1039/c4tb01063a

163. Johannsen M, Gneveckow U, Eckelt L, et al. Clinical hyperthermia of prostate cancer using magnetic nanoparticles: Presentation of a new interstitial technique. *Int J Hyperth*. 2005;21(7):637-647. doi:10.1080/02656730500158360.

164. Johannsen M, Gneveckow U, Thiesen B, et al. Thermotherapy of Prostate Cancer Using Magnetic Nanoparticles: Feasibility, Imaging, and Three-Dimensional Temperature Distribution. *Eur Urol*. 2007;52(6):1653-1662. doi:10.1016/j.eururo.2006.11.023.

165. Maier-Hauff K, Rothe R, Scholz R, et al. Intracranial Thermotherapy using Magnetic Nanoparticles Combined with External Beam Radiotherapy: Results of a Feasibility Study on Patients with Glioblastoma Multiforme. *J Neurooncol*. 2007;81(1):53-60. doi:10.1007/s11060-006-9195-0

166. Zhu L, Zhou Z, Mao H, Yang L. Magnetic nanoparticles for precision oncology: Theranostic magnetic iron oxide nanoparticles for image-guided and targeted cancer therapy. *Nanomedicine*. 2017;12(1):73-87. doi:10.2217/nnm-2016-0316

167. Roby KF, Taylor CC, Sweetwood JP, et al. Development of a syngeneic mouse model for events related to ovarian cancer. *Carcinogenesis*. 2000;21(4):585-591. doi:10.1093/carcin/21.4.585

168. Pelaez F, Shao Q, Ranjbartehrani P, et al. Optimizing Integrated Electrode Design for Irreversible Electroporation of Implanted Polymer Scaffolds. *Ann Biomed Eng*. 2020;7. doi:10.1007/s10439-019-02445-4

169. Etheridge ML, Bischof JC. Optimizing magnetic nanoparticle based thermal therapies within the physical limits of heating. *Ann Biomed Eng*. 2013;41(1):78-88. doi:10.1007/s10439-012-0633-1

170. Xie W, Guo Z, Gao F, et al. Shape-, size-and structure-controlled synthesis and biocompatibility of iron oxide nanoparticles for magnetic theranostics. *Theranostics*. 2018;8(12):3284-3307. doi:10.7150/thno.25220

171. Shah RR, Davis TP, Glover AL, Nikles DE, Brazel CS. Impact of magnetic field parameters and iron oxide nanoparticle properties on heat generation for use in magnetic hyperthermia. *J Magn Magn Mater*. 2015;387:96-106. doi:10.1016/j.jmmm.2015.03.085

172. Guardia P, Corato R Di, Lartigue L, et al. Water-Soluble Iron Oxide Nanocubes with High Values of Specific Absorption Rate for Cancer Cell Hyperthermia Treatment. *ACS Nano*. 2012;6(4):3080-3091. doi:10.1021/nn2048137

173. Tong S, Quinto CA, Zhang L, Mohindra P, Bao G. Size-Dependent Heating of Magnetic Iron Oxide Nanoparticles. *ACS Nano*. 2017;11(7):6808-6816. doi:10.1021/acsnano.7b01762

174. Gonzales-Weimuller M, Zeisberger M, Krishnan KM. Size-dependant heating rates of iron oxide nanoparticles for magnetic fluid hyperthermia. *J Magn Magn Mater*. 2009;321(13):1947-1950. doi:10.1016/j.jmmm.2008.12.017

175. Hergt R, Dutz S, Müller R, Zeisberger M. Magnetic particle hyperthermia: Nanoparticle magnetism and materials development for cancer therapy. *J Phys Condens Matter*. 2006;18(38). doi:10.1088/0953-8984/18/38/S26

176. Urano M, Kuroda M, Nishimura Y. For the clinical application of thermochemotherapy given at mild temperatures. *Int J Hyperth*. 1999;15(2):79-107. doi:10.1080/026567399285765.

177. Hildebrandt B, Wust P, Ahlers O, et al. The cellular and molecular basis of hyperthermia. *Crit Rev Oncol Hematol*. 2002;43(1):33-56. doi:10.1016/s1040-8428(01)00179-2

178. Sapareto SA, Hopwood LE, Dewey WC, Raju MR, Gray JW. Effects of Hyperthermia on Survival and Progression of Chinese Hamster Ovary Cells. *Cancer Res*. 1978;38(2).

179. Zhang J, Li J, Wang X, Kawazoe N, Chen G. Targeting ligand-functionalized photothermal scaffolds for cancer cell capture and: In situ ablation. *Biomater Sci*. 2017;5(11):2276-2284. doi:10.1039/c7bm00639j

180. Ferrari M, Cirisano F, Morán MC. Mammalian Cell Behavior on Hydrophobic Substrates: Influence of Surface Properties. *Colloids and Interfaces*. 2019;3(2):48. doi:10.3390/colloids3020048

181. Ankamwar B, Lai TC, Huang JH, et al. Biocompatibility of Fe3O4 nanoparticles evaluated by in vitro cytotoxicity assays using normal, glia and breast cancer cells. *Nanotechnology*. 2010;21(7). doi:10.1088/0957-4484/21/7/075102

182. Liu Y, Chen Z, Wang J. Systematic evaluation of biocompatibility of magnetic Fe3O4 nanoparticles with six different mammalian cell lines. *J Nanoparticle Res*. 2011;13(1):199-212. doi:10.1007/s11051-010-0019-y

183. Lam CXF, Hutmacher DW, Schantz J, Woodruff MA, Teoh SH. Evaluation of

polycaprolactone scaffold degradation for 6 months in vitro and in vivo. *J Biomed Mater Res*. 2009;90(3):906-919. doi:10.1002/jbm.a.32052.

184. Sun H, Mei L, Song C, Cui X, Wang P. The in vivo degradation, absorption and excretion of PCL-based implant. *Biomaterials*. 2006;27(9):1735-1740. doi:10.1016/j.biomaterials.2005.09.019

185. Brezovich IA. Low frequency hyperthermia: Capacitive and ferromagnetic thermoseed methods. *Med Phys Monogr*. 1988;16:82-111.

186. Hergt R, Dutz S. Magnetic particle hyperthermia—biophysical limitations of a visionary tumour therapy. *J Magn Magn Mater*. 2007;311(1):187-192. doi:10.1016/j.jmmm.2006.10.1156

187. Zee J Van Der. Review Heating the patient: a promising approach? *Ann Oncol*. 2002;13:1173-1184. doi:10.1093/annonc/mdf280

188. Ito R, Takahashi T, Katano I, Ito M. Current advances in humanized mouse models. *Cell Mol Immunol*. 2012;9(3):208-214.

189. Paine-Murrieta GD, Taylor CW, Curtis RA, et al. Human tumor models in the severe combined immune deficient (scid) mouse. *Cancer Chemother Pharmacol*. 1997;40(3):209-214.

190. Magnottia E, Marascoa WA. The latest animal models of ovarian cancer for novel drug discovery. *Expert Opin Drug Discov*. 2018;13(3):249-257.

191. Watanabe Y, Takahashi T, Okajima A, et al. The analysis of the functions of human B and T cells in humanized NOD/shi-scid/gammac(null) (NOG) mice (hu-HSC NOG mice). *Int Immunol*. 2009;21(7):843-858.

192. Toss A, Tomasello C, Razzaboni E, et al. Hereditary ovarian cancer: Not only BRCA 1 and 2 Genes. *Biomed Res Int*. 2015;2015. doi:10.1155/2015/341723

193. Ayantunde AA, Parsons SL. Pattern and prognostic factors in patients with malignant ascites: a retrospective study. *Ann Oncol*. 2007;18(5):945-949.

194. Sheid B. Angiogenic effects of macrophages isolated from ascitic fluid aspirated from women with advanced ovarian cancer. *Cancer Lett*. 1992;62(2):153-158.

195. Kipps E, Tan DSP, Kaye SB. Meeting the challenge of ascites in ovarian cancer: new avenues for therapy and research. *Nat Rev Cancer*. 2013;13(4):273-282. doi:10.1038/nrc3432.Meeting

196. Holm-Nielsen P. Pathogenesis of ascites in peritoneal carcinomatosis. *J Pathol Microbiol Immunol*. 1953;33(1):10-21.

197. Nagy JA, Herzberg KT, Dvorak JM, Dvorak HF. Pathogenesis of malignant ascites formation: initiating events that lead to fluid accumulation. *Cancer Res*. 1993;53(11):2631-2643.

198. Naora H, Montell DJ. Ovarian cancer metastasis: integrating insights from disparate model organisms. *Nat Rev Cancer*. 2005;5(5):355-366.

199. Yeung T-L, Leung CS, Yip K-P, Yeung CLA, Wong STC, Mok SC. Cellular and molecular processes in ovarian cancer metastasis. A Review in the Theme: Cell and

Molecular Processes in Cancer Metastasis. *Am J Physiol Cell Physiol*. 2015;309(7):444-456.

200. Carmignani CP, Sugarbaker TA, Bromley CM, Sugarbaker PH. Intraperitoneal cancer dissemination: mechanisms of the patterns of spread. *Cancer Metastasis Rev*. 2003;22(4):465-472.

201. Tan DSP, Agarwal R, Kaye SB. Mechanisms of transcoelomic metastasis in ovarian cancer. *Lancet Oncol*. 2006;7(11):925-934.

202. Arauchi A, Yang CH, Cho S, et al. An immunocompetent, orthotopic mouse model of epithelial ovarian cancer utilizing tissue engineered tumor cell sheets. *Tissue Eng - Part C Methods*. 2015;21(1):23-34. doi:10.1089/ten.tec.2014.0040

203. Greenaway J, Moorehead R, Shaw P, Petrik J. Epithelial-stromal interaction increases cell proliferation, survival and tumorigenicity in a mouse model of human epithelial ovarian cancer. *Gynecol Oncol*. 2008;108(2):385-394. doi:10.1016/j.ygyno.2007.10.035

204. Decio A, Giavazzi R. Orthotopic Model of Ovarian Cancer. In: *Tumor Angiogenesis Assays*. New York, NY: Humana Press; 2016:139-149.

205. Nieman KM, Kenny HA, Penicka C V, et al. Adipocytes promote ovarian cancer metastasis and provide energy for rapid tumor growth. *Nat Med*. 2011;17:1498-1503.

206. Lam T, Moy A, Lee HR, Shao Q, Bischof JC, Azarin SM. Iron oxide-loaded polymer scaffolds for non-invasive hyperthermic treatment of infiltrated cells. *AIChE J*. 2020;66(12). doi:10.1002/aic.17001

207. Majety M, Pradel LP, Gies M, Ries CH. Fibroblasts influence survival and therapeutic response in a 3D co-culture model. *PLoS One*. 2015;10(6):1-18. doi:10.1371/journal.pone.0127948

208. Koller F, Palsson BØ, Masters J. *Primary Mesenchymal Cells*.; 2001.

209. O'Donnell RL, McCormick A, Mukhopadhyay A, et al. The use of ovarian cancer cells from patients undergoing surgery to generate primary cultures capable of undergoing functional analysis. *PLoS One*. 2014;9(6):e90604. doi:10.1371/journal.pone.0090604

210. Zhu J, Thakolwiboon S, Liu X, Zhang M, Lubman DM. Overexpression of cd90 (thy-1) in pancreatic adenocarcinoma present in the tumor microenvironment. *PLoS One*. 2014;9(12):1-20. doi:10.1371/journal.pone.0115507

211. Kisselbach L, Merges M, Bossie A, Boyd A. CD90 expression on human primary cells and elimination of contaminating fibroblasts from cell cultures. *Cytotechnology*. 2009;59(1):31-44. doi:10.1007/s10616-009-9190-3

212. Chu P, Wu E, Weiss LM. Cytokeratin 7 and cytokeratin 20 expression in epithelial neoplasms: a survey of 435 cases. *Mod Pathol*. 2000;13(9):962-972. doi:10.1038/modpathol.3880175

213. Gupta D, Lis CG. Role of CA125 in predicting ovarian cancer survival - A review of the epidemiological literature. *J Ovarian Res*. 2009;2(1):1-20. doi:10.1186/1757-2215-2-13

214. Markman M. The Role of CA-125 in the Management of Ovarian Cancer. *Oncologist*. 1997;2(1):6-9.

215. Strauss R, Li ZY, Liu Y, et al. Analysis of epithelial and mesenchymal markers in ovarian cancer reveals phenotypic heterogeneity and plasticity. *PLoS One*. 2011;6(1):1-20. doi:10.1371/journal.pone.0016186

216. Pribyl LJ, Coughlin KA, Sueblinvong T, et al. Method for Obtaining Primary Ovarian Cancer Cells From Solid Specimens. *J Vis Exp*. 2014;84.

217. Shyu RY, Su HL, Yu JC, Jiang SY. Direct growth suppressive activity of interferon-alpha and -gamma on human gastric cancer cells. *J Surg Oncol*. 2000;75(2):122-130.

218. Shang D, Yang P, Liu Y, Song J, Zhang F, Tian Y. Interferon-α Induces G1 Cell-Cycle Arrest in Renal Cell Carcinoma Cells Via Activation of Jak-Stat Signaling. *Cancer Invest*. 2011;29(5):347-352.

219. Burke F, Smith PD, Crompton MR, Upton C, Balkwill FR. Cytotoxic response of ovarian cancer cell lines to IFN-γ is associated with sustained induction of IRF-1 and p21 mRNA. *Br J Cancer*. 1999;80(8):1236-1244. doi:10.1038/sj.bjc.6690491

220. Katayama T, Nakanishi K, Nishihara H, et al. Type I interferon prolongs cell cycle progression via p21 WAF1/CIP1 induction in human colon cancer cells. *Int J Oncol*. 2007;31(3):613-620. doi:10.3892/ijo.31.3.613

221. Pan H, Gray R, Braybrooke J, et al. 20-Year Risks of Breast-Cancer Recurrence after Stopping Endocrine Therapy at 5 Years. *N Engl J Med*. 2017;377:1836-1846.

222. Glimelius I, Diepstra A. Novel treatment concepts in Hodgkin lymphoma. *J Intern Med*. 2016;281(3):247-260.

223. Repasky EA, Evans SS, Dewhirst MW. Temperature Matters! And Why it Should Matter to Tumor Immunologists. *Cancer Immunol Res*. 2013;1(4):210-216. doi:10.1158/2326-6066.CIR-13-0118.Temperature

224. Toraya-Brown S, Sheen MR, Zhang P, et al. Local hyperthermia treatment of tumors induces CD8+ T cell-mediated resistance against distal and secondary tumors. *Nanomedicine*. 2015;10(6):1273-1285.

225. Takada T, Yamashita T, Sato M, et al. Growth Inhibition of Re-Challenge B16 Melanoma Transplant by Conjugates of Melanogenesis Substrate and Magnetite Nanoparticles as the Basis for Developing Melanoma-Targeted Chemo-Thermo-Immunotherapy. *J Biomed Biotechnol*. 2009.

226. Chu KF, Dupuy DE. Thermal ablation of tumours: Biological mechanisms and advances in therapy. *Nat Rev Cancer*. 2014;14(3):199-208. doi:10.1038/nrc3672